④

Applied Research Laboratory
The Pennsylvania State University

MEASUREMENT AND ANALYSIS OF THE NOISE RADIATED BY LOW MACH NUMBERS CENTRIFUGAL BLOWERS

by

D. M. Yeager and G. C. Lauchle

ARL-PSU

TECHNICAL REPORT

(4)

The Pennsylvania State University
APPLIED RESEARCH LABORATORY
P.O. Box 30
State College, PA 16804

MEASUREMENT AND ANALYSIS OF THE NOISE RADIATED BY LOW MACH NUMBERS CENTRIFUGAL BLOWERS

by

D. M. Yeager and G. C. Lauchle

N00024-85-C-6041

Technical Report No. TR 87-009
November 1987

Supported by:
IBM

L. R. Hettche
Applied Research Laboratory

Unclassified

SECURITY CLASSIFICATION OF THIS PAGE

A189226

REPORT DOCUMENTATION PAGE

1a. REPORT SECURITY CLASSIFICATION
Unclassified

1b. RESTRICTIVE MARKINGS

2a. SECURITY CLASSIFICATION AUTHORITY

2b. DECLASSIFICATION / DOWNGRADING SCHEDULE

3. DISTRIBUTION / AVAILABILITY OF REPORT
(A) Unlimited

4. PERFORMING ORGANIZATION REPORT NUMBER(S)

5. MONITORING ORGANIZATION REPORT NUMBER(S)

6a. NAME OF PERFORMING ORGANIZATION
IBM

6b. OFFICE SYMBOL *(If applicable)*

7a. NAME OF MONITORING ORGANIZATION

6c. ADDRESS *(City, State, and ZIP Code)*
P.O. Box 390
Poughkeepsie, NY 12602

7b. ADDRESS *(City, State, and ZIP Code)*

8a. NAME OF FUNDING / SPONSORING ORGANIZATION
IBM

8b. OFFICE SYMBOL *(If applicable)*
IBM

9. PROCUREMENT INSTRUMENT IDENTIFICATION NUMBER

8c. ADDRESS *(City, State, and ZIP Code)*
P.O. Box 390
Poughkeepsie, NY 12602

10. SOURCE OF FUNDING NUMBERS

PROGRAM ELEMENT NO.	PROJECT NO.	TASK NO.	WORK UNIT ACCESSION NO

11. TITLE *(Include Security Classification)*
Measurement and Analysis of the Noise Radiated by Low Mach Number Centrifugal Blowers (unclassified)

12. PERSONAL AUTHOR(S)
D. M. Yeager and G. C. Lauchle

13a. TYPE OF REPORT
Ph.D. Thesis

13b. TIME COVERED
FROM ________ TO ________

14. DATE OF REPORT *(Year, Month Day)*
October 1987

15. PAGE COUNT
219

16. SUPPLEMENTARY NOTATION

17. COSATI CODES

FIELD	GROUP	SUB-GROUP

18. SUBJECT TERMS *(Continue on reverse if necessary and identify by block number)*
aerodynamic noise, centrifugal blowers, acoustic intensity, frequency domain analysis, flow visualization, cascade analysis, computational fluid dynamics

19. ABSTRACT *(Continue on reverse if necessary and identify by block number)*

An investigation was performed of the broad band aerodynamically generated noise in low tip-speed Mach number, centrifugal air moving devices. An interdisciplinary experimental approach was taken which involved investigation of the aerodynamic and acoustic fields, and their mutual relationship. The noise generation process was studied using two experimental vehicles: 1) a scale model of a homologous family of centrifugal blowers typical of those used to cool computer and business equipment, and 2) a single blade from a centrifugal blower impeller which was placed in a known, controllable flow field.

The radiation characteristics of the model blower were investigated by measuring the acoustic intensity distribution near the blower inlet and

20. DISTRIBUTION / AVAILABILITY OF ABSTRACT
☒ UNCLASSIFIED/UNLIMITED ☐ SAME AS RPT ☐ DTIC USERS

21. ABSTRACT SECURITY CLASSIFICATION
Unclassified

22a. NAME OF RESPONSIBLE INDIVIDUAL

22b. TELEPHONE *(Include Area Code)*

22c. OFFICE SYMBOL

DD FORM 1473, 84 MAR

83 APR edition may be used until exhausted
All other editions are obsolete

SECURITY CLASSIFICATION OF THIS PAGE
Unclassified

comparing it with the intensity near the inlet to an axial flow fan. Results showed that the centrifugal blower is a distributed, random noise source, unlike an axial fan which exhibited the effects of a coherent, interacting source distribution.

Aerodynamic studies of the flow field in the inlet and at the discharge to the rotating impeller were used to assess the mean flow distribution through the impeller blade channels and to identify regions of excessive turbulence near the rotating blade row. These studies included flow field qualification via flow visualization of the inlet field, and quantification of the flow velocities using single- and dual-channel hot film anemometry. Both circumferential and spanwise mean flow nonuniformities were identified along with a region of increased turbulence just downstream of the scroll cutoff. The fluid incidence angle, normally taken as an indicator of blower performance, was estimated from mean flow data as deviating considerably from an ideal impeller design.

New frequency-domain expressions for the correlation area and dipole source strength per unit area on a surface immersed in turbulence were developed which can be used to characterize the noise generation process over a rigid surface immersed in turbulence. The equations show that the correlation area may be thought of as a complex radiation efficiency which is normalized by its maximum value, the total area of the blade surface. Both the correlation area and the dipole source strength per unit area reflect the characteristics of the local turbulence regions and mutual interactions between regions.

An investigation of the noise radiated from the single, isolated airfoil (impeller blade) was performed using modern correlation and spectral analysis techniques. Radiation from the single blade in flow was characterized using these expressions for the correlation area and the dipole source strength per unit area, and from the relationship between the blade surface pressure and the incident turbulent flow field. Also, a computational fluid dynamics computer program was used to model the steady, two-dimensional flow over the single blade profile.

Results showed that radiation from the single blade was dominated by the effects of the incident turbulence. Normalized correlations areas of approximately 25% were measured at low frequencies. While the noise generation was more efficient at the trailing edge of the isolated blade, more noise was radiated from the region near the leading edge.

Abstract

An investigation was performed of the broad band, aerodynamically generated noise in low tip-speed Mach number, centrifugal air moving devices. An interdisciplinary experimental approach was taken which involved investigation of the aerodynamic and acoustic fields, and their mutual relationship. The noise generation process was studied using two experimental vehicles: 1) a scale model of a homologous family of centrifugal blowers typical of those used to cool computer and business equipment, and 2) a single blade from a centrifugal blower impeller which was placed in a known, controllable flow field.

The radiation characteristics of the model blower were investigated by measuring the acoustic intensity distribution near the blower inlet and comparing it with the intensity near the inlet to an axial flow fan. Results showed that the centrifugal blower is a distributed, random noise source, unlike an axial fan which exhibited the effects of a coherent, interacting source distribution.

Aerodynamic studies of the flow field in the inlet and at the discharge to the rotating impeller were used to asses the mean flow distribution through the impeller blade channels and to identify regions of excessive turbulence near the rotating blade row. These studies included flow field qualification via flow visualization of the inlet field, and quantification of the flow velocities using single- and dual-channel hot film anemometry. Both circumferential and spanwise mean flow nonuniformities were identified along with a region of increased turbulence just downstream of the scroll cutoff. The fluid incidence angle, normally taken as an indicator of blower performance, was estimated from mean flow data as deviating considerably from an ideal impeller design.

New frequency-domain expressions for the correlation area and dipole source strength per unit area on a surface immersed in turbulence were developed which can be used to characterize the noise generation process over a rigid surface immersed in turbulence. The equations show that the correlation area may be thought of as a complex radiation efficiency which is normalized by its maximum value, the total area of the blade surface. Both the correlation area and the dipole source strength per unit area reflect the characteristics of the local turbulence regions and mutual interactions between regions.

An investigation of the noise radiated from the single, isolated airfoil (impeller blade) was performed using modern correlation and spectral analysis techniques. Radiation from the single blade in flow was characterized using these expressions for the correlation area and the dipole source strength per unit area, and from the relationship between the blade surface pressure and the incident turbulent flow field. Also, a computational fluid dynamics computer program was used to model the steady, two-dimensional flow over the single blade profile.

Results showed that radiation from the single blade was dominated by the effects of the incident turbulence. Normalized correlations areas of approximately 25% were measured at low frequencies. While the noise generation was more efficient at the trailing edge of the isolated blade, more noise was radiated from the region near the leading edge.

Table of Contents

List of Tables

List of Figures

List of Symbols

BEP	Best Efficiency Point or design point of an air moving device
c	Speed of sound
$E[\ ]$	Expectation operator
$\mathbf{F}[\ ]$	Fourier transform operator
f_i	Force in the i-th direction
dG_{pp}/dS	Dipole source strength autospectral density per unit area (mean square pressure)
G_{xx}	Autospectral density function (one-sided)
G_{xy}	Cross-spectral density function (one-sided)
$\hat{G}_{xy}$	Cross-spectral density with retarded time correction
G_{pp}	Autospectral density of acoustic pressure p
$G_{p_s p_s}$	Autospectral density of surface pressure p_s
G_{pp_s}	Cross-spectral density between acoustic and surface pressures
$G_{p'_s p_s}$	Cross-spectral density between surface pressures at different points
$(G_{p_s p_s})_{i,i}$	Autospectral density of surface pressure at location i
$(G_{p_s p_s})_{i,j}$	Cross-Spectral density between surface pressures at locations i,j
H_{ij}	Transfer function
I_h^c	Complex intensity in h-direction
k	Ensemble index
L	Characteristic dimension of turbulence
ℓ_j	Direction cosines
M	Mach number
p	Pressure
p_{ij}	Stokesian gas tensor
r	Source-to-Receiver distance
Re	Reynolds number
S	Strouhal number ($S = fd/U$)
S	Integration surface
S_a	Blade surface area
S_c	Correlation area
$\hat{t}$	Retarded time ($\hat{t} = t - r/c$)
T_{ij}	Lighthill's stress tensor

u_i, v_i	Total velocity in *i*-th direction
u'_i, v'_i	Fluctuating velocity in *i*-th direction
U_i, V_i	Mean velocity in *i*-th direction
U	Tangential blade velocity
$\vec{V}$	Total fluid velocity ($\vec{V} = \vec{V}_r + \vec{V}_x + \vec{V}_\theta$)
$\vec{V}_m$	Meridional fluid velocity ($\vec{V}_m = \vec{V}_x + \vec{V}_r$)
$\vec{V}_r$	Radial fluid velocity
$\vec{V}_x$	Axial fluid velocity
$\vec{V}_\theta$	Tangential fluid velocity
$\vec{W}$	Total fluid velocity relative to impeller
x_i, y_i	Component *i* of space vectors
$\vec{x}, \vec{y}$	Space vectors
$z(t)$	Substitution variable — time domain
$Z(f)$	Substitution variable — frequency domain
δ_{ij}	Kronecker delta
δ	Deviation angle ($\delta = \gamma_2 - \gamma'_2$)
γ_1	Inlet fluid angle
γ'_1	Inlet blade angle
γ_2	Outlet fluid angle
γ'_2	Outlet blade angle
ι	Fluid incidence angle ($\iota = \gamma_1 - \gamma'_1$)
μ	Viscosity
ν	Kinematic viscosity ($\nu_{air} = 15.7 \times 10^{-6} m^2/s$)
Ω	Rotational velocity of blade
ρ	Density
σ_c	Normalized correlation area or correlation radiation efficiency factor
τ	Time delay

Acknowledgments

As with most major works, this project represents the collective efforts of several people. I would especially like to acknowledge the following individuals for their support and guidance: Professor Gerald Lauchle, thesis advisor, whose technical and leadership abilities were instrumental throughout this project; Dr. George Maling, Jr. who, as my resident advisor, helped keep me focused on the end results, and whose ability to understand a technical problem appears to be without bounds; the remaining committee members, Dr. Robert Henderson, Dr. Martin Trethewey, and Dr. Philip Morris, for their suggestions and guidance during the project; and Dr. William Lang, Manager of the IBM Poughkeepsie Acoustics Laboratory, for his understanding and support. I would also like to express my gratitude to the IBM Corporation for supporting this research. Finally, the commitment to this endeavor has been a joint one, and would not have been possible without the enduring support and encouragement of my wife, Susan.

Chapter 1. Problem Formulation and Literature Review

1.1 *Discussion of Problem*

Many applications for air moving devices are noise sensitive — the computer industry, residential and commercial appliances, ventilating systems, etc. Typically, pumping requirements for the device are particular to the application, and hence the type of air moving device (i.e., axial, mixed flow, centrifugal, or transverse) is to some extent predetermined. Centrifugal devices have a distinct advantage over the other types; they generally produce greater static pressures (at the same speed and diameter) due to their ability to transfer a large amount of angular momentum to the fluid. Because of this characteristic, applications in the computer industry suitable for centrifugal blowers are growing in numbers. This is due primarily to the market demands for higher capacity processors which, in the final analysis, means higher packaging density for the electronics to be cooled, hence greater system resistance, and increased volumetric flow rate requirements for the air mover. Centrifugal blower noise is also normally free of any annoying discrete frequency sound energy, which means two things: 1) the perceived loudness is not magnified due to tonal energy, and 2) the noise sources are associated with random processes (turbulence).

In the hierarchy of noise control techniques, reduction of the source of the noise is strongly preferred over the other approaches of treatment of the path or treatment of the receiver. Reduction of the noise of an air moving device requires a basic knowledge of the noise source mechanisms present. While a vast literature exists on the noise radiated from an axial air moving device, little information currently is available on the basic structure of the noise sources of low-speed centrifugal blowers. As long as the random noise sources remain unresolved (physically within the air moving device, and conceptually for the researcher), the development of quieter, more efficient centrifugal blowers will continue to be inhibited by the lack of physical and acoustical knowledge. This thesis contains the results of an analysis and several sets of experiments performed with the objective of establishing a better understanding of the broad-band, aerodynamic noise source mechanisms present in a forward-curved centrifugal blower operating at low tip-speed Mach number (i.e., $M < 0.1$). A schematic representation of a centrifugal blower is shown in Figure 1.

1.2 Approach to Problem

As with any complex noise source, a basic understanding of the noise generation process of a centrifugal air moving device is, by nature, difficult to obtain, and at the same time fundamental to the effective treatment of or reduction of the noise source mechanisms. The complexity of the problem is indirectly demonstrated by a conspicuous void in the body of air moving device literature pertaining to the noise of low speed centrifugal blowers. Morfey's 1973 statement [63] still holds true nearly 15 years later: "Very little basic work has been done on the aerodynamic noise of centrifugal fans and blowers, despite their widespread use . . . "

In this case, the process of noise source identification involves relating the aerodynamic field inside of the air moving device to the radiated acoustic field by correlating, in a general sense, the flow phenomena with a local acoustic source or collection of sources. It is not enough to quantify each field (aerodynamic and acoustic) independently — the key is the cause-effect relationship between the fluid flow and the resulting noise. There are three possible approaches to this class of problem:

Cause-Effect Inference (Induction). By observing or measuring the effects of modifications to the environment, certain relationships may be established. For

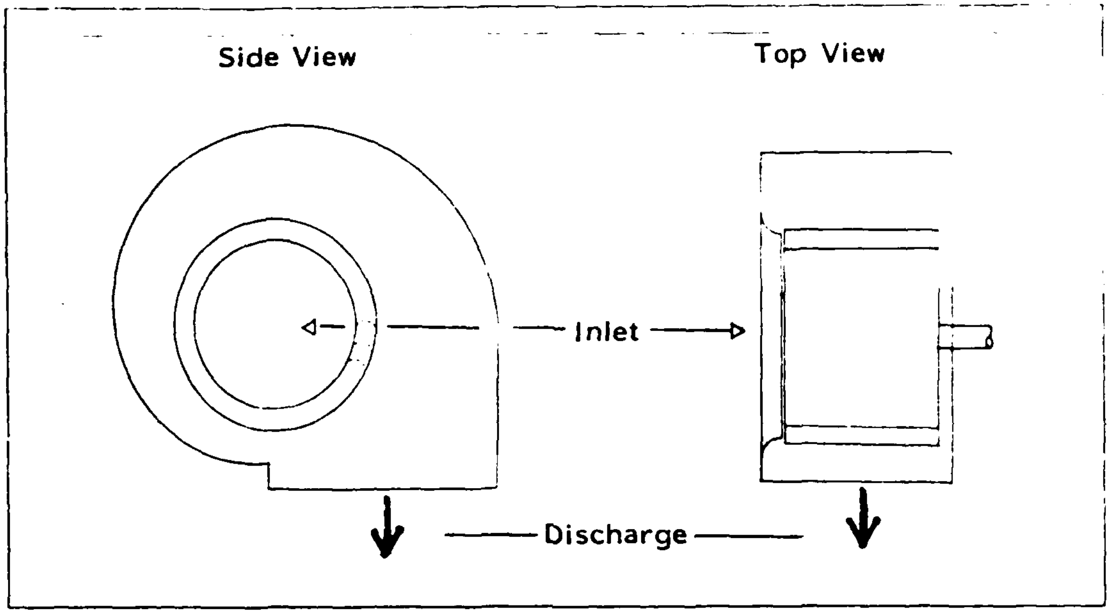

Figure 1. Schematic of Centrifugal Blower

example, a change in the operating point of the air moving device affects the noise. The changes in the noise spectrum may be attributed to the differences in the aerodynamic field such as the static pressure distribution across the blower and the different flow patterns over the individual blades. If a single parameter could be isolated, the resultant acoustical effects could be related to changes in that parameter. The challenge is to minimize the number of parameters affected by a single modification to the environment. Parametric studies utilize this approach.

Correlation by Association (Deduction). Deduction implies inference by means of reasoning based on general principles as opposed to observations. This approach entails detailed quantification of the aerodynamic and acoustic fields independently and establishing a relationship based on evidence external to the measurement system. An example is the inference of a region of increased noise from measurement of high turbulence levels near a blade surface, based on a knowledge of the relationship between turbulent fluctuations near a solid surface and the radiated acoustic noise. This approach requires an thorough understanding of the basic principles involved, and can be especially difficult when the individual source mechanisms are mutually masked. A case where deductive reasoning is particularly useful would be for identifying the source of a discrete tone in the spectrum related to the rotational frequency of the impeller.

Direct Evaluation. This method for identifying acoustic sources involves measurement of the correlation (cross spectral density) between aerodynamic and acoustic quantities, each characteristic of the respective field. When feasible, direct evaluation has obvious advantages over the previous two approaches, however, the practical difficulties associated with these types of determinations are often insurmountable (noise-to-signal ratio).

All three approaches just discussed were used to some degree in the research. A model centrifugal blower was constructed as the experimental vehicle for all of the measurements on a blower. (Results may be scaled using similarity relationships.) The overall acoustic field was quantified by determining the total radiated sound power spectrum as a function of blower operating point, and by determining the two-dimensional acoustic intensity distribution near the inlet to the air moving device. The aerodynamic field was evaluated via a systematic measurement of the mean and turbulent velocity levels near the rotating blade row inlet and exit. Measurements were concentrated near the impeller because it is believed to be the primary source of noise (as opposed to interactions with the rigid scroll surface). This belief is based on experiments which have shown that the acoustical effects of replacing the rigid scroll boundary with an acoustically *soft* boundary are at best minimal; certainly not indicative of dominant wall-interaction sources. Useful results were also obtained from efforts to visualize the flow field using aerodynamic visualization techniques.

In the final experimental phase, a set of measurements was performed on a single isolated impeller blade immersed in a known flow field. This was done for two primary reasons. First, equations were developed which allow estimates to be made of the frequency-dependent dipole source strength per unit area and correlation area[1] at an arbitrary point on the blade surface immersed in a turbulent flow field. Knowledge of these quantities provides important information on the relative strength of the aerodynamic noise sources on the blade surface and some measure of the efficiency of radiation of the local source mechanisms (i.e., the relative coupling with neighboring points). Since these measurements have not been reported in the literature before this thesis, it was important to explore the applicability of the equations and analysis using a relatively straightforward aerodynamic noise source (i.e., a single blade in a known flow field as opposed to a rotating impeller in a scroll housing). The second motivation for the single blade experiments was to be able to deductively infer aerodynamic-acoustic relationships in the operational model blower from a detailed knowledge of the single blade radiation mechanisms; the single blade characteristics not otherwise available for the rotating impeller due to the practical difficulties associated with making measurements in the rotating reference frame.

All measurements in the final experimental phase were made in a stationary reference frame. There was no possibility of obtaining valid cross spectral data between the blade surface pressures and the radiated acoustic field in a moving reference frame for at least two reasons. First, instrumentation presents a challenge due to the susceptibility of the miniature transducers to extraneous noise and the requirement for

---

[1] These terms will be defined in the next chapter.

routing the signals through a slip ring. Second, measurements made on a single blade in a stationary frame indicate that the rotating frame signal would be far below the overall noise floor produced by radiation from all 26 blades on the impeller.

1.3 Literature Review — Centrifugal Blower Noise

Studies on the noise radiated by centrifugal blowers may be classified into two major categories: 1) acoustic investigations in which little or no aerodynamic work was done, or 2) aerodynamic investigations where the radiated acoustic noise was inferred from aerodynamic measurements. In both categories, the relationship between the aerodynamic turbulence and radiated noise was seldom evaluated directly. The following brief review of the literature will cover fluid dynamic investigations of centrifugal blower internal flow structures, general blower noise investigations, effects of geometry on noise generation from a centrifugal blower, narrow- and broad-band noise reduction techniques, and finally, references to more extensive literature reviews of centrifugal blower noise.

Both theoretical and experimental fluid mechanic investigations of the flow field in a centrifugal impeller have appeared in the literature. The device-independent studies (i.e., related to airfoil response and flow patterns and not necessarily applied to axial or centrifugal air moving devices) are largely theoretical with emphasis on the lift and pressure fluctuations and response of an airfoil immersed in flow. The literature is rich in this area [33, 35, 37-39, 66]. Examples of experimental investigations of isolated airfoils are given in References [1, 19, 32, 64, 98]. The aerodynamic experimental studies of centrifugal blowers largely focus on identifying the mean and fluctuating flow patterns which exist in a centrifugal air moving device [2, 27, 36, 43, 61, 78, 79], and on effects of various parameters (e.g., inlet turbulence) on the steady flow field [42, 81, 95].

The topic of general blower noise includes studies on dimensional analysis and similarity laws as they apply to the radiated noise. The first frequency-independent fan laws were established by Madison [56] in 1949. Frequency dependence was not incorporated into the fan laws until 1963 when Maling [57] published a generalized spectral function for centrifugal blower noise based on the operating point of a homologous family of blowers as a function of a normalized frequency parameter. Other investigations of similarity laws for blowers have included discrete frequency tones [67, 71]. In addition to similarity laws, discussions on the nature of centrifugal blower noise sources have been published [7, 41].

The influence of geometrical parameters on the noise generated by a centrifugal blower is critical to the designer. The results of four independent parametric studies were published in the 1970s [8, 47, 62, 84] on the subjects of inlet conditions (2 papers), scroll housing effects, and impeller geometry, respectively.

Noise reduction techniques for centrifugal blowers have primarily concentrated on reduction of the rotor-stator interactions at the scroll cutoff (blade passage frequency tone, or BPF). Increasing the cutoff decreases the strength of the tone, but also adversely affects the air performance of the blower. While it is recognized that these effects depend on the specific fan application, increasing the cutoff normally provides sufficient attenuation of the discrete tone [29, 89]. Alternative methods for reducing the BPF include 1) a streamlined cutoff geometry [76], 2) circumferentially offset blade row at center septum [55], 3) spatial modulation of the blade spacing [48], 4) inclined blades relative to cutoff (or vice versa) [29], and 5) acoustical resonators located at the cutoff region, where the BPF is generated, and tuned to the harmonics related to the blade rotational speed [45, 46, 72, 99]

Broad band noise reduction has been less successful than reduction of pure tone levels, since the mechanisms are not well understood. Techniques have been limited to various housing treatments such as bulk absorbers [9, 59], or flow-resistive materials backed by a sealed plenum [96]. A notable exception to the bulk absorber approach was reported by Petrov and Khoroshev [75] in 1971 who applied transition meshes to the inlet and outlet of the blade channels of a centrifugal impeller using fine wire screen. They explained that the inlet mesh served to reduce the scale of the ingested large-scale turbulence, thereby acting as an agent for the cascade process in which turbulent energy is transferred from the large scales (low frequency) into smaller scales (high frequency) for eventual viscous dissipation. This spectral redistribution to higher frequencies is also advantageous in terms of psychoacoustic annoyance criteria. For an ingested field devoid of large scale eddies, the inlet mesh creates small scale turbulence over the blade surface and helps to extend the separation point, especially for a forward curved blade design which tends to exhibit suction side separation. The outlet mesh is said to provide a more uniformly distributed outlet flow, again by way of conversion of large scale turbulence. The price paid for the use of transition meshes is a pressure loss associated with the turbulence generation process and flow through the screens.

Another method for producing small scale turbulence over the blade surface was the subject of a West German patent [93] (the United Kingdom counterpart is referenced here), where the inventor describes a set of edge serrations to be applied to the leading (and trailing) edges of the centrifugal impeller, which is "responsible for a turbulent boundary layer on the face of the blade helping to put an end to noise-producing instabilities and shedding of vortices." The concept of edge serrations has been applied to axial flow devices by several researchers (see, for example, Arndt and Nagel [6]), but use of serrations with centrifugal impellers is not common. Experiments performed within IBM on the use of edge serrations on centrifugal impellers showed that the serrations were not effective in reducing the overall noise levels, but a minimal amount of spectral redistribution was achieved.

There have been a number of reviews published on noise reduction of centrifugal blowers. The most notable are those by Neise [68-70] and Mugridge [65].

1.4 Research Objectives

The purpose of this research is to investigate the generation and radiation of broad band, random, aerodynamically-generated noise of a forward-curved, low Mach number centrifugal blower. The investigation has the following objectives:

Source Characterization — Investigate the overall characteristics of a family of forward-curved centrifugal blowers. In particular, examine the acoustic radiation characteristics and the gross mean flow patterns and their interrelationships. In addition, investigate the radiation from a single, isolated blade immersed in a flow field typical of that found in a centrifugal blower.

Numerical Modelling — Investigate the application of computational fluid dynamics algorithms and implementations to flow through a centrifugal blower impeller. Develop a model for the flow over a single blade and evaluate its effectiveness in simulating realistic flow patterns over the airfoil.

Source Identification and Ranking — Identify and make an estimate of the relative strength of the aerodynamic noise source mechanisms in a centrifugal blower using both aerodynamic and acoustic measurements, and employing modern multichannel signal analysis techniques (i.e., correlation and spectral analysis).

1.5 Outline of Thesis

The thesis is presented in the progression of theory, description of experiments, experimental results, and conclusions. The experimental results comprise over half of the thesis, and thus contain the primary contribution of the research to the field. A portion of the experimental results, however, utilize an approach to the analysis of aerodynamic noise which is developed in the theoretical portion of the thesis as an extension of earlier work by Siddon [88] and Sharland [86].

The theoretical section of the thesis is presented in Chapter 2, "Theory of Aerodynamic Noise Generation." This section begins with a brief introduction to the Lighthill's Acoustic Analogy theory of aerodynamic noise generation. The remainder of the chapter is devoted to the development of frequency-domain expressions for estimating the correlation area, and the dipole source strength per unit area based on both the mean square acoustic pressure radiated to the far field and the acoustic intensity. Some of the equations are new while others are extensions of Siddon's time-domain expressions into the frequency domain. These equations are used in the experimental investigation of the noise radiated by a single impeller blade immersed in flow (Chapter 6). In addition to the derivations, a physical interpretation of the analysis is presented using a multiple input/output model approach.

Chapter 3, "Overview of Hardware Design and Test Facilities," contains the general descriptive information of the various experiments reported in following chapters. The design of the experimental hardware is presented along with a brief review of dimensional analysis used for scaling. This section also includes a description of the acoustical facilities and the data analysis procedures used.

Chapter 4, "General Blower Characterization," presents experimental results of the acoustical and aerodynamic characterization of the model centrifugal blower, in terms of the external field properties (i.e., radiated power, acoustic intensity distribution around the the outside of the blower, and the overall air performance). Measurement of the air performance was a prerequisite for the rest of the experiments since the primary objective was to quantify the blower noise when operating at the design point, which is the point of maximum efficiency.

The results of aerodynamic measurements made inside the blower housing, near the rotating blade row, are presented in Chapter 5, "Aerodynamic Measurements in Model Blower." Mean and turbulence velocity components were measured at the blade leading and trailing edges at 40 different locations. The results of these measurements were used to infer mean and turbulent distributions around the impeller, thereby providing information of the distribution of the related aerodynamic noise mechanisms. Discussions on the interpretation of the hot film anemometer data are included. In addition, flow visualization experiments were performed and recorded on video tape. The tapes have proven invaluable in assessing the validity of mean and turbulent flow patterns deduced from the experimental data. The results of the flow visualization experiments are presented. This section also contains an application of the measured data to a cascade model of the impeller. Cascade analysis provides information on the gross flow patterns over an individual blade based on experimental data, and is commonly used in the design and analysis of air moving devices.

An investigation was performed on the radiation of noise from a single impeller blade immersed in a known, controllable flow field (jet flow). These results are given in Chapter 6, "Single Blade Investigations." This set of experiments was motivated by the possibility of relating the noise radiation characteristics of a single, isolated blade, immersed in a flow field simiar to that typically found in the model centrifugal blower to the noise generation process in the operational blower. Blade surface pressures were measured as well as the coherence between surface pressures at two points on the blade separated by a streamwise or chordwise distance. The dipole source strength per unit area and correlation area was also determined from estimates of the cross spectrum between the blade surface pressure and the radiated acoustic pressure. These measurements represent the best method currently available for directly determining the (acoustic) strength of the aerodynamic source regions on a centrifugal fan blade and were based on the equations developed in Chapter 2.

A summary of the experimental results is presented in the final chapter, Chapter 7, "Conclusions and Recommendations for Future Work."

Chapter 2. Theory of Aerodynamic Noise Generation

This chapter contains the theoretical results of the thesis. First, a general review of aerodynamically generated noise will be presented, beginning with Lighthill's Acoustic Analog theory and Curle's extension to include the effects of solid boundaries. A brief review of edge noise follows with emphasis on the experimental work of Brooks and Hodgson [17] and how edge noise pertains to the present problem.

Finally, Section 2.2, "Frequency Domain Analysis," contains the primary theoretical results of the thesis. In that section, a frequency domain analysis of radiated noise from a rigid surface will be presented as an extension of the time-domain results of Siddon [88] whose work was based on that of Sharland [86] and Curle [23]. Some of the expressions developed are new while others are *modernized* versions of previously published work. The expressions are cast in a form that is suitable for application to noise source identification and source strength mapping using multiple input/output analysis. Practical aspects of using the theory are also discussed. An application of the analysis is presented in Section 6.2, "Experimental Investigations Using Frequency Domain Theory."

2.1 Aerodynamically Generated Noise

2.1.1 Acoustic Analog Theory

The analytical foundations for the investigation of sound generated by fluid turbulence were established in 1952 by Lighthill [53, 54]. Part I of Lighthill's General Theory [53] adopted a rather straightforward approach which was quite similar to the classic treatment of Reynolds stresses [82]: by comparing the equations of density for a (turbulent) fluid in motion with those of a uniform acoustic medium at rest, and considering the differences to be attributable to the effects of a fluctuating external force acting on the acoustic medium, Lighthill was able to formulate an equation which describes aerodynamic sound generation in terms of a forcing function:

$$\frac{\partial^2 \rho}{\partial t^2} - c^2 \frac{\partial^2 \rho}{\partial x_i \, \partial x_i} = \frac{\partial^2 T_{ij}}{\partial x_i \, \partial x_j} \, . \tag{2.1}$$

Here, ρ is the total density ($\rho = \rho_o + \rho'$), c is the speed of sound, and the instantaneous applied stress tensor at a point is given by,

$$T_{ij} = \rho u_i u_j + p_{ij} - c^2 \rho \delta_{ij} \, , \tag{2.2}$$

where u_i is the total velocity ($u_i = U_i + u'_i$) in the i-th direction and δ_{ij} is the Kronecker delta. The Stokesian gas stress tensor, p_{ij}, is,

$$p_{ij} = p\delta_{ij} - \mu \left[\frac{\partial u_i}{\partial x_j} + \frac{\partial u_j}{\partial x_i} - \frac{2}{3} \left(\frac{\partial u_k}{\partial x_k} \right) \delta_{ij} \right] \tag{2.3}$$

where μ is the coefficient of viscosity and p is the total pressure ($p = p_o + p'$). Derivations of Equation (2.1) are given in the literature in more detail than was included in the original work. See, for example, Dowling and Ffowcs-Williams [25].

The left-hand side of Equation (2.1) describes the propagation of sound in a uniform medium at rest (i.e., the acoustic wave equation). The right-hand side serves as a source term which contains the effects of sound generation, convection with the flow, variable propagation speed (i.e., finite amplitude), and viscous dissipation. That is, with relatively insignificant assumptions (adiabatic sound propagation and isotropic, Newtonian fluid), Equation (2.1) is an exact description of the density fluctuations: "Hence the density fluctuations in the real flow must be exactly those which would occur in a uniform acoustic medium subject to the external stress system given by the difference, T_{ij}, between the effective stresses in the real flow and the stresses in the uniform acoustic medium at rest [53]." The form of the source term, a double divergence of a stress tensor, indicates a quadrupole source distribution.

The acoustic density fluctuations at a point in space $\vec{x}$ in an unbounded medium are given by Lighthill as the solution to Equation (2.1) in the form of a volume integral over the source region V,

$$\rho' = \rho - \rho_o = \frac{1}{4\pi c^2} \frac{\partial^2}{\partial x_i \, \partial x_j} \int_V T_{ij}\left(\vec{y}, t - \frac{|\vec{x} - \vec{y}|}{c}\right) \frac{d\vec{y}}{|\vec{x} - \vec{y}|} \qquad (2.4)$$

where the integrand is the stress field evaluated at the retarded time. The essence of Equation (2.4) lies in the nature of the sources which may be regarded as a field of quadrupoles whose strength per unit volume is the stress tensor T_{ij}. Thus, if the flow field is known, the acoustic density fluctuations may be obtained using Equation (2.4).[2]

The relationship between the total radiated power and various dimensional parameters was also established by Lighthill [53] using dimensional analysis arguments.

---

[2] The primary limitation to Lighthill's theory is the requirement of *a priori* knowledge of the flow field stress tensor.

The radiated sound power W_Q of a given turbulence region of characteristic dimension L is related to the mean-flow Mach number M and the speed of sound c by

$$W_Q \propto \rho_o c^3 L^2 M^8 . \tag{2.5}$$

The above solution is valid for an unbounded medium at rest in which the turbulent source region is imbedded, an example being an imbedded jet. If a solid boundary is introduced into the source region, then additional terms must be included in the solution of Equation (2.4) to account for the fluctuating forces acting on the fluid by the boundary. This extension to Lighthill's theory was developed by Curle [23] in 1955, whose expression for the acoustic density fluctuations includes a surface integral as well as the volume integral of Equation (2.4):

$$\rho' = \frac{1}{4\pi c^2} \frac{\partial}{\partial x_i} \left[\frac{\partial}{\partial x_j} \int_V \frac{T_{ij}\left(\vec{y}, t - \frac{r}{c}\right)}{r} \, d\vec{y} - \int_S \frac{P_i\left(\vec{y}, t - \frac{r}{c}\right)}{r} \, d\vec{y} \right] \tag{2.6}$$

where P_i is the force per unit area exerted on the fluid in the x_i direction, $(P_i = \ell_j \, p_{ij})$, ℓ_i are the direction cosines for the outward normal from the fluid, p_{ij} is the stress tensor given in Equation (2.3), $r = |\vec{x} - \vec{y}\,|$, is the distance from the integration point on the surface to the receiver in the acoustic field removed from the mean flow, and the surface integral is over the surface of the boundary. It is readily shown that the boundary-induced term is, "exactly equivalent to the sound generated in a medium at rest by a distribution of dipoles of strength P_i per unit area, and P_i is exactly the force per unit area exerted on the fluid by the solid boundaries in the x_i direction [23]." Curle used dimensional arguments similar to Lighthill's to deduce the dependence of sound power on the flow field variables:

$$W_D \propto \rho_0 c^3 L^2 M^6 \qquad (2.7)$$

which implies that the importance of surface dipole terms increases significantly at low Mach number relative to the volume quadrupole terms. The estimates of Equations (2.5) and (2.7) were based on the assumption that both the volume and surface regions are *compact*, which means that retarded time differences have been ignored over the source regions. This assumption is valid for low Mach numbers only since the source region becomes of the order of an acoustic wavelength as the characteristic velocity approaches the speed of sound. Dowling and Ffowcs-Williams [25] show that, for $M \geq 1$ the radiated power is proportional to M^3 rather than M^8 for low Mach numbers.

For large Reynolds numbers, the viscous stress components of T_{ij} may be neglected. Also, at low Mach numbers, the acoustic density fluctuations are a small proportion of the ambient density. Therefore, the applied stress tensor may be approximated by the fluctuating Reynolds stress; $T_{ij} \sim \rho_0 u_i u_j$. This approximation was set forth by Lighthill. What this shows is the nature of the quadrupole source terms. For $i = j$ the velocity components are aligned and the dominant sources may be thought of as longitudinal quadrupoles in which the fluid is stretched and compressed. For $i \neq j$ the quadrupoles are comprised of opposing dipoles with aligned dipole moments spaced a small distance apart (i.e., lateral quadrupoles). This configuration generates sound by applying fluctuating shearing forces to the fluid.

The Lighthill-Curle Acoustic Analogy theory provides an exact solution for aerodynamically generated noise, where the noise generation is contained within a fixed volume. The derived wave equation, Equation (2.1), contains the effects of fluid viscosity, convection, Reynolds stress, and compressibility. While the equation is exact, convection effects are imbedded in the forcing functions (i.e., the stress tensor of the right-hand side of Equation [2.1]). Since the left-hand side of Equation (2.1) describes an acoustic medium at rest, the solutions must be considered *effective* density fluctuations that would propagate in a stationary medium under the stress system described by the forcing functions. For example, in the far field of a jet, the acoustic medium is removed from the flow field and the solution ρ given by Equation (2.6) is exact. However, for turbulent boundary layer flow over a plate, where the receiver is located in the mean flow field, the acoustic field is more accurately described by including convection in the wave equation rather than in the forcing function. This particular point was discussed by Tam [90].

2.1.2 Edge Effects

It is well known that the radiation from a semi-infinite flat plate immersed in flow is significantly increased at low Mach number by the presence of the plate edge. Mathematically, the edge represents a spatial discontinuity which may be accounted for using a Green's function approach in which the eddy interactions are important in the acoustic near field [31]. Other theoretical approaches have been formulated for edge noise. A review of edge noise theories was presented by Howe [40] in which several different edge noise models developed by researchers were consolidated into one, unified theory. Confusion persists on the exact mathematical treatment of the edge boundary condition (application of the Kutta condition), but the underlying result is that the edge noise scales with the *fifth* power of the characteristic eddy convection velocity, which is slightly more efficient than the surface dipole terms (M^6), and considerably more efficient than the volume quadrupole sources (M^8), assuming small values of the Mach number M (compare Equations [2.5] and [2.7], for volume and surface radiation).

While theoretical developments have progressed considerably, experimental investigations have been limited due to the measurement complexity, with a few notable exceptions. Specifically, Brooks and Hodgson [17] confirmed the fifth power relationship between the radiated noise and convection velocity by relating the surface pressure statistics to the trailing edge noise of an airfoil immersed in flow with the noise due primarily to the tripped turbulent boundary layer over the airfoil. They concluded that the turbulent boundary layer flow past a sharp trailing edge was not affected by the edge, assuming the top and bottom turbulent flow fields were statistically independent. A blunt edge, however, produces additional noise due to a coherent vortex structure.[3] The blade surface pressure represents a superposition of the scattered edge field and the incident field (either from the turbulent boundary layer or the external field turbulence).

2.2 Frequency Domain Analysis

In this section, frequency domain expressions are developed which describe the relationship between the surface pressures on a plane, rigid boundary immersed in flow, and the radiated acoustic pressure at some point distant from the boundary. More specifically, it is shown that the mean square acoustic pressure in space resulting from stress fluctuations at the surface of a boundary (e.g., a centrifugal fan blade) in flow may be obtained by integrating (over the boundary) the cross-spectral density between the (retarded time) surface pressure and the farfield acoustic pressure. In addition to the expression for the mean square acoustic pressure, a formulation is presented for the

---

[3] Coherent shedding from a blunt trailing edge was also investigated by Blake [16] who developed an analytical formulation to relate the coherent, wake-induced pressures to the characteristics of the near-edge wake.

acoustic intensity and the correlation area on the blade surface. The frequency-domain expressions developed in this section are, for the most part, original to this work. In some cases (correlation area and dipole source strength per unit area), parallel developments were adapted from previous work which used time-domain analysis, however, the final equations are new.

The expression for the noise generated by a volume of turbulence containing a solid boundary was first derived by Curle [23], and is given here in an expanded form of Equation (2.6) which was used by Siddon [88]:

$$c^2\rho(\vec{x},t) = \int_S \left[\frac{\partial}{\partial t}(\rho u_n) \right] \frac{dS}{4\pi r} - \frac{\partial}{\partial x_i} \int_S \left[f_i + \rho u_i u_n \right] \frac{dS}{4\pi r} - \frac{\partial^2}{\partial x_i \partial x_j} \int_V \frac{[T_{ij}]}{4\pi r} dV \tag{2.8}$$

where the square brackets [ ] indicate that the term is evaluated at the retarded time $\hat{t} = t - r/c$, and f_i is the local stress acting at the surface (shear and normal). For a rigid, stationary surface the normal velocity of the surface $u_n = 0$. By neglecting the quadrupole source terms (the volume integral), and limiting the solution to the acoustic and geometric far field, the acoustic pressure is due to a surface integral of the time derivative of the stress components. If we also assume that only the *normal* stress is of importance [88] (i.e., neglect shear stress), then the following form may be used for the acoustic pressure:

$$p(\vec{x},t) \cong \left(\frac{\cos\theta}{4\pi x c} \right) \int_{S} \frac{\dot{p}(\vec{y},\tau)}{r} \, dS(\vec{y}) \tag{2.9}$$

In this form the dipole nature of the source term is evident due to the time derivative of a fluctuating force on the fluid. This convenient expression for the acoustic pressure due to the normal stress fluctuations at the surface forms the basis for the subsequent analysis.

It is instructive to examine Equation (2.9). The acoustic pressure at a spatial location $\vec{x}$ at time t is determined by contributions from the surface pressure (actually the time derivative of the surface pressure) over the entire surface at an earlier time τ. Since $r = |\vec{x} - \vec{y}\,|$ is the distance from the surface point of integration to the far field point, the retarded time is dependent on the surface point location $\vec{y}$. Thus, in order to account for retarded time *differences* over the surface, all $r-$dependency must be retained within the integral over $S(\vec{y}\,)$. Secondly, neglecting the shear stress means that the source terms are assumed to be associated with the normal surface pressure. The angle dependency in Equation (2.9) is indicative of the orientation of the dipole source model perpendicular to the surface. Thus, for a plane surface the radiation from opposing faces includes a change in sign due to the direction of the unit normal vector. This is accounted for in the (dipole) cosine directivity factor.

2.2.1 Dipole Source Strength – dGpp/dS

For a fixed far field location, the acoustic pressure is comprised of contributions from the entire blade surface – superposition. The individual pressure contributions are superimposed at $\vec{x}$ in a *coherent* manner, hence the amplitude and phase of the pressure combine to form the total pressure. The total power of a source is related to the integral over a closed surface surrounding the source of the normal acoustic energy flux (intensity). Thus, at a point on the integration surface the power is directly related to the active intensity, or, for plane waves or in the far field or spherical waves from a point monopole, to the mean square acoustic pressure. An expression for the contribution to the mean square acoustic pressure at a point in space by the surface dipoles will be developed.

For $p(\vec{x}, t)$ and $p_s(\vec{y}, t)$ stationary, ergodic random processes $\{p_k\}$ and $\{p_{s_k}\}$, the finite Fourier transforms over the k-th record of length T are:

$$P_k(\vec{x}, f, T) = \int_0^T p_k(t) e^{-j\omega t} dt \tag{2.10}$$

$$P_{s_k}(\vec{y}, f, T) = \int_0^T p_{s_k}(t) e^{-j\omega t} dt \, . \tag{2.11}$$

Then, by definition the two-sided spectral density functions are

$$S_{pp_s} = \lim_{T \to \infty} \frac{1}{T} E\left[P_k^*(\vec{x}, f, T) P_{s_k}(\vec{y}, f, T) \right] \tag{2.12}$$

$$S_{pp} = \lim_{T \to \infty} \frac{1}{T} E\left[\, | P_k(\vec{x}, f, T) |^2 \right] . \tag{2.13}$$

Also, the single-sided spectral density $G_{12} = 2S_{12}$. Introducing a substitution variable, $z(t) = \partial p_s/\partial t$, Equation (2.9) becomes

$$p(\vec{x},t) = \left(\frac{\cos\theta}{4\pi xc} \right) \int_S z(\vec{y},\hat{t})\, dS(\vec{y}) . \qquad (2.14)$$

Taking the finite Fourier transform of the k-th record of Equation (2.14)

$$P_k(\vec{x},f,T) = \left(\frac{\cos\theta}{4\pi xc} \right) \int_S \hat{Z}_k(\vec{y},f,T)\, dS \qquad (2.15)$$

where $\hat{Z}_k$ is the finite Fourier transform of the substitution variable $z(\hat{t})$ evaluated at the retarded time, $\hat{t}$.

Note: The retarded time evaluation introduces a bias error in the finite transform estimate due to the evaluation of $\hat{Z}_k$ from a time record of length T, but offset from the time record used for P_k by the amount of the time delay $\tau = r/c$. In practice the bias may be minimized by making $\tau << T$, or eliminated by aligning the time records before performing the transforms. The bias error results from the *finite* transforms and is removed by the limitation operation ($T \to \infty$) taken on the expected value to yield the analytic relationship. **For this analysis the bias will be taken as zero by virtue of aligned data records.** See Bendat and Piersoll [15] and Seybert and Hamilton [85] for further discussion of time-delay bias errors.

Two Fourier transform properties

$$\mathbf{F}\left[z(\hat{t})\right] = \hat{Z}(f) = e^{-j\omega r/c} Z(f) \tag{2.16}$$

and

$$\mathbf{F}[z(t)] = Z(f) = j\omega P_s(f) \tag{2.17}$$

allow Equation (2.15) to take the form

$$P_k(\vec{x},f) = \left(\frac{\cos\theta}{4\pi x c} \right) \int_S j\omega e^{-j\omega r/c} P_{s_k}(\vec{y},f)\, dS(\vec{y})\,. \tag{2.18}$$

Multiplying by the conjugate of the acoustic pressure spectrum gives

$$P_k^*(\vec{x},f)P_k(\vec{x},f) = \left(\frac{\cos\theta}{4\pi x c} \right) \int_S j\omega e^{-j\omega r/c} P_k^*(\vec{x},f) P_{s_k}(\vec{y},f)\, dS(\vec{y})\,. \tag{2.19}$$

The autospectral density is obtained by applying the expectation operator E over the ensemble index k to both sides of Equation (2.19). The true autospectral density requires taking the limit of the expected value divided by T as $T \to \infty$. The final expression is given here in terms of the one-sided cross- and autospectral density functions.

$$G_{rp} = \left(\frac{\cos\theta}{4\pi x c} \right) \int_S j\omega e^{-j\omega r/c} G_{rp_s}\, dS\,. \tag{2.20}$$

Differentiating Equation (2.20) gives an expression for the contribution to the mean square acoustic pressure G_{rp} **per unit area** by the dipole sources associated with the blade surface pressures.

$$\frac{dG_{rp}}{dS} = \left(\frac{\cos\theta}{4\pi x c} \right) j\omega\, e^{-j\omega r/c} G_{pp_s}\,. \tag{2.21}$$

This term is called the **dipole source strength** after Siddon who developed a similar expression for time domain quantities (i.e., dG_{rp}/dS was cast in terms of the τ derivative of the cross correlation function [88]) and a frequency domain version based on a modified definition of the cross spectrum. Since G_{rp} is real, the real part of Equation (2.21) is taken for the final expression for the dipole source strength per unit area (in units of mean square pressure per unit area):

$$\frac{dG_{rp}}{dS} = -\frac{\omega\cos\theta}{4\pi x c}\ \mathrm{Im}\left[e^{-j\omega r/c} G_{rp_s} \right]. \tag{2.22}$$

The full expression for the dipole source strength per unit area, given by Equation (2.21), is complex; the imaginary components being related to the non-propagating field. A detailed discussion of the interpretation of the dipole source strength per unit area is given in the following sections.

2.2.2 Acoustic Intensity — dI/dS

In this section an expression for the acoustic intensity is derived based on the finite-difference approximation. The approach used here was adapted from Elko [28] who derived the cross-spectral representation of the acoustic intensity for stationary, ergodic signals from a pair of closely spaced pressure microphones.

The complex acoustic intensity at a point $\vec{x}$ in the acoustic field is given by the following equation:

$$I_h^c = p\vec{u}_h = \left(\frac{\cos\theta}{4\pi x c} \right) \int_S \left[\frac{\partial p_s(\hat{t}, \vec{y})}{\partial t} \right] \vec{u}_h \, dS \qquad (2.23)$$

where $\vec{u}_h$ is the instantaneous acoustic particle velocity at a point $\vec{x}$ in an arbitrary direction denoted h. Applying the finite-difference approximation[4] to $\vec{u}_h$ yields, for the integrand **L** in Equation (2.23):

$$\begin{aligned} \mathbf{L} &= \left[\frac{\partial p_s(\hat{t}, \vec{y})}{\partial t} \right] \vec{u}_h \\ &= \frac{\left[z(\hat{t})\, w_2(t) \right] - \left[z(\hat{t})\, w_1(t) \right]}{-\rho \Delta h} \end{aligned} \qquad (2.24)$$

---

[4] The finite-difference approximation assumes that the difference between two closely spaced pressures can be used to approximate the pressure gradient. Euler's equation relates the pressure gradient to the time derivative of the particle velocity: $\partial \vec{u}_i / \partial t = -(1/\rho)\partial p / \partial \vec{x}_i$.

where the following substitution variables were used:

$$z(t) = \frac{\partial p_s(t)}{\partial t} \quad ; \quad w_i(t) = \int p_i(t) dt, \tag{2.25}$$

and, where $p_i(t)$ is the acoustic pressure at position i $(i = 1,2)$ on either side of the field point $\vec{x}$, aligned in the h—direction (see Figure 2). Then using the Parseval relation, where $R_{zv}(0)$ is the cross correlation between z and v evaluated at zero time delay,

$$R_{zv}(0) = E[z(t)v(t)] = \int_{-\infty}^{\infty} S_{zv}(\omega) \, df. \tag{2.26}$$

Using the frequency domain relationships,

$$\begin{aligned} S_{x\hat{z}} &= e^{-j\omega r/c} \; S_{xz} \\ S_{zx} &= j\omega \; S_{p_s x} \\ S_{xw_i} &= \frac{1}{j\omega} \; S_{xp_i} \end{aligned} \tag{2.27}$$

in Equation (2.24) yields,

$$\int_{-\infty}^{\infty} L(\omega) \; \frac{d\omega}{2\pi} = - \frac{1}{\rho \Delta h} \int_{-\infty}^{\infty} e^{-j\omega r/c} \left[S_{p_s p_2} - S_{p_s p_1} \right] \frac{d\omega}{2\pi} \, . \tag{2.28}$$

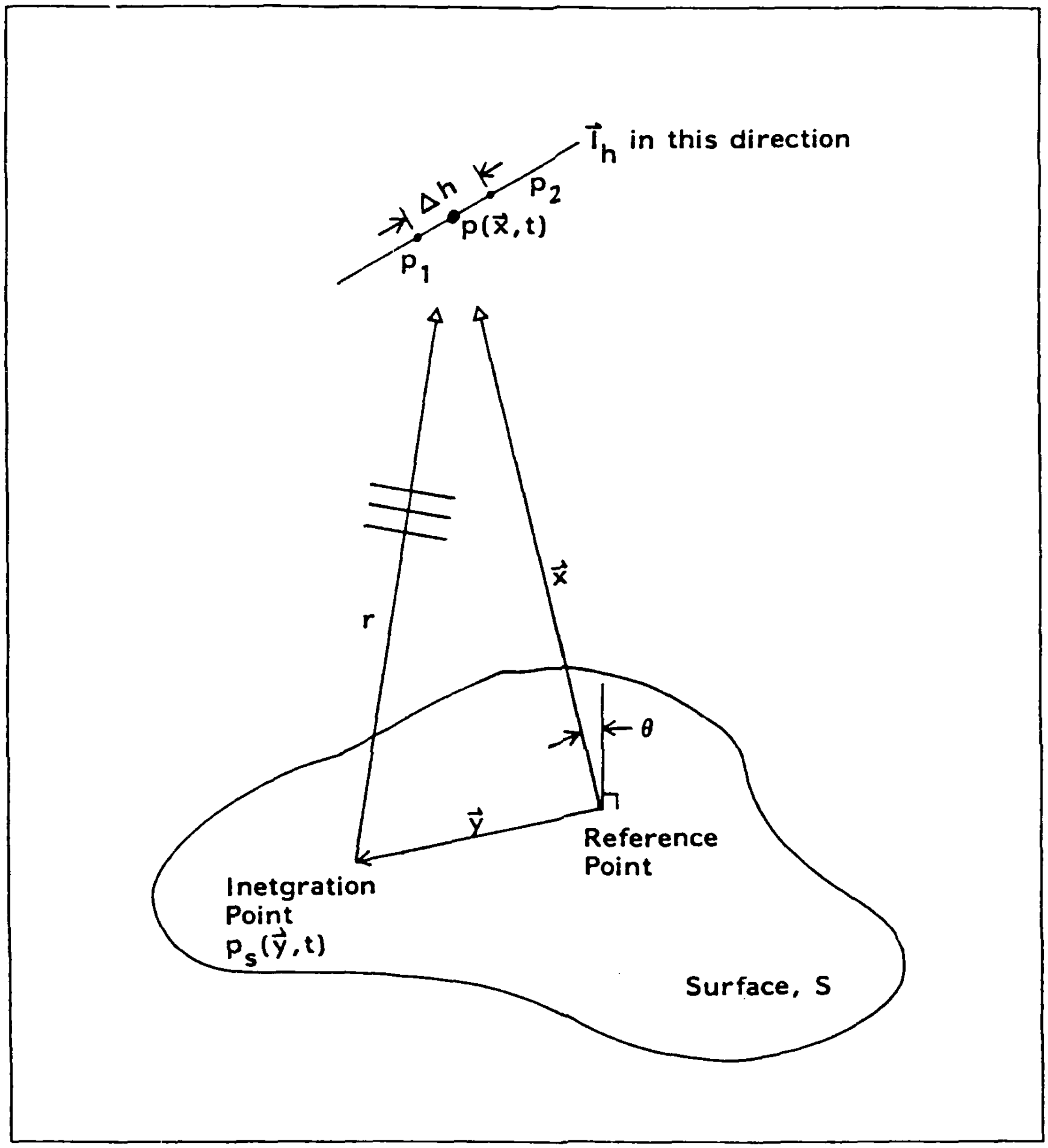

Figure 2. Schematic of Intensity Estimate and Related Terminology

It follows that the complex intensity is,

$$I_h^c(\omega) = \frac{\cos\theta}{4\pi x c\rho\Delta h}\int_S e^{-j\omega r/c}\left[S_{p_sp_2} - S_{p_sp_1}\right]dS \qquad (2.29)$$

$$= I_h(\omega) + jQ_h(\omega)$$

The real part of Equation (2.29), I_h is termed the *active* intensity and is related to the propagation of acoustic energy. The imaginary part Q_h, or the *reactive* intensity, characterizes the non-propagating portion of the acoustic field. From Equation (2.29), the active intensity is given by,

$$\frac{dI_h(\omega)}{dS} = \frac{\cos\theta}{8\pi x c\rho\Delta h}\left[\hat{C}_{p_sp_1} - \hat{C}_{p_sp_2}\right] \qquad (2.30)$$

where the hat denotes the phase shift correction of the cross spectrum,

$$e^{-j\omega r/c}G_{xy} = \hat{G}_{xy} = \hat{C}_{xy} + j\hat{Q}_{xy}\,. \qquad (2.31)$$

Equation (2.29) and Equation (2.30) represent a means for estimating the contribution, per unit area, to the acoustic intensity by the sources associated with the normal component of the fluctuating stress field near the surface of an airfoil or other solid object immersed in flow. The intensity is determined from the difference between the real parts of the cross spectra measured between the surface pressure and each of the two, closely spaced pressure microphones located in the acoustic field.

This expression provides all of the benefits of examining the intensity field as opposed to using the plane-wave assumption for the intensity, namely the mean square pressure divided by the characteristic impedance of the medium.

2.2.3 Correlation Area — Sc

The concept of correlated regions of turbulent eddies interacting with the solid surface implies a surface area, or *correlation area*, associated with the coherent fluctuations and thus acting as a discrete, coherent noise source. Identification of the correlation areas is important since their size and shape is related to the efficiency noise generation and radiation. The following abbreviated form for Equation (2.18) will be used to derive a frequency-dependent equation for the correlation area, where the time record index *k* has been omitted for brevity:

$$\begin{aligned} P(f) &= \left(\frac{\cos\theta}{4\pi x c} \right) \int_S j\omega e^{-j\omega r/c} \; P_s(f)\, dS \\ &= \int_S A_{\omega r} \; P_s(f)\, dS \end{aligned} \tag{2.32}$$

and the following substitution variables were used:

$$\begin{aligned} A &= \left(\frac{\cos\theta}{4\pi x c} \right) \\ A_{\omega r} &= \left(\frac{\cos\theta}{4\pi x c} \right) j\omega \, e^{-j\omega r/c} . \end{aligned} \tag{2.33}$$

The effects of retarded time, $e^{-j\omega r/c}$, and time differentiation, $j\omega$, have been incorporated into the variable A and denoted $A_{\omega r}$. Since $A_{\omega r}$ contains the retarded time effects in the phase term $e^{-j\omega r/c}$, and since the retarded time is a function of source-to-receiver distance, where the source is taken as each differential surface area, then $A_{\omega r}$ must be included in the integration over the surface S.

An alternate expression to Equation (2.19) for the mean square pressure spectrum may be obtained by multiplying Equation (2.32) by the conjugate of itself at a different set of surface locations $\vec{y}'$:

$$P^*(f,\vec{x})\,P(f,\vec{x}) = \int_S \int_{S'} A_{\omega r}\, P_s(f,\vec{y})\, A^*_{\omega r'}\, P^*_s(f,\vec{y}')\; dS(\vec{y}')dS(\vec{y}) \qquad (2.34)$$

where $A_{\omega r'} = \left(\frac{\cos\theta}{4\pi x c} \right) j\omega\; e^{-j\omega r'/c}$, and $r' = \left| \vec{x} - \vec{y}' \right|$. The *differences* in retarded time over the entire integration surface are manifested in the phase differences between $A_{\omega r}$ and $A_{\omega r'}$.

The *inner* integral of Equation (2.34) may be cast in terms of a *correlation area* S_c,

$$A_{\omega r} P_s(f,\vec{y}) \int_S A^*_{\omega r'}\; P^*_s(f,\vec{y}')\; dS(\vec{y}') \equiv P^*_s(f,\vec{y}) P_s(f,\vec{y})\; |A_{\omega r}|^2\; S_c(f,\vec{y}) \qquad (2.35)$$

where terms involving the integration variable $\vec{y}$ of the outer integral of Equation (2.34) have been taken outside of the integral over $\vec{y}'$ in Equation (2.35) to emphasize their independence. In this definition the retarded time *differences* have been neglected over the correlation area **only**. This point will be clarified momentarily. The definition of correlation area, given by Equation (2.35), may be rearranged to obtain the following form for S_c :

$$
\begin{aligned}
S_c &= \frac{\int_S P^*(\vec{y}\,')P_s(\vec{y})\ e^{-j\omega(r-r')/c}\ dS(\vec{y}\,')}{P_s(\vec{y})P_s^*(\vec{y})} \\
&\rightarrow \frac{\int_S G_{p'_s p_s}\ e^{-j\omega(r-r')/c}\ dS(\vec{y}\,')}{G_{p_s p_s}}
\end{aligned}
\tag{2.36}
$$

where the right arrow → in Equation (2.36) indicates the transformation into spectral density functions via the expectation operator and limiting process described earlier in Section 2.2.1, "Dipole Source Strength — dGpp/dS." (Recall that the finite transform index k was dropped for notational brevity.) Equation (2.36) provides a good conceptual picture of the correlation area. For each fixed point $\vec{y}$, the correlation area is determined by the integral of the cross spectrum between the surface pressure at the fixed point $\vec{y}$ and all other points on the surface with the phase adjusted to compensate for the retarded time differences between the different points on the surface. This integral is normalized by the autospectrum of the surface pressure taken at $\vec{y}$. The normalized cross spectrum is the transfer function:

$$
\begin{aligned}
S_c &= \int_S H_{p_s p'_s}\ e^{-j\omega(r-r')/c}\ dS(\vec{y}\,') \\
&\cong \int_S H_{p_s p'_s}\ dS(\vec{y}\,') .
\end{aligned}
\tag{2.37}
$$

Assuming a statistical decay in the two-point correlation with separation distance $\xi = r - r'$, then for large ξ the cross spectrum is small and the phase correction term $e^{-j\omega\xi/c}$ is unimportant. For small values of ξ, the phase correction may be approximated as unity. Hence, the approximation Equation (2.37) was made by ignoring the retarded time *differences*, only, just over the correlation area, and assuming spatial decay of the coherence between surface pressures separated by a distance ξ. These assumptions allow the approximation $A_{\omega r'} \cong A_{\omega r}$ which was used in Equation (2.35).

The difficulty with implementing Equation (2.37) is the requirement for the determination of two-point transfer functions over the entire blade surface; that is, the result of the double integral. Since the radiated acoustic pressure at a point in space is a superposition of pressures radiating from all regions of the blade surface, the effects of this integration can be incorporated into the equation for S_c to obtain a more practical expression for the correlation area.

The mean square acoustic pressure was expressed as an integral of the cross spectrum between the surface pressure and the acoustic pressure in Equation (2.19). Combining Equation (2.34) and Equation (2.36), and comparing with Equation (2.19) gives an expression for the correlation area:

$$S_c(f,\vec{y}) = \frac{A_{\omega r}\ G_{pp_s}}{|A_{\omega r}|^2\ G_{p_s p_s}} \tag{2.38}$$

where $A_{\omega r}$ is given in Equation (2.33). The real part of Equation (2.38) can be expressed as

$$\mathbf{Re}[S_c] = -\frac{4\pi x c}{\omega \cos\theta}\ \mathbf{Im}\left[e^{-j\omega r/c}\ \frac{G_{pp_s}}{G_{p_s p_s}}\right]. \tag{2.39}$$

The obvious advantage to this representation of the correlation area over that presented in Equation (2.36) is that S_c is determined by a single cross-spectral measurement; one point on the surface, and one point in the acoustic far field.

The time-domain representation of the correlation area was first presented by Sharland [86] who failed to realize the benefit of incorporating the correlation between the surface pressure and the far field acoustic pressure into the correlation area. Thus Sharland's expression for S_c was similar to Equation (2.35) above, but cast in the time domain (i.e., S_c was based on the cross-correlation and the autocorrelation functions). In 1973 Siddon [88] published a more rigorous derivation for the correlation area, still using time-domain auto- and cross-correlations functions, but was able to incorporate the cross correlation between the surface and acoustic pressures into the expression (see Equation [13] in Siddon [88]). The exclusion of frequency-dependent information in Siddon's expression for the correlation area made the experimental results difficult to interpret since the behavior of S_c was controlled by the dominant frequency components. The work presented here is an extension of Siddon's time-domain derivation into the frequency domain.

2.2.4 Interpretation of dGpp/dS and Sc

The mean square acoustic pressure at a point in space is denoted by G_{pp}, where frequency- and space-dependence are assumed. G_{pp} is comprised of contributions from source regions over the entire surface of a quasi-plane surface immersed in flow, hence the differential contribution to G_{pp}, dG_{pp}/dS, is a function of surface position $\vec{y}$. dG_{pp}/dS is referred to as the *dipole source strength per unit area.* If we consider the case where the source strength is uniform over the entire radiating surface, then the form of the dipole source strength per unit area is readily seen. For a uniform source strength distribution over S, $dG_{pp}/dS = K$ and

$$G_{pp} = \int_S \left(\frac{dG_{pp}}{dS} \right) dS(\vec{y}) = K \cdot \int_S dS = K \cdot S_a \qquad (2.40)$$

where S_a if the surface area of the immersed body.

An alternate form for G_{pp} is obtained by combining Equation (2.34) and Equation (2.36),

$$G_{pp} = |A_{\omega r}|^2 \int_S G_{p_s p_s}(\vec{y}) \; S_c(\vec{y}) \; dS(\vec{y}) , \qquad (2.41)$$

where the spectral-density form of Equation (2.36) for the correlation area has been used. Equation (2.41) demonstrates a fundamental feature of the correlation area; **$S_c(\vec{y})$ is a direct measure of the local surface pressure interactions and cancellations.** The correlation area contains space- and frequency-dependent information regarding the efficiency of radiation from the various regions of the radiating surface. For regions of high cancellation (local multipole distribution), S_c is quite small and there is no reinforcement of the local pressure from neighboring eddies. For large values of S_c the local eddies are well correlated over a large area and hence increase the strength of the local dipole sources.

The term *correlation area* is somewhat of a misnomer since S_c, as defined in Equation (2.35), is a complex quantity and, as discussed above, is related to the efficiency of radiation. It will be shown momentarily that the maximum value for S_c is the surface area of the immersed body, S_a. With this information, the correlation area could be normalized to the surface area of the radiating body to form a *normalized correlation area*, or correlation radiation efficiency factor σ_c which is bounded by ± 1,

$$\sigma_c = S_c / S_a \,. \tag{2.42}$$

The term *correlation area* will continue to be used throughout this thesis, primarily to maintain a historical link with previously published literature. However, it is noted here, and this point will be re-visited, that the correlation area is a *complex* quantity, and the *real* part, which corresponds to the radiation of real acoustic energy, can be negative. Values of S_c less than zero correspond to regions on the immersed body which destructively interfere with surrounding areas so as to create a net effect of absorbing energy — *an acoustical sink!*

The effects of the correlation area on the radiated pressure field are best demonstrated by examining three cases: 1) coherent sources over the entire radiating surface, 2) partially coherent sources where the correlation decays as a function of separation distance, and 3) total statistical independence between any two points on the surface S_a. In all cases it will be assumed that the local strength of the surface pressure is independent of $\vec{y}$ (i.e., $G_{p_s p_s}(\vec{y}) = K$ where K is constant). Thus the acoustic pressure is proportional to the the surface integral of the correlation area (see Equation (2.41)). Also, for the sake of discussion, the effects of the retarded time differences over the correlation area are neglected (i.e., $e^{-j\omega(r-r')/c} = 1$, where the prime is used to indicate the integration over the correlation area only).

Total Coherence. Since the mean square surface pressure is uniform over the surface, the only factor affecting two-point correlation is the relative phase relationship between the two pressures. Total coherence here means a unity coherence function between two points or that the cross spectrum is independent of surface location or separation distance; that is, $G_{p'_s p_s}(\vec{y}, \vec{y}') = G_{p_s p_s}(\vec{y})$ for all values of $\xi = |\vec{y} - \vec{y}'|$ and $\vec{y}$. Thus, from Equation (2.36) the correlation area $S_c = \int_S dS(\vec{y}) = S_a$, and the radiated pressure is

$$G_{pp} = |\mathrm{A}_{\omega r}|^2 \ \mathrm{K} \int_S S_a \ dS(\vec{y}) = |\mathrm{A}_{\omega r}|^2 \ \mathrm{K} \ S_a^2 . \tag{2.43}$$

Partial Coherence. For this case the cross spectrum decays with separation distance ξ about each point on the surface. Assuming a monotonic decay of the magnitude of the transfer function between two surface points, a separation distance or *correlation radius* ξ_c exists such that $\xi_c = \sqrt{S_c/\pi}$, and ξ_c is less than the characteristic dimension of the surface, $\sqrt{S_a}$. For simplicity assume the correlation area S_c is uniform over the surface. Then, the acoustic pressure is given by:

$$G_{pp} = |\mathrm{A}_{\omega r}|^2 \ \mathrm{K} \int_S S_c \ dS(\vec{y}) = |\mathrm{A}_{\omega r}|^2 \ \mathrm{K} \ S_a S_c . \tag{2.44}$$

Statistically Independent. Two-point independence implies the transfer function is unity at $\xi = 0$, but zero every where else. This case is treated by taking the limit of the *partial coherence* case as $\xi_c \rightarrow 0$, implying $S_c \rightarrow 0$ and there is no radiation. This case is of course not physically realizable as the even random molecular motion implies some infinitesimal correlation area.

Recall that the variable $\mathrm{A}_{\omega r}$ contains the frequency dependence due to the time derivative of the surface pressure, the (dipole) cosine directivity, and the spherical divergence:

$$|A_{\omega r}|^2 = \frac{\omega^2 \cos^2\theta}{16\pi^2 x^2 c^2} \tag{2.45}$$

2.2.5 Multiple Input/Output Analysis

A model for the problem may be developed by treating the distributed source region over the solid surface immersed in flow as a collection of discrete source regions, and the resultant acoustic pressure as the output of a multiple input/output model. Thus the integrals may be approximated by summations, the accuracy of which depends the character of the sources (source strength uniformity) and the selection of the differential area, ΔS. Since the multiple input/output model closely resembles the measurement procedures used here (i.e., discrete samples over a blade surface), a discussion is presented here regarding possible sources of errors and optimal ways to implement the formulas just developed for the correlation area and dipole source strength per unit area.

In general, the output of a multiple input system, G_{yy}, is given in terms of the cross spectra between inputs G_{ij}

$$G_{yy} = \sum_{i=1}^{q} \sum_{j=1}^{q} H_i^* G_{ij} H_j + G_{nn} \tag{2.46}$$

or in terms of the cross spectra between each input and the output G_{iy}

$$G_{yy} = \sum_{i=1}^{q} H_i^* G_{iy} + G_{ny} \tag{2.47}$$

where the cross spectra G_{iy} are given (for $G_{in} = 0$) by,

$$G_{iy} = \sum_{j=1}^{q} H_j G_{ij} . \qquad (2.48)$$

The noise terms, G_{nn}, G_{ny}, and G_{in} represent the extraneous noise in the model resulting from the optimal least squares estimate of the system transfer functions [13].

This set of equations represents a multiple input/output model where the unknown quantities, the transfer functions or frequency response functions H_i, represent linear systems based on the measured cross spectra. These linear frequency response functions do not necessarily correspond to any physically realizable system, but rather are the result of the mathematical processes inherent in the above equations. The degree to which the H's correspond to the physical system depends on several factors such as the linearity of the physical system, measurement accuracy of the cross-spectral estimates, the relationship between the model and the physical system, and other factors.[5] A derivation of the above set of equations describing the multiple input/output problem may be found in Bendat and Piersoll [14]. The equivalent to the above equations for the turbulence model are as follows:

---

[5] For further discussions of multiple input output analysis see References [10-13, 15, 92].

$$\begin{aligned} G_{pp} &= \sum_{i=1}^{q} \mathrm{A}_{\omega r_i} \, (G_{pp_s})_i \, \Delta S_i + G_{np} \\ &= \sum_{i=1}^{q} H_i \, (G_{pp_s})_i + G_{np} \end{aligned} \tag{2.49}$$

$$\begin{aligned} G_{pp} &= \sum_{i=1}^{q} \sum_{j=1}^{q} \mathrm{A}_{\omega r_i} \mathrm{A}^{*}_{\omega r_j} \, (G_{p_s p_s})_{ij} \, \Delta S_i \, \Delta S_j \\ &= \sum_{i=1}^{q} \sum_{j=1}^{q} H_i \, H_j^{*} \, (G_{p_s p_s})_{ij} \end{aligned} \tag{2.50}$$

where the equivalent system transfer function is

$$H_i = \mathrm{A}_{\omega r_i} \, \Delta S_i \tag{2.51}$$

and the acoustic pressure-surface pressure cross spectrum $(G_{pp_s})_i$ can be expressed as the sum of two-point surface cross spectra $(G_{p_s p_s})_{ij}$ as in Equation (2.48). These equations will be used to illustrate several practical aspects regarding estimates of the dipole source strength dG_{pp}/dS and correlation area S_c.

In lumped-element terms, the dipole source strength is denoted $(\Delta G_{pp}/\Delta S)_i$ where the incremental strength is evaluated at the i-th location on the surface. The units are of course the same as for the continuous form — Pa^2/m^2. As discussed earlier, the source strength represents the relative magnitude of the dipole-related sources as a function of frequency and spatial location on the surface. For a given turbulent structure, the multiple input/output model is defined by the distribution of measurement points on the surface, where the measured quantities are the various cross spectra between q source locations and the output (far field acoustic pressure). A uniform sampling grid is assumed here (for simplicity) thus the area associated with each measurement location is $\Delta S_i = S_a/q$ where the total surface area is denoted S_a. An estimate of the cumulative acoustic pressure (output) is given by,

$$G_{pp} = \sum_{i=1}^{q} \left(\frac{\Delta G_{pp}}{\Delta S} \right)_i \times \frac{S_a}{q} \ . \tag{2.52}$$

It is clear from Equation (2.52) that **the dipole source strength per unit area $(\Delta G_{pp}/\Delta S)_i$ is independent of the number of samples taken over the surface.** This fact allows the source strength to be determined (at a point) from the measurement of the cross spectrum at a single point on the surface.

A reasonable model for the eddy structure over the surface is to treat the distributed sources as discrete regions within which the eddies are, to some degree, self-coherent. The pressure fluctuations related to the turbulence outside of a particular region are assumed to be uncorrelated with those within the region Given a relatively sparse sampling grid (or rapid spatial fluctuations of the source distribution), the errors associated with estimating G_{pp} are large due to the fundamental notion that the i-th input in the model represents the differential area ΔS_i on which that point is centered. For a given measurement distribution, the errors in estimating the output from the given inputs are contained in the noise term of Equation (2.49), G_{np}. The differences between the true, nonuniform source distribution within ΔS_i and a uniform distribution based on the point measurement at location i are contained in G_{np}. In addition, the effects of partial (as opposed to full) correlation of pressures within ΔS_l are also included in G_{np}. Again, the spatial sampling errors affect the accuracy of the prediction of the total radiated pressure (a finer grid structure or more uniform source distribution yields a more accurate prediction), but not the estimate of the local dipole source strength.

The mutual correlation among inputs to the model is determined by the relationship between the sampling density and the correlation area. If all samples are taken at locations on the surface which are outside of the correlation areas centered on each point, then the inputs of the multiple input system are uncorrelated with each other and the governing equations are simplified. In this case the inputs may be treated independently and the output is determined by the sum of autospectral densities multiplied by the system transfer functions.

$$G_{pp} = \sum_{i=1}^{q} |H_i|^2 \; (G_{p_s p_s})_{i,i} + G_{np} \,. \tag{2.53}$$

This expression cannot be used to obtain a simplified estimator for the dipole source strength distribution. While the notion of using the autospectral density as an estimate of the dipole source strength is tempting, the penalty for such a simplification is an increased error term G_{pn} which becomes an inseparable part of the estimate of G_{pp} (i.e., $G_{pp} \sim G_{pp} - G_{np}$ is a *poor* approximation for sparse spatial sampling).[6]

---

[6] The best estimator for the source strength is given by the measurement of the cross spectrum between the surface pressure and the far field acoustic pressure (see for example Equation [2.20]). In effect, this is the same as performing a surface integral of the cross spectrum between two surface pressures as in the inner integral of Equation (2.34) since that information

If two points i,j are sampled within a correlation area then inputs i and j are partially correlated. In this case the cross spectrum between an input and the output contains, in addition to the autospectral density terms of Equation (2.53), terms involving the cross spectrum between inputs. These cross-spectral terms are associated with interference between surface pressure regions (see Equation [2.48]). Inclusion of these terms provides a more accurate estimate of the source strength than using just the autospectrum of the surface pressure, however, a better estimate yet of the cross spectrum is by direct measurement.

In summary, a lumped-element multiple input/output model has been applied to the distributed aerodynamic sources due to turbulence interactions with solid surface immersed in a flow field. Consequences of finite spatial sampling have been discussed. In general, the multiple input/output system is represented by the set of equations

$$G_{pp} = \sum_{i=1}^{q} H_i \ (G_{pp_s})_i + G_{np} \tag{2.54}$$

where the cross spectrum may be viewed in terms of the cross spectrum between two surface pressures,

$$(G_{pp_s})_i = \sum_{j=1}^{q} H_j^* \ (G_{p_s p_s})_{ji} \tag{2.55}$$

---

is contained in the acoustic pressure. The errors associated with the finite spatial resolution of the sampling grid are thereby eliminated.

There are three ways for estimating the cross spectrum of Equation (2.55) at each location *i*, listed here in order of increasing accuracy:

Estimate of Equation (2.55) — Surface Autospectrum at Point *i*. This estimator is the worst of the three because it contains both types of errors — those due to the finite spatial sampling inherent in the use of Equation (2.55) and the effects of neglecting mutual source interference. This estimator is however relatively simple to obtain since only the surface pressure autospectra are involved. The approximation to the mean square acoustic pressure using this estimator is given by,

$$G_{pp} \sim \sum_{i=1}^{q} |H_i|^2 \ (G_{p_s p_s})_{i,i} + G_{np} \, . \tag{2.56}$$

Equation (2.55) — Surface Cross Spectrum. In theory, the implementation of Equation (2.55) requires the measurement of all combinations of cross spectra between each surface pressure location. In practice, the number of cross spectra required depends on the relationship between the correlation area and the measurement grid. For correlation areas which are relatively small, only a few inputs near each location *i* will be important. The rest of the cross terms will be small relative to the autospectrum at *i*. While this estimator still contains the effects of finite spatial sampling, it does have the advantage of not requiring the measurement of the cross spectrum between the radiated acoustic pressure and the surface pressure, which can be a difficult quantity to measure due to the inherently poor coherence. Also, use of this method allows the prediction of the radiated noise from the surface *in situ* — that is, without the need for an acoustical environment for measuring the radiated acoustic pressure free of background noise or reflections from nearby surfaces. The approximation to the mean square acoustic pressure using this estimator is given by,

$$G_{pp} \sim \sum_{i=1}^{q} \sum_{j=1}^{q} H_i H_j^* \, (G_{p_s p_s})_{ij} + G_{np} \, . \tag{2.57}$$

Direct Measurement. If an environment is available in which the radiated acoustic pressure can be measured, then a direct measurement of the cross spectrum can be obtained. Measurement of the cross spectrum has the effect of performing a continuous integral (over the surface) of the cross spectra between the surface pressures, since that information is contained in the radiated acoustic pressure. The approximation to the mean square acoustic pressure using this estimator is given by Equation (2.54). This method overcomes the problems associated with finite spatial resolution of the sampling grid and includes the effects of partially correlated source regions. This is the preferred method for estimating the cross spectrum.

In addition to the use of Equation (2.54) for predicting the radiated pressure, the model may also be formulated in terms of the correlation area, S_c,

$$G_{pp} = \sum_{i=1}^{q} |H_i|^2 \, (G_{p_s p_s})_{ii} \left(\frac{S_c}{\Delta S} \right)_i \, . \tag{2.58}$$

Since the correlation area and the dipole source strength are both based on the cross spectrum between the acoustic pressure and the surface pressure, they are both subject to the same types of errors and limitations discussed above. Therefore, the optimal estimates for these quantities may be obtained from a direct measurement of the cross spectrum G_{pps_i}.

Another approach to the solution of the multiple input/output problem was developed by Bendat in 1976 [10, 11] which is referred to here as *partial coherent output power* analysis or PCOP. This process involves the computation of *conditioned* spectra which represent the cross-spectral density functions between an input and the output where the linear effects of other inputs have been removed. The mathematical procedure allows a new model to be developed based on conditioned inputs which are mutually uncorrelated by virtue of the conditioning process. An important parameter for establishing the conditioned model is the causality relationship between the inputs (i.e., whether input *i* is causing effects in input *j*, or vice versa). Interpretation of the conditioned inputs is difficult, at best. The analysis is dependent on *a priori* knowledge of the causality nature of the inputs in the original model, which is often the original objective the investigator. Without that knowledge the results can be misleading or even erroneous. **For the case of turbulence interactions over a plane surface, PCOP analysis is not applicable.** The reason is that PCOP analysis is an attempt to estimate the strength of individual inputs **with all other inputs powered off**. That is, the conditioning process is intended to isolate the unique properties of each input and estimate their relative contribution to the total output. By conditioning inputs, the effects of mutual source interactions are removed from inputs ranked by the investigator to be of lower order in terms of cause and effect, and attributed to inputs of higher order. For a turbulence model based on samples taken at various locations over the solid surface immersed in flow, the partially correlated regions represent a coherent eddy structure and local pressure interactions. A cause-effect relationship between the source regions is **not** applicable since the sources are interacting and collectively form a distributed complex source region. In most cases of turbulence generated noise, it makes no sense to associate a specific area within a correlation region with the *cause* and another area within the same correlation region with the *effect* — the correlation region is a distributed, interacting source region and should not be thought of as an accumulation of discrete stimulus and response areas.

2.2.6 Summary — dGpp/dS, dI/dS, Sc

The expressions that were developed in the previous sections are collected here in the forms used for the experimental work presented in Section 6.2, "Experimental Investigations Using Frequency Domain Theory." Note that the **real** part of each of the three components (mean square pressure, intensity, and correlation area) is given.

Dipole Source Strength per Unit Area — Mean Square Pressure

$$\frac{dG_{pp}}{dS} = -\frac{\omega \cos\theta}{4\pi x c} \, \mathbf{Im}\left[\hat{G}_{pps}\right]. \tag{2.59}$$

Dipole Source Strength per Unit Area — Acoustic Intensity

$$\frac{dI_k}{dS} = \frac{\cos\theta}{8\pi x c \rho \Delta h} \left[\hat{C}_{p_s p_1} - \hat{C}_{p_s p_2}\right]. \tag{2.60}$$

Correlation Area

$$S_c = - \frac{4\pi x c}{\omega \cos \theta} \ \mathbf{Im}\left[\frac{\hat{G}_{pp_s}}{G_{p_s p_s}} \right]. \tag{2.61}$$

The hat indicates a retarded time correction $e^{-j\omega r/c}$.

A form similar to Equation (2.59) was previously derived by Siddon [87, 88] based on the Fourier transform of the slope of the cross correlation function. Time-domain equivalent expressions for Equation (2.59) and Equation (2.61) were developed by Siddon as well with a slightly different form of Equation (2.61) first published by Sharland [86]. Auto- and cross-correlation functions were used by earlier researchers (see, for example, investigations by Clark and Ribner [20], Lee [50], Lee and Ribner [51], Leggat and Siddon [52], Miller et al [60], Richarz [80], and Siddon [88]). The frequency-domain expression of the correlation area, Equation (2.61), and the derivation of the equation for the acoustic intensity, Equation (2.60), are new to this work.

Chapter 3. Overview of Hardware Design and Test Facilities

This study involved the design and construction of a specialized centrifugal blower assembly and incorporated a wide variety of experimental data including the measurement of aerodynamic parameters such as mean flow velocity vectors, turbulence intensity levels and overall fan performance. Far-field acoustical data was acquired (sound power, pressure and intensity) as well as near-field and blade surface data. This section will describe the centrifugal blower design, the various experimental setups used, and some of the data acquisition techniques employed.

3.1 Scale Model Blower Blower Design and Mounting Configuration

This section includes a brief discussion of the fan laws and the scaling laws used in the design of the model blower. The blower was designed as a member of a family of blowers which are in widespread use for cooling computer and business equipment. The term *family* implies an homologous series of air moving devices covering a wide range of pressure and flow conditions where the performance of each device is predictable from any other device in the family using the fan law relationships described in [44].

3.1.1 Fan Laws and Sound Laws

It is often instructive to cast relational parameters in dimensionless form. The specific quantity used to nondimensionalize a parameter depends on the desired form of the relationship between the independent variables. In general, the total number of independent dimensionless parameters required for a specific problem is obtained by subtracting the number of dimensions involved from the number of dimensional quantities in the system. This is known as the Buckingham Pi theorem [18] and has formed the foundation for nondimensionalization of a broad range of problems.

In nondimensionalizing fluid flow problems involving small, low-speed air moving devices, the two most important parameters are the flow and pressure coefficients given by:

$$\phi = \frac{4Q}{\pi^2 N D^3} = \frac{4Q}{\pi D^2 U} \tag{3.1}$$

$$\psi = \frac{2P}{\rho(\pi D N)^2} = \frac{2P}{\rho U^2} \tag{3.2}$$

The flow coefficient, ϕ, is obtained by normalizing the flow rate, Q, to the effective flow rate calculated from the tip speed, N, and the circular area based on the tip diameter, D. The pressure coefficient (total, static, or velocity), ψ, is the pressure normalized by the effective tip velocity pressure, $(\rho U^2)/2$, where the tip speed $U = \pi D N$.

The overall air performance of a particular air moving device is generally characterized by the amount of static pressure developed for a given flow rate. This P *versus* Q relationship is referred to as a *head-flow curve*. When a blower is attached to some passive device for cooling, a *point of operation* is reached which corresponds to an equilibrium between the pressure rise across the blower and the pressure drop through the passive device. Since the flow rate through both devices is the same, this point is represented graphically as the intersection of the system resistance curve and the head-flow curve (see Figure 3). The *system resistance curve* relates the pressure drop across some passive device to the volumetric flow rate through the device. For turbulent flow this curve approximates a square law: $P = KQ^2$.

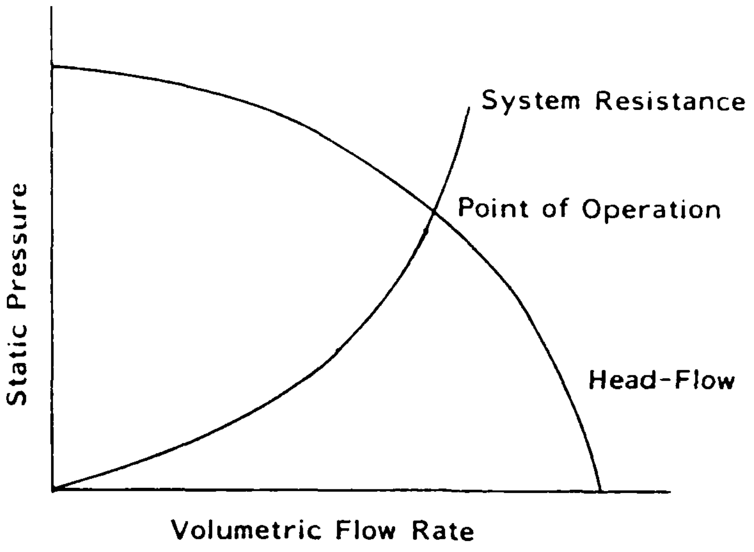

Figure 3. Air Moving Device Point of Operation

In nondimensional terms, the point of operation is referred to as the *point of rating*. Two similar fans are said to operate at the same point of rating if, on a dimensional head-flow curve, the proportions of pressure and flow capacities remain the same for both air moving devices. The dimensionless head-flow curves for any two air moving devices having similar flow conditions will be identical. This is a direct result of the fan laws which describe the relationships between the various flow parameters of the system. In order for these relationships to hold, there must be total similarity in the flow conditions; that is, geometric, kinematic, and dynamic similarity. Geometric similarity refers to dimensions (proportional magnitudes and equal angles), kinematic to fluid velocities, and dynamic to fluid forces. Total similarity as defined here ensures that the pressure and flow coefficients between two similar devices will remain constant. Considering other forces on the fluid such as compressibility, viscosity, gravity, and surface tension, none are important (within at least an order of magnitude) in terms of flow performance for the class of air moving devices of interest.

The sound laws for fans are relationships which allow the overall radiated noise level to be estimated from data on a single fan in a similar series of fans. The sound laws, first proposed by Madison [56], are based on the assumptions that, for a fixed point of rating, the sound intensity of the radiated noise is directly related to the mean square hydrodynamic pressure level inside the air moving device, and that the ratio of the hydrodynamic rms level to mean level remains constant throughout the series of air moving devices. Also, the sound power is related to the intensity through an area factor, thus the overall power radiated is proportional to the square of the characteristic linear dimension D. From the fan laws the flow rate Q is directly related to D^2 so the final sound power dependence is:

$$W = K_1 P^2 Q = K_2 D^7 N^5 \tag{3.3}$$

This is a fairly crude expression for noise dependence which contains no frequency-dependent information. The first attempt at developing a characteristic frequency spectrum for blower noise was by Maling [57]. While Maling was able to obtain a generalized spectrum, $g(s, \phi)$, he found that the flow coefficient (ϕ) and the normalized frequency parameter ($s = f/N$) were interrelated and thus g must be determined for each value of the flow coefficient ϕ.

3.1.2 Application of Scaling Laws to Model Blower Design

The initial objective of the project was to investigate the noise of a small centrifugal blower typical of those being used throughout the computer industry for cooling computer and business equipment. Space being of primary importance in the design of electronic equipment, most centrifugal blower impellers are of the order of 100 mm in diameter or smaller. Since most of the measurements were to be performed at or near the impeller blade surfaces, it was decided to design a scaled version of a typical device which was physically more accessible. The small blower that was chosen as the base design will henceforth be referred to as the *reference* air moving device, and the scaled blower which was designed and built specifically for this project will be referred to as the *model* air moving device.

A dimensional scale factor of 2 was selected as being a good compromise between accessibility and manageability. The model blower design was thus determined by scaling all of the linear dimensions of the reference device by 2.0 and by maintaining all of the appropriate blade angles. In addition, in order to maintain a constant tip speed Mach number the rotational speed of the blower was reduced by a factor of 2.0 from 3450 r/min to 1725 r/min. Since there were no commercially available impellers that matched the desired specifications, a custom impeller was fabricated by Revcor, Inc., Carpentersville, Illinois. A single-inlet configuration was chosen for the model over the reference double-inlet impeller. This was done to avoid any flow anomalies associated with disturbances due to the motor and other hardware obstructions that would have been near the inlet. As a result, the overall impeller width was the same as the reference impeller since only half of the impeller was modelled. Flow conditions inside the impeller were felt to be nearly identical since the reference impeller was constructed of two halves joined at the center along a solid septum.

The profile of the scroll volute was designed so that the clearance between the blade tips and the scroll increased linearly with angular displacement around the wheel.

The intent was to make the mean velocity or flow through the blades as uniform as possible by increasing the discharge cross-sectional area linearly with angle. If the scroll and blade row are "unwrapped," the angle between the line connecting the blade tips and the line of the scroll profile is called the *development angle*. A development angle of about 10° is a good compromise between blower performance and noise and is commonly used in the industry. The *cutoff angle* is the angle between two radial lines; the line from the axis of rotation to the top of the scroll and from the axis of rotation to the tongue or cutoff region. This is shown in Figure 4 on page 74.

The scroll profile for the model blower was chosen to maintain the same, nearly optimal, development angle as employed in the reference blower, but to increase the cutoff angle thereby minimizing the possibility of strong discrete tones due to the rotor-stator interactions at the scroll cutoff. The likelihood of strong, rotor-stator interactions in the model blower was increased by the fact that the model blower was a half-width, single-inlet design rather than a double-inlet impeller. The reference impeller design incorporated the blade passage tone reduction technique of circumferentially offsetting the two halves of the double-inlet wheel, which was not possible to implement on the single-inlet model impeller.

The scroll used for this work was manufactured by De-Sta-Co Division of Dover Corporation (Model 650) and had an optimal 10° development angle for a 161-mm diameter impeller. The cutoff angle for the scroll used here was 92°. This is considerably larger than the 64° cutoff which is accepted as being nearly optimal. The purpose of such a large cutoff was to eliminate the generation of discrete frequency tones (see later discussion).

The impeller was driven by a one-half horsepower, three-phase motor capable of operating at speeds between 0 and 1900 r/min, with a nominal rotational speed of 1780 r/min at 208 volts. For most of the experiments the motor was operated at a constant voltage of (208 volts) throughout the blower flow range which is a typical operating procedure (see Section 3.2.2, "Air Performance Determination," for discussion of speed variation at constant voltage.) A photograph of the model and reference blower components is shown in Figure 5 on page 75.

The blower assemblies were mounted to 570-mm square, 19-mm thick plywood plates which were attached to 609-mm square, 9.5-mm thick aluminum plates. The plates were designed to fit into the floor structure of the data processing raised floor installation installed in the IBM Poughkeepsie Acoustics Laboratory (see Section 3.3.1, "Acoustical Facilities," for details of the acoustical facilities). A schematic of the blower assembly is shown in Figure 6 on page 75.

A summary of the model blower specifications is provided in Table 1 and Table 2. The blade angles were deduced from information obtained from the manufacturer of the impeller. The computed dynamic specifications were calculated from the following assumptions:

- Computation of the average velocity at the inlet orifice was based on a uniform flow distribution across the inlet, an inlet opening diameter of 123.5 mm (DeStaCo inlet ring #603), and the blower operating at the design point (Best Efficiency Point or BEP) which is a flow rate of 0.141 m^3/s.

- The computation of the average air velocity at the exit of the blades was based on evenly distributed flow through the blade channels, the mean radius of the blades, and the BEP operating point.

Table 1. Model Blower Scroll Specifications

Scroll Specifications

Material: Steel (20 gauge)
Bellmouth Inlet Diameter: 123.5 mm
Discharge Area: 177.8 x 120.6 mm wide
Optimum Impeller Diameter: 161.3 mm
Development Angle: 10.8 degrees
Cutoff Angle: 92°

Table 2. Model Blower Impeller Specifications and Dynamic Characteristics

Impeller Specifications

Material: Aluminum
Number of Blades: 26
Blade Thickness: 1.0 mm
Mean Radius Blade Spacing: 17.63 mm
Arch Length: 17.46 mm
Radius of Forward Curvature: 11.11 mm
Chord Length: 16.26 mm
Inlet Blade Angle: 15°
Outlet Blade Angle: 66°
Blade Camber Angle: 91.2°
Blade/Impeller Width: 101.6 mm
Impeller Diameter (TE): 160.34 mm
Trailing Edge Radius: 80.17 mm
Leading Edge Radius: 60.11 mm
Mean Impeller Radius: 70.14 mm

Dynamic Characteristics

Tip Speed @ 1800 rpm: 15.07 m/s
Mach Number: 0.0438
Dynamic Head: 137.4 Pa (re: 15.07 m/s)
Average Velocity at Inlet: 9.09 m/s
Average Velocity at Exit: 2.87 m/s
Mach Number at Exit: 0.00834
Dynamic Head at Exit: 4.98 Pa (re: 2.87 m/s)

It is important to note the extremely small tip velocities relative to the speed of sound. For Mach number less than about 0.3 the flow through a compressor, from an aerodynamic viewpoint, can be considered incompressible. In acoustical terms the fluid can never be considered incompressible, otherwise there would be no noise generated and an infinite sound speed. In terms of aerodynamic and acoustic performance, using the frequency-independent sound laws expressed in Equation (3.3), the noise level generated by the model blower should be the same as the for the reference blower, for the same point of rating, keeping in mind the linear dependence of sound power on width. Also, the fan performance should be equivalent to two reference blowers operating in parallel. This is because the static pressure is directly related to the square of the tip speed, which was unchanged, and the two-fold increase in the characteristic dimension D caused a four-fold increase in flow, which was reduced to twice the flow since only a half-width configuration of the reference blower was modelled.

3.2 Task-Specific Test Setups

This section is devoted to a description of each of the measurement setups used for this study. In addition to a detailed description of the hardware and instrumentation, further details will be provided on the specific measurement methodology used and the manipulation of the first-generation data to obtain the desired quantities.

3.2.1 Aerodynamic Load Apparatus

Since the kinematic flow conditions for an air moving device are strongly dependent on the particular operating point of the device, it is important for the purposes of these studies to be able to control the point of operation of the blower without significantly affecting its aerodynamic or acoustic performance. One approach to this problem was first proposed by Maling [58], and has been in use in the IBM

Acoustics Laboratory since 1962, in which an aerodynamic load is applied to the air moving device under test by attaching the device to a large plenum with thin, non-porous, acoustically transparent walls. The operating point of the air moving device is controlled via an adjustable orifice located in the opposite corner of the plenum from the air mover. Use of a piezometer ring located inside the test plenum provides a means for monitoring the static pressure developed by the air moving device and thus enables the operating point to be set. The head-flow curve may be used to estimate the volumetric flow rate of the device for a given static pressure, or, a more elaborate facility might incorporate a means for determining the volumetric flow rate directly by monitoring the flow through the adjustable orifice.

The key to the success of the plenum has been that the walls can be made quite thin and still remain impervious to flow, thus providing minimal acoustical attenuation over a broad frequency range. The test plenum is generally used for overall sound power determination, thus the effect of the plenum on the directivity of the air moving device is not very important, especially if reverberant room methods are used for determining sound power.

In 1985 the Institute of Noise Control Engineering, Technical Committee on Computer and Business Equipment, issued a document which described in some detail the specifications for constructing a standardized test plenum, and measurement procedures governing the use of the plenum for measuring the noise emitted by air moving devices [30]. This document was published in the form of a "Recommended Practice" (henceforth referred to as *INCE RP 1-85*), and has since been submitted to an ANSI working group for conversion to an American National Standard. A European counterpart to INCE RP 1-85 which specifies a slightly different configuration for attaching the air moving device has also been submitted to the International Organization for Standardization, ISO, for conversion into an international standard.

A new test plenum was constructed during the summer of 1984 following the guidelines of INCE RP 1-85. The box frame was constructed of solid 50-mm square oak members and covered with a thin Mylar® cover (0.0381 mm nominal thickness). A schematic representation of the INCE test plenum is shown in Figure 7. The INCE plenum was used throughout the project to provide the subject blower with a desired aerodynamic load. For all tests on the model blower performed in the Acoustics Laboratory, the blower and plenum were installed in the reverberation room. The static pressure inside the test plenum was monitored using a digital manometer calibrated to read pressure head in mm of water.

3.2.2 Air Performance Determination

The air flow performance was measured with the blower assembly attached to an air flow test facility located in the IBM Poughkeepsie Thermal Laboratory and tested in accordance with standardized test procedures [3]. In addition to the static pressure and flow, the voltage, speed, and input electrical power were recorded. This information was needed to determine the design point of the blower (i.e., the best efficiency point or BEP). The BEP is defined as the point of maximum static efficiency, where static efficiency is the ratio of aerodynamic output power to electrical input power to the motor. Note that this is an approximation to the true air mover efficiency in which the input power is taken at the impeller shaft rather than at the motor.

For all tests, the blower was operated at a constant voltage (208 volts) throughout the flow range, which is a typical test procedure [3]. Depending on the torque curve of the motor, this may or may not cause the blower to operate at a constant rotational speed. In the present setup, the one-half horsepower, three-phase motor has sufficient power to overcome the additional lift and drag forces at maximum flow. The total variation in operating speed of the blower is from 1779 r/min at free delivery (i.e., 0 pascals static pressure) to 1792 r/min in the stall region for nearly totally blocked flow with a static pressure of 25 mm of water (250 pascals). The acoustical effect of this small variation can be estimated by assuming a fifth power dependence on speed, which says that the difference between operating at constant speed and constant voltage in this case is insignificant (0.16 dB).

3.2.3 Blade Channel Inlet/Outlet Velocity Determinations

In order to quantify the uniformity of mean flow through the blade channels, and to identify regions of excessive turbulence intensity near the blade surfaces, hot film anemometry was used to measure the velocity components at the inlet and exit of the blade channels. Anemometry was the method of choice because it is reasonably accurate, relatively easy to use, and is capable of measuring both the steady and fluctuating components of the velocity field.

Single- and dual-element hot film sensors were used to resolve the velocity vector at the leading and trailing edges of the blades into radial, $\vec{v}_r$, and tangential, $\vec{v}_\theta$, components.[7] Generally the radial velocity component is of interest since it is a measure of the volumetric flow rate through the blade channel. Other components are important for investigations involving the three dimensionality of the flow or for an estimate of the fluid angles relative to the blade geometry, however, inferences of the fluid angles can be made from knowledge of the radial component.

The general flow direction at various points in the air moving device inlet was obtained using flow visualization techniques (see Section 5.1, "Flow Visualization"). This information coupled with the cosine directivity characteristics of a hot film sensor allowed measurements to be made at the leading edges of the blades of the magnitude

---

[7] See Section A.1, "Velocity Diagrams," for discussion of the velocity field and the terminology used in the decomposition of the velocity vectors.

of the radial velocity component using a single-element sensor. For these measurements the sensor was placed close to the leading edge of the blade row and aligned with axis of rotation so as to minimize the sensitivity to the axial velocity component.

At the trailing or outside edges of the blades, it may be assumed that the meridional velocity component ($\vec{v}_m = \vec{v}_r + \vec{v}_x$) is completely radial; that is, the axial component $\vec{v}_x$ is negligible. This is not in general true at the leading edges. With this simplifying assumption, mean velocity and turbulence measurements were performed at the trailing edges using a single-element hot film sensor located in a fixed frame of reference (relative to the scroll) with the sensing element oriented one of two ways (relative to the axis of rotation), depending on the desired result:

Parallel — This orientation provides a measure of the vectorial sum of the radial and tangential velocity, and is assumed to approximate the *total* velocity since the axial component is small.

Perpendicular — This sensor orientation allows determination of the magnitude of the *radial* velocity vector, again assuming a small axial component.

The appropriate sensor orientations in the blower inlet were achieved by modifying a standard hot film sensor probe support by adding a right angle bend approximately 35 mm from the sensor end. This allowed placement of the cross-stream sensor, which *also incorporated a 90° orientation, at the blade leading edge without significant* upstream flow disturbance from the probe support. A photograph showing the sensor placed at the leading edge using the modified probe support is shown in Figure 9.

The leading- and trailing-edge radial velocities were measured at five spanwise positions spaced 20 mm apart, centered on the geometric center of the impeller. Five leading- and five trailing-edge measurements were taken at each of eight circumferential locations, equally spaced at 45° intervals around the impeller for a total of 80 spatial locations. A diagram of the measurement grid and the sensor orientations used is shown in Figure 10. Additional measurements of other velocity components and directions were made at selected locations around the impeller.

In all of the velocity measurements, it was necessary to sample the signal at the same time relative to the blade position for each revolution of the impeller. A schematic of the instrumentation setup to accomplish this is shown in Figure 11. Once per revolution of the impeller, a short pulse was generated by an infrared sensor attached to the mounting plate which sensed a white strip of paper affixed to the rotating shaft. The angular location of the paper on the shaft determined the location of the blades relative to the sensor at the instant of trigger. A time delay between this trigger signal and an instrumentation trigger used to initiate the acquisition of data was introduced through the use of the GenRad pulse delay generators. The functions of the generator were to provide control over the time delay between blade passage and instrumentation trigger, and to condition the infrared signal. These pulse delay generators act to sharpen the trigger since the width and height of the pulse from the infrared sensor depend to some extent on the shape of the paper on the shaft and the supply voltage used to drive the infrared emitter/sensor. The duration of the infrared pulse was about 2 milliseconds with a rise and decay of about 5 volts per ms. At a rotational speed of 1780 r/min and 26 blades, the blades pass at a rate of 1.3 ms per blade. The duration of the final trigger pulse should be a small fraction of the blade repetition rate to ensure stable instrumentation triggering. The pulse delay generator provided such a pulse from the infrared signal. An optical strobe was triggered by the same pulse used to initiate data acquisition (i.e., the delayed trigger). In this way, the time waveform from the hot film anemometer system was accurately synchronized with the passage of a blade channel by continuously adjusting the time delay to visually align the sensor with a specific blade edge. A sampling rate of 102.4 kHz was used which provided about 132 data samples between blade edges. This is the maximum sampling rate of the analyzer being used (HP5420A).

With accurate triggering, the mean velocity levels can be estimated using the time averaging capability of the analyzer. However, in order to estimate the turbulence levels at each point in space, statistics must be computed based on several sample time records (ensemble averaging). In general, the mean or rms velocity levels for a particular circumferential location are represented by a specific *data bin* in the resultant time record.

The velocity direction for a given blade position may be determined using either two different orientations of the single-element hot film sensor, as in Reference [78], or through the use of a two-element hot film sensor. In general, a three-element, cross-wire sensor may be used to determine the direction of the mean velocity vector if the signs of the orthogonal components are known. A two-element hot film sensor may be used with two-dimensional flow, again with knowledge of the two direction signs. Estimates were made of the discharge velocity at the trailing edge by assuming that the radial component was flowing outward away from the axis of rotation and the tangential component was in the direction of rotation. While these would appear to be reasonable assumptions, there were locations around the impeller where the flow did not appear to have any significant radial flow. For these conditions, where the mean flow is not necessarily associated with flow through the blade channels, the direction sign of the tangential component was less certain.

Two dual-element sensors were used. The TSI Model 1241 is a straight probe with the x-sensors oriented for end flow where the Model 1246 probe contains a 90 degree bend and is thus suited for cross flow applications. The direction of the mean velocity vector was computed from:

$$\theta = \tan^{-1} \left| \frac{(V_a - V_b)}{(V_a + V_b)} \right| \qquad (3.4)$$

where V_a, V_b are the mean velocities computed from the output of the two sensors, and the angle is relative to a line bisecting the right angle formed by the two sensors. The results of the hot film sensor measurements are presented in Section 5.2, "Blade Channel Inlet/Outlet Velocities."

3.2.4 Microphone Positioning System

As part of the effort to characterize the overall radiation characteristics of the blower, an investigation of the distribution of the active acoustic intensity near the inlet of the blower was performed. The objective of this portion of the research was to characterize the flow of acoustic energy from the inlet of the air moving device by mapping the acoustic intensity near the inlet as a function of spatial location and frequency.

In order to perform the space-domain measurements, a sampling device was constructed which allowed automated control of the position of a sensor retainer over an area of 1 square meter (1.03 m × 1.10 m) with a computed spatial resolution of 25 microns.[a] The *computed* resolution is based on the mechanical resolution of the stepper motors and ball bearing screw. The *actual* resolution must take into account mechanical fitting tolerances, friction, backlash, etc. This would most certainly be greater than 25 microns. The positioning system was primarily used to position acoustical sensors,

---

[a] The author gratefully acknowledges the work of Reinhart Beatty who was responsible for the mechanical design and construction of the positioning system. The author was responsible for the design layout of the system.

hence the term *Microphone Positioning System*, or MPS. The MPS ball bearing lead screws were driven by a commercially available two-axis stepper motor motion control system[7] interfaced to an IBM PC/XT using the IEEE-488 interface protocol. Position control software was written to sense limit switches mounted to the MPS to set an absolute origin when power is applied, and to perform relative and absolute moves. The MPS measurement plane may be oriented horizontally or vertically using detachable supports.

A schematic representation of the instrumentation used for measuring the intensity distribution is shown in Figure 12. The instrumentation system of Figure 12 may be used for mapping acoustic or aerodynamic quantities, scalar or vector (e.g., sound pressure, sound intensity, mean flow components, turbulence intensity, etc.). Most quantities of interest are functions of frequency as well as space, thus requiring the management of relatively large blocks of data. For example, a 10 × 20 point, two-dimensional intensity map consumes nearly 1 megabyte of disk space when stored in numerical format on a computer disk.

For the measurement of intensity maps each spatial vector was represented by two spectra—magnitude and direction of the intensity vector over a given frequency range. Since the analysis system was limited to measuring one intensity component at a time, two sweeps of the measurement grid were required to obtain a complete map of the two-dimensional intensity field, requiring a total of 9 hours for acquisition alone. For such an extended measurement time source stationarity becomes important. Periodic checks were made at reference locations in the sound field to ensure the long term stability of the source and acoustic environment. All intensity estimates were made

---

[7] The stepper motor system is available from Superior Electric, Bristol, CT as the MODULYNX® Motion Control system, and typically consists of the motors, driver electronics, and a computer interface

using a Bruel and Kjaer Type 3519 Sound Intensity Probe and a Hewlett Packard HP5420 FFT Analyzer The cross spectral method was used for estimating the sound intensity vector.

Two basic source configurations were measured using the system described above:

1. An axial fan (Muffin® XL Model MX2A1, EG&G Rotron, Woodstock, NY) was mounted in one of the reflecting plane floor panels of the hemi-anechoic chamber (see Section 3.3.1, "Acoustical Facilities," for description of the acoustical facilities) such that the outlet noise was isolated from the inlet sound field (i.e., outlet air discharged under the raised floor).

2. The model blower assembly was installed in the hemi-anechoic chamber with the mounting plate perpendicular to the raised floor and a section of the raised floor, directly under the blower, replaced with acoustically absorptive material. The blower was oriented such that the inlet was directed away from the reflecting plane and air was exiting in a plane parallel to the floor.

The three-bladed axial fan was operating at free delivery at a speed of 3100 r min thereby generating discrete frequency tones related to the blade passage frequency of 155 Hz. The measurement grid contained 200 points (10 × 20) spaced at intervals of 50 mm, centered 100 mm above the fan inlet. The intensity probe consisted of two 12.7-mm diameter microphones separated by a 50-mm spacer. The increased microphone spacing was used to improve the accuracy of the intensity estimates at the first few harmonics of the blade passage frequency of 155 Hz. A measurement bandwidth of 800 Hz was selected thus yielding nominal resolution bandwidth of 3.125 Hz.

Figure 13 is a schematic representation of the blower installation which shows the orientation and relative size of the measurement area located just above the blower mounting plate. For this set of data the measurements were made at spatial intervals of 30 mm for an overall grid size of 270 mm × 570 mm. The cross spectral estimates were made over a frequency bandwidth of 6.4 kHz providing a frequency resolution of 25 Hz. A smaller microphone separation distance of 12 mm was selected to extend the upper frequency range of the estimates.

3.2.5 Quiet Air Source

A series of experiments were performed using the frequency domain expressions developed in Section 2.2, "Frequency Domain Analysis," to estimate the dipole source strength of the noise generated on a single blade immersed in flow under various conditions. This section contains a brief description of the apparatus designed to produce a flow field suitable for such an analysis. Details and results of the experiments performed using this flow apparatus are described in Section 6.2, "Experimental Investigations Using Frequency Domain Theory."

The design goals for the air source were as follows:

Low Noise. The residual acoustic noise level of the air source should be sufficiently low so as to produce at least a 10 dB increase in radiated noise over a broad frequency range when a single blade is inserted. This is a key feature of the flow facility, hence the term *quiet air source*.

Variable Turbulence. There should be regions of very low turbulence and regions of high turbulence. The turbulence intensity should range from a minimum of 1 percent to a maximum level of 30 percent or higher. A wide range of turbulence levels was found in the inlet of the model blower, and these experiments should be performed under similar conditions.

Variable Mean Flow. The mean flow velocity should be variable from 5 m/s to 15 m/s (typical velocities in the model blower) at a particular point in space.

Minimal Acoustical Disturbance. All points in the flow field must be accessible and the entire flow apparatus should allow for unobstructed acoustic radiation from within the flow field.

In order to satisfy the above design goals, a jet flow facility was constructed producing a flow field in which two distinct regions existed: a central *core* region containing very low turbulence levels and a clearly defined direction of mean flow, and a *mixing* region with much higher turbulence levels and large scale eddies characteristic of a transition layer. The key elements to the quiet air source are depicted in the schematic shown in Figure 14. The air supply was provided by the second of two model blower assemblies constructed for this project. The blower was attached to an acoustically lined plenum which served as a settling chamber and transition to a 10 meter section of flexible acoustical duct. The blower, transition plenum, and acoustical duct were installed below the raised floor of the hemi-anechoic chamber to minimize the background noise level. The duct was attached to a large opening in a floor tile upon which was placed a 0.7-meter long section of rectangular, acoustically lined duct (Quiet-DUCT® Silencer Type L manufactured by Industrial Acoustics Company, Bronx, New York). The final component in the air path was a rectangular converging section attached to the end of the acoustical duct which provided a small rectangular orifice for the jet exit area. The converging section was 0.5 meter long with an inlet area of 390 mm × 300 mm and an exit area of 110 mm × 23 mm for an area contraction ratio of 46.

The exit air velocity was controlled by varying the speed of the model blower attached to the transition plenum. The maximum velocity attainable in the core region was 16 m/s. The aerodynamic and acoustic characteristics of the quiet air source will be given in Section 6.2.2, "Quiet Air Source Characterization." A photograph of the quiet air source installed in the hemi-anechoic chamber is shown in Figure 15.

3.3 General Laboratory Facilities

A brief description of the acoustical facilities and instrumentation used for this project is given in this section. For the most part commercially available instruments were used during the research, so signal processing details will not be provided unless a specialized approach was chosen for a task.

3.3.1 Acoustical Facilities

All of the experiments for the present study were performed at the IBM Acoustics Laboratory in Poughkeepsie, New York with the exception of the air performance data which required the use of an air flow test facility located in the IBM Poughkeepsie Thermal Laboratory. The three primary acoustical chambers at the Acoustics Laboratory are a reverberation room, a convertible, fully-anechoic chamber, and a hemi-anechoic chamber.

All chambers are single-wall construction with either poured concrete or filled concrete block. All floors are poured concrete on-grade construction with no floating suspension. The absorptive surfaces of both anechoic chambers are nominal 90-Hz wire-protected fiberglass wedges.

The reflective plane of the hemi-anechoic chamber is a *raised-floor* construction typical of that found in a data processing installation with 60-cm square floor panels, weighing approximately 14 kg each, supported by a structural grid. If required, a two-speed, low noise air system supplies fresh air into the space under the raised floor of the hemi-anechoic room. The air is then vented into the chamber through several perforated panels and exits the chamber via acoustically lined return air ducts. The perforated floor panels are interchangeable with solid panels and thus may be arranged to eliminate their influence on the measurements. Dimensions of the hemi-anechoic field (i.e., between wedge tips) are 7.3 × 10.6 × 3.9 m high.

The 230 cubic meter reverberation room is populated with acoustical absorbers arranged to reduce the effects of low modal density at frequencies below the statistical lower frequency limit of the chamber. The reverberation room has been qualified for use in measuring noise sources containing discrete frequency tones at or above the 100 Hz one-third octave band [94].

Background noise levels in the chambers are quite low, due in part to the favorable location of the Laboratory site relative to possible environmental noise sources. For most octave bands of interest, the minimum noise levels measured in the chambers are limited by the instrumentation and not the environmental noise. Background noise levels in the hemi-anechoic chamber increase by about 3.0 dB on an A-weighted basis with the air system operating on high speed and about 0.2 dB on low speed, relative to the air system powered off (which is of the order of 19 dB(A)).

3.3.2 Instrumentation

Some of the specific instrumentation setups were covered in Section 3.2, "Task-Specific Test Setups." This section contains a description of transducers and other specialized instrumentation used.

Various transducer types were employed, depending on the parameter to be measured. In general, sound field measurements utilized Bruel and Kjaer 12.7-mm or 6.35-mm diameter condenser microphones; flow field velocity measurements were performed using hot film anemometry from TSI, Inc.; and blade surface pressures were measured using either microphones fitted with probe tubes or miniature pressure sensors manufactured by Kulite Semiconductors.

For measurements made in the hemi-anechoic chamber, both 12.7-mm and 6.35-mm diameter, free field response microphones were used; Bruel and Kjaer Type 4165 and Type 4135, respectively. A 12.7-mm diameter pressure response microphone, Bruel and Kjaer Type 4166, was used for the reverberation room measurements.

The hot film anemometry system consisted of a three-channel anemometer (TSI Model 1054A) with integral linearizers, a sum and difference module (TSI Model 1063) for use with two-element sensors, and a variety of single- and two-element hot film sensors. The linearizers and sensors were calibrated by the manufacturer for mean flow using an end point calibration over the range of 0-30 m/s. The frequency response of the sensors was checked following procedures specified by the manufacturer. The internal oscillator produces a 1 kHz square wave in the Wheatstone bridge circuit and the half-power response of the sensor may be estimated from the time constant τ. The nominal measured bandwidth was 30 kHz or higher for all sensors used. Control resistors were utilized with the sensors to provide the proper operating resistance. End point calibration and stability were checked periodically during the experiments.

Blade surface pressure measurements were performed using either a 12.7-mm condenser microphone fitted with a probe tube (Bruel and Kjaer Type 4165 microphone and UA0040 Probe Kit), or a miniature pressure transducer manufactured by Kulite Semiconductor Products, Inc., Ridgefield, New Jersey (Model LQMIC-125-LT). The Kulite sensors are similar to those used in edge noise studies reported by Brooks and Hodgson [17]. They are piezoresistive type sensors incorporating a strain gage etched on a thin diaphragm. The nominal dimensions of the sensor are 0.76-mm thick, 4.4-mm wide, and 9.6-mm long. The circular sensing area has an overall diameter of approximately 3 mm. A battery was used for the power source to minimize noise. For an excitation voltage of 6 volts, the overall nominal sensitivity was 0.8 μV/Pa. Further details concerning calibration and frequency response of both the Kulites and the probe tube microphones are provided in Section 6.2.1, "Transducer Calibration."

Signal conditioning was often necessary. For this purpose most of the signal amplification and filtering was achieved using a two-channel signal conditioner (Ithaco Model 454 preamplifier and Model 4112 filter). The filter-amplifier sets were calibrated and verified to have minimal inter-channel gain and phase mismatch. The band pass filters were nominal fourth-order Butterworth.

Signal analysis was performed using a two-channel digital signal analyzer (Hewlett Packard HP5420 FFT Analyzer), a two-channel sound intensity analyzer (Bruel and Kjaer Type 3360), or a single-channel, one-third octave band real time analyzer (GenRad Model 1995). All FFT analysis was performed on the Hewlett Packard HP5420 FFT Analyzer. The selection of a *random* signal type implements a Hanning data window. A 3.2 kHz analysis bandwidth was used and signals were averaged over 256 or 512 ensembles. The cross spectral density estimates between the blade surface pressure and the acoustic field at a distance of 200 mm implies a propagation time delay of 580 μs. Since this time delay is a small portion of the total time record used by the analyzer for the 3.2 kHz bandwidth ($T = 80$ms), the resulting time delay bias error was assumed to be negligible. The Hewlett Packard HP5420 FFT Analyzer was also used to ensemble average the velocity records acquired using the synchronized triggering system. For these data, a total of 128 ensemble averages was used.

Some signal analysis was also performed using a digital oscilloscope with post-processing capabilities (Nicolet Instruments Model 4094 with software packages for waveform analysis, mathematics, and advanced acquisition). In particular, the steady and fluctuating velocity levels were obtained by sampling the hot film sensor output at a rate of 1K samples/second (K equals 1024) for 16 seconds, and computing the mean and rms levels from the stored data using the Nicolet software. The data were also stored on diskette for further analysis. The low sampling rate of 1K samples s was selected based on the maximum memory size of 16K samples per trace.

Frequently data were transferred to a computer for more extensive processing, in which case an IBM PC/XT was used to communicate to the attached instruments via the General Purpose Interface Bus (GPIB). The PC/XT was also used as a local controller for various instruments, allowing repetitive tasks to be programmed, or, occasionally acted to synchronize the acquiring of data among multiple instruments.

In cases where graphical output of the post-processed data was required, or more extensive processing of the data was required than was feasible for a rather limited PC microprocessor, the information was transferred from the PC environment to an IBM mainframe host computer. The host-PC interface was implemented using the IBM Personal Computer Graphics Attachment (IBM PCGA) emulation package. The PCGA package consists of terminal emulation hardware and software which reside in the PC and a graphics card which interfaces to the appropriate graphics display (in this case, a high resolution, monochrome graphics display, Tektronix Model 614).

After transferring the data to the host, graphical display was obtained using primarily two graphics packages; either GRAPHPAK, a VSAPL-based package containing graphics utilities to be used in a user-written APL program, or, GRAFSTAT, also VSAPL-based but menu-driven. Both graphics packages are also capable of creating device-independent graphics files which could be used for plotter output or for direct integration into the IBM Document Composition Facility.

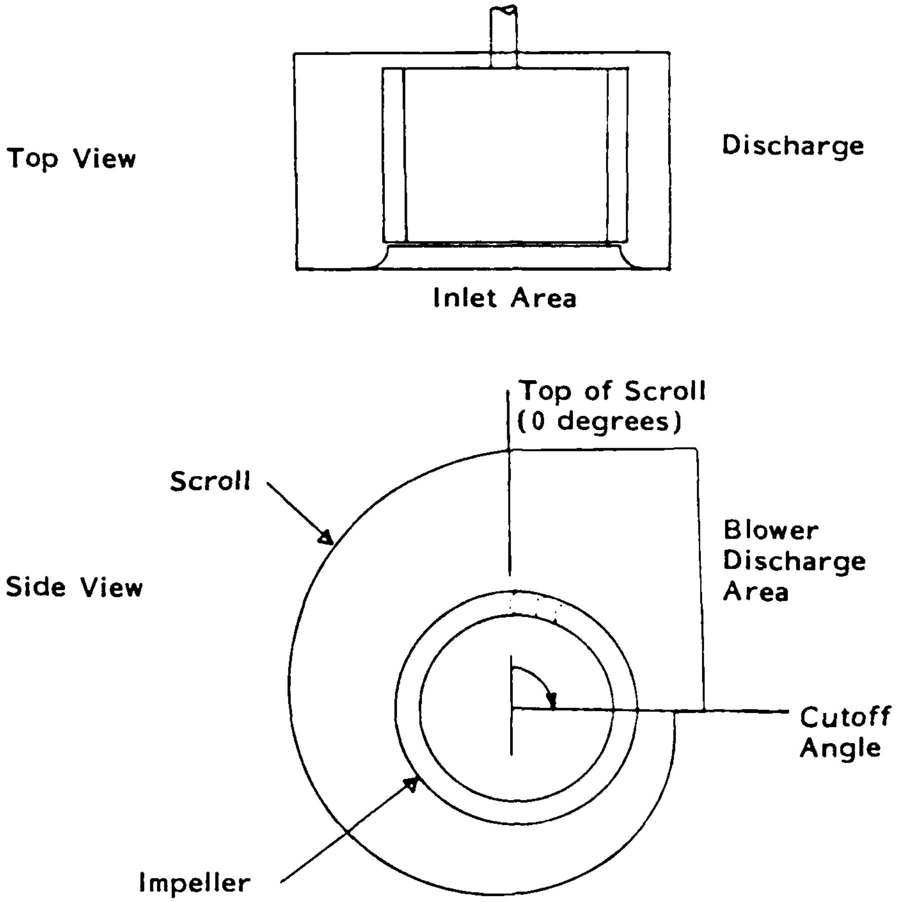

Figure 4. Centrifugal Blower Terminology. The cutoff angle is measured clockwise (as viewed from the inlet) from the top of the scroll to the scroll cutoff or tongue. A 92° cutoff angle was chosen for the model blower to minimize the strength of the rotor-stator interactions.

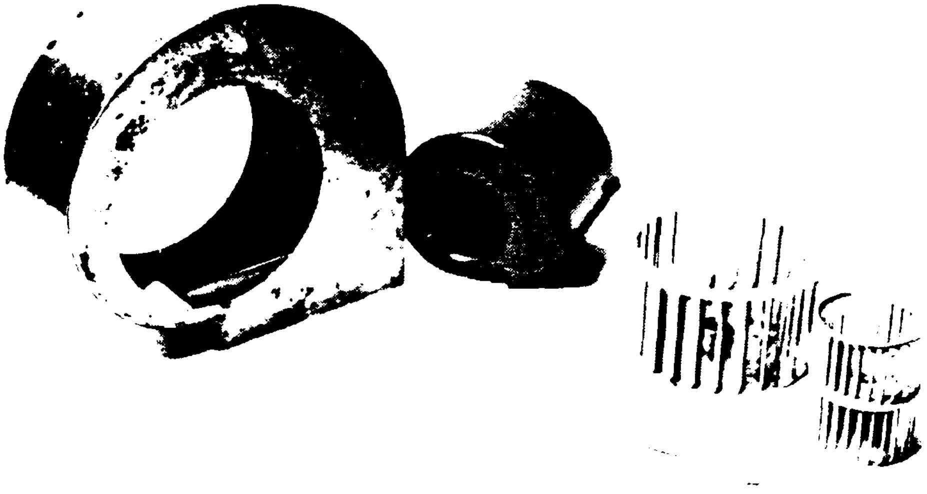

Figure 5. Photograph of Scroll and Impeller of Model and Prototype. The model blower scroll is shown without the inlet bellmouth adapter that is normally installed after the impeller is mounted to the motor shaft.

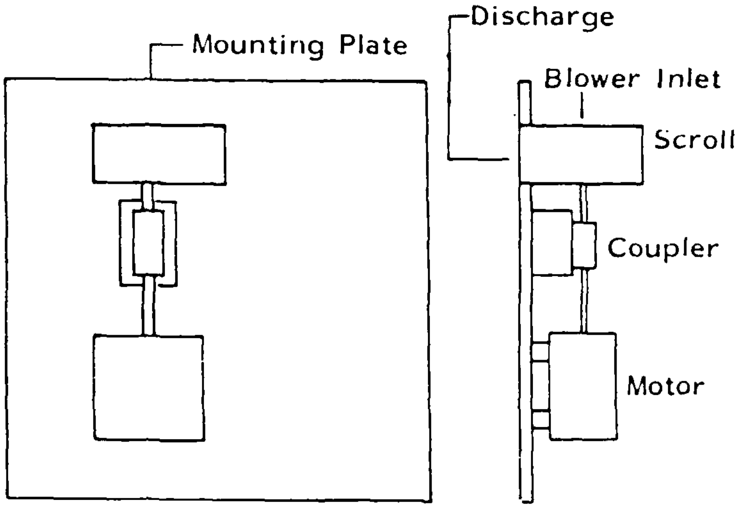

Figure 6. Blower Assembly Schematic

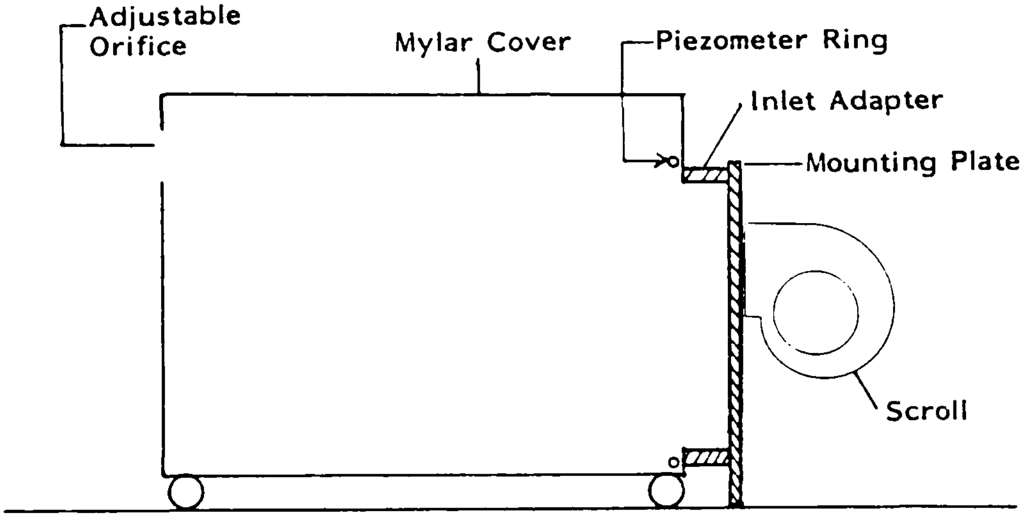

Figure 7. Schematic Representation of INCE Test Plenum. The plenum was contructed according to guidelines provided in INCE RP 1-85. The inlet adapter consisted of a wood frame attached to the rubber mounting panel. A foam gasket was used between the blower assembly and the inlet adapter to minimize leakage.

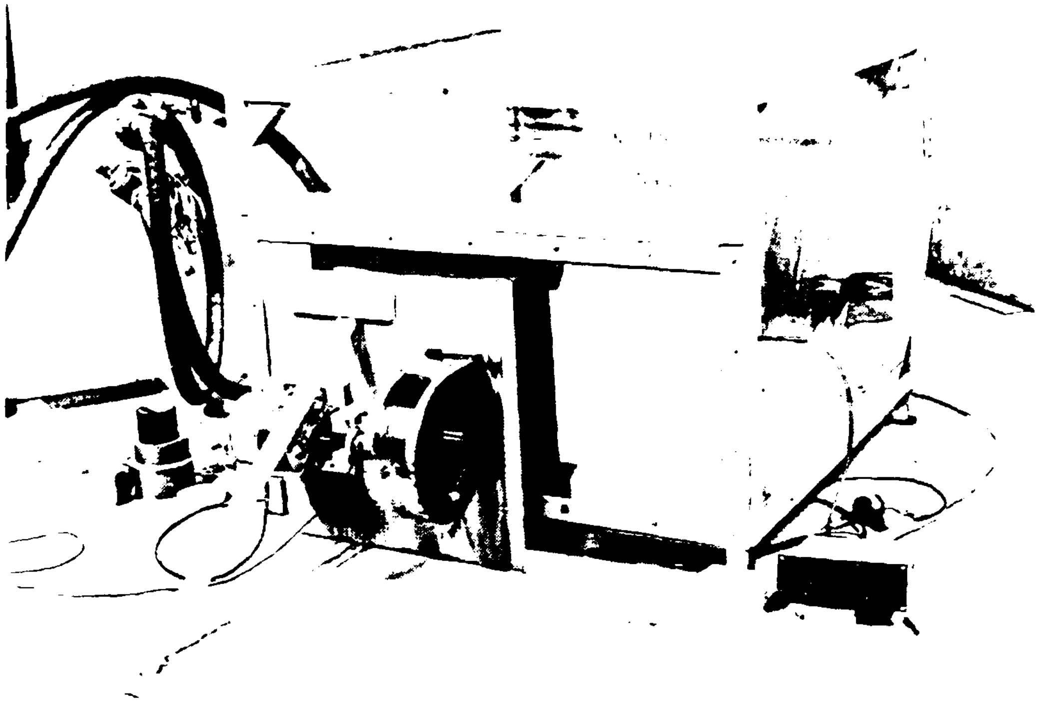

Figure 8. Photograph of INCE Test Plenum and Blower Assembly. The test apparatus is shown here installed in the reverberation room.

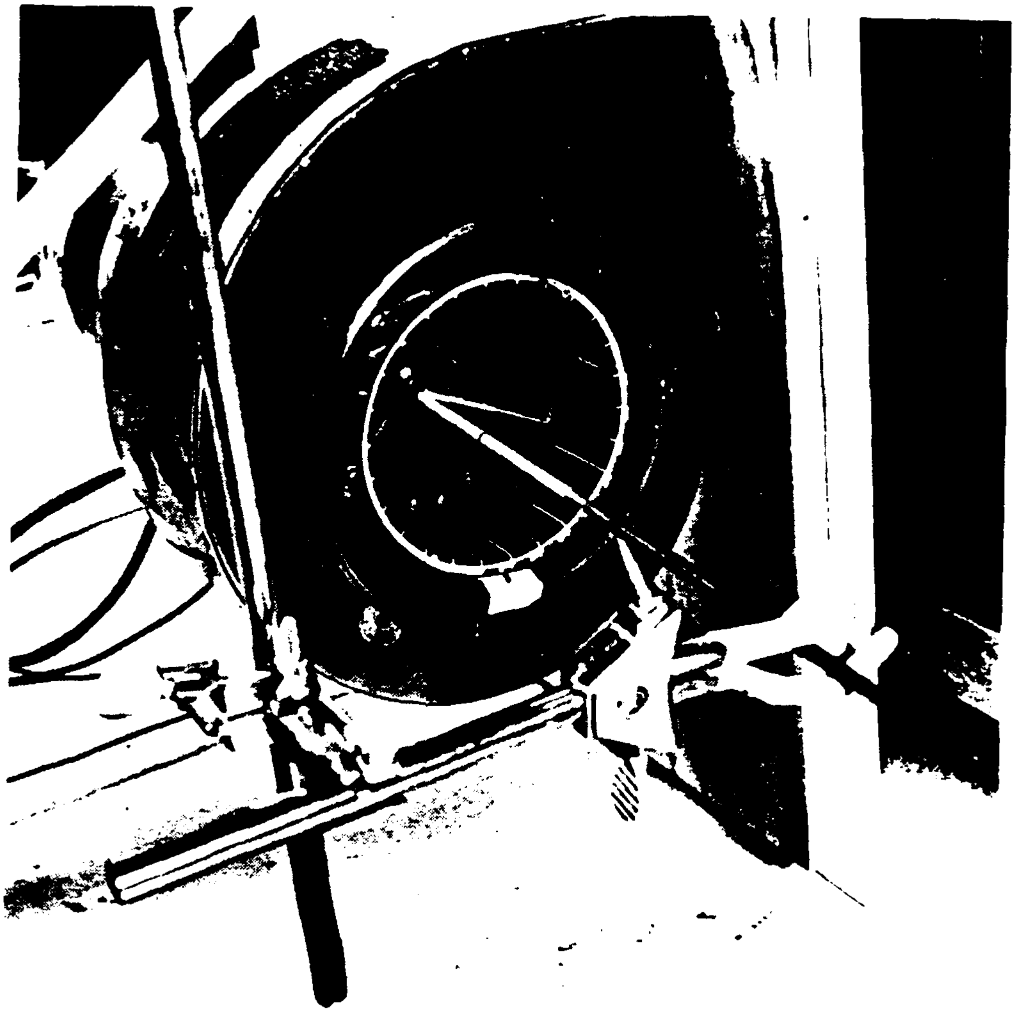

Figure 9. Photograph of Hot Film Sensor and Modified Probe Support. The sensor was located as close to the blade edges as possible; typically less than 1 mm away.

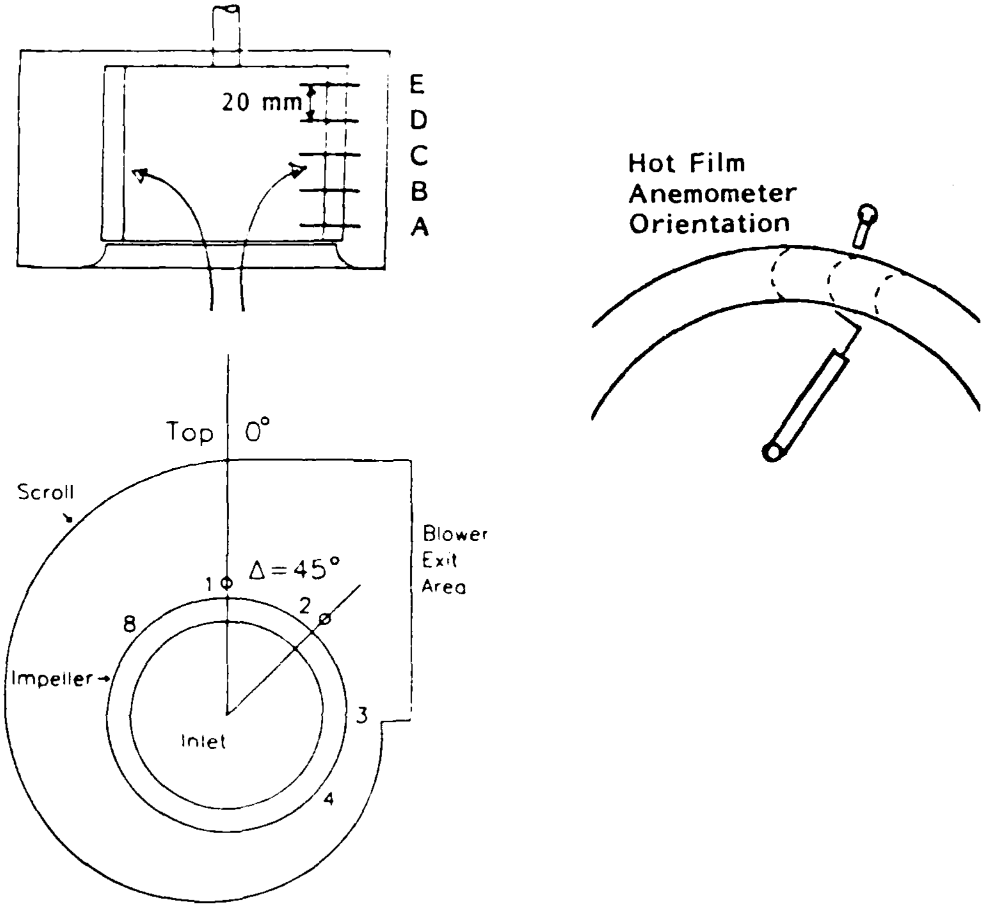

Figure 10. Velocity Sensor Locations and Orientations. The spanwise and circumferential measurement grid around impeller is shown along with the sensor orientations used for the blade channel inlet/outlet velocity determinations. The indicated sensor orientations allow a single element sensor to be used to measure the radial velocity component.

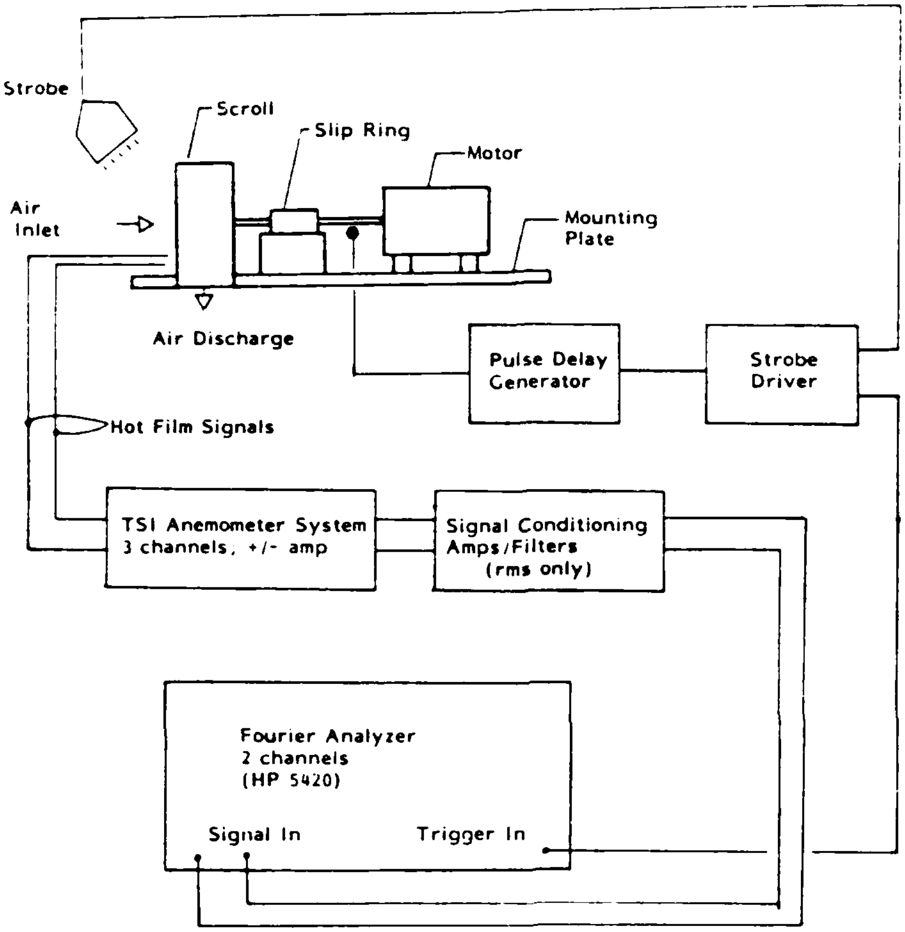

Figure 11. Instrumentation Setup Used for Visually Aligned Triggering Scheme. The variable delay generator was used to visually align the sensor with the strobed rotating impeller.

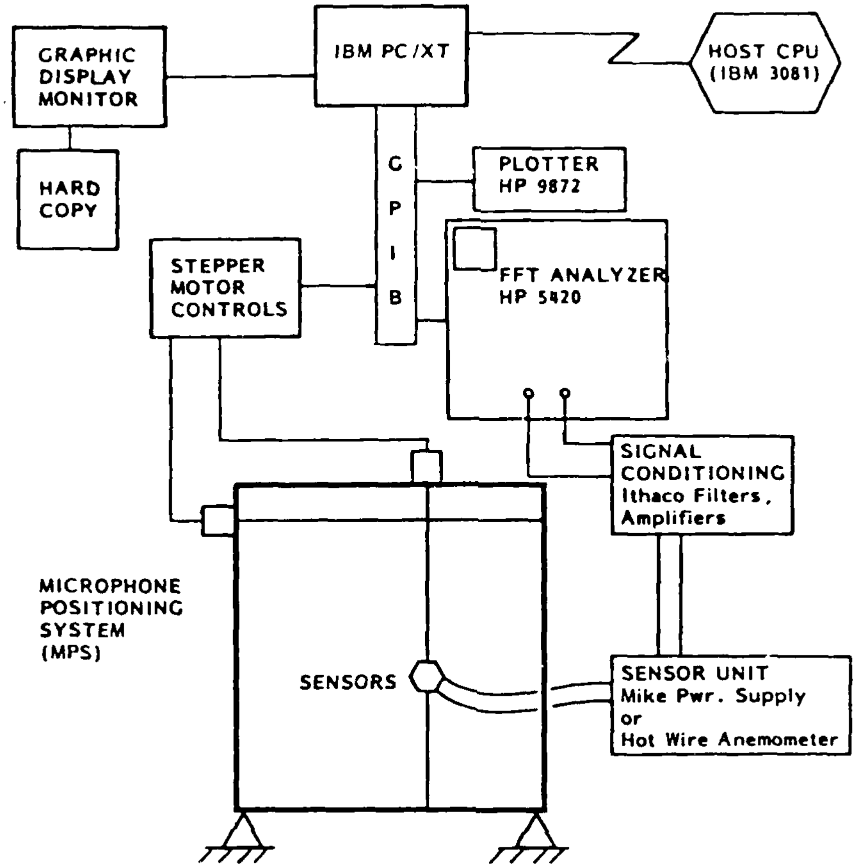

Figure 12. **Schematic of Instrumentation Setup Used for Microphone Positioning System (MPS).** The host connection operates at channel speeds for rapid data and file transfers.

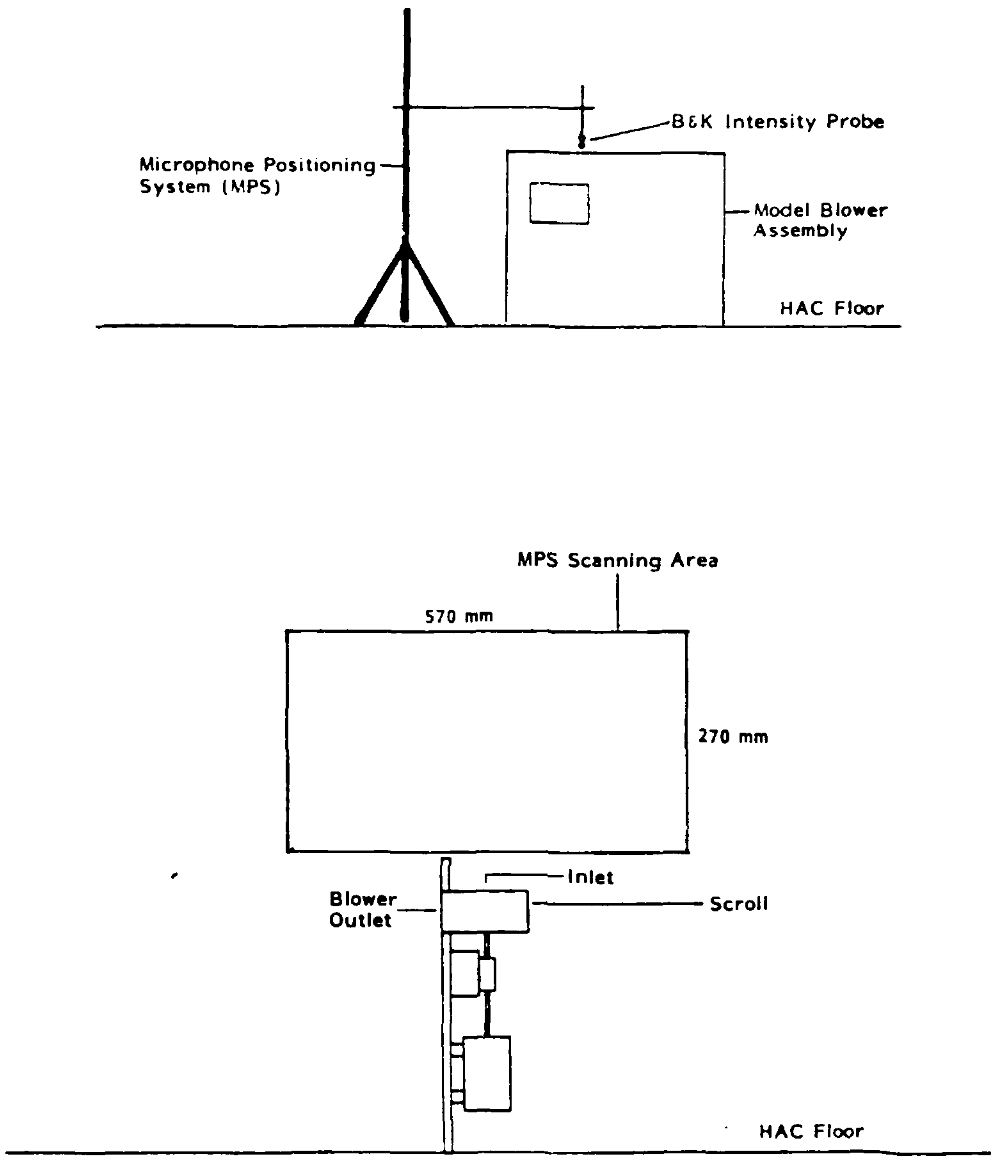

Figure 13. Schematic of Blower Installation for Intensity Maps. The scans were performed in a plane which was aligned with the axis of rotation of the air moving device impeller.

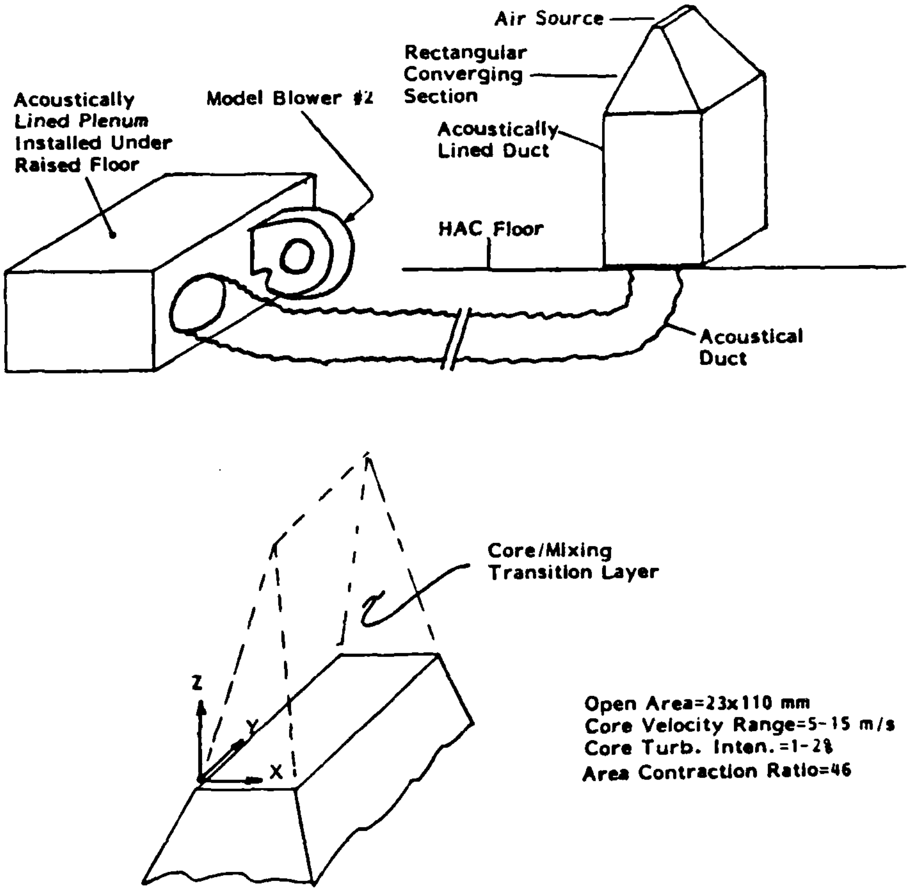

Enlarged View of Nozzle

Figure 14. Schematic Representation of Quiet Air Source

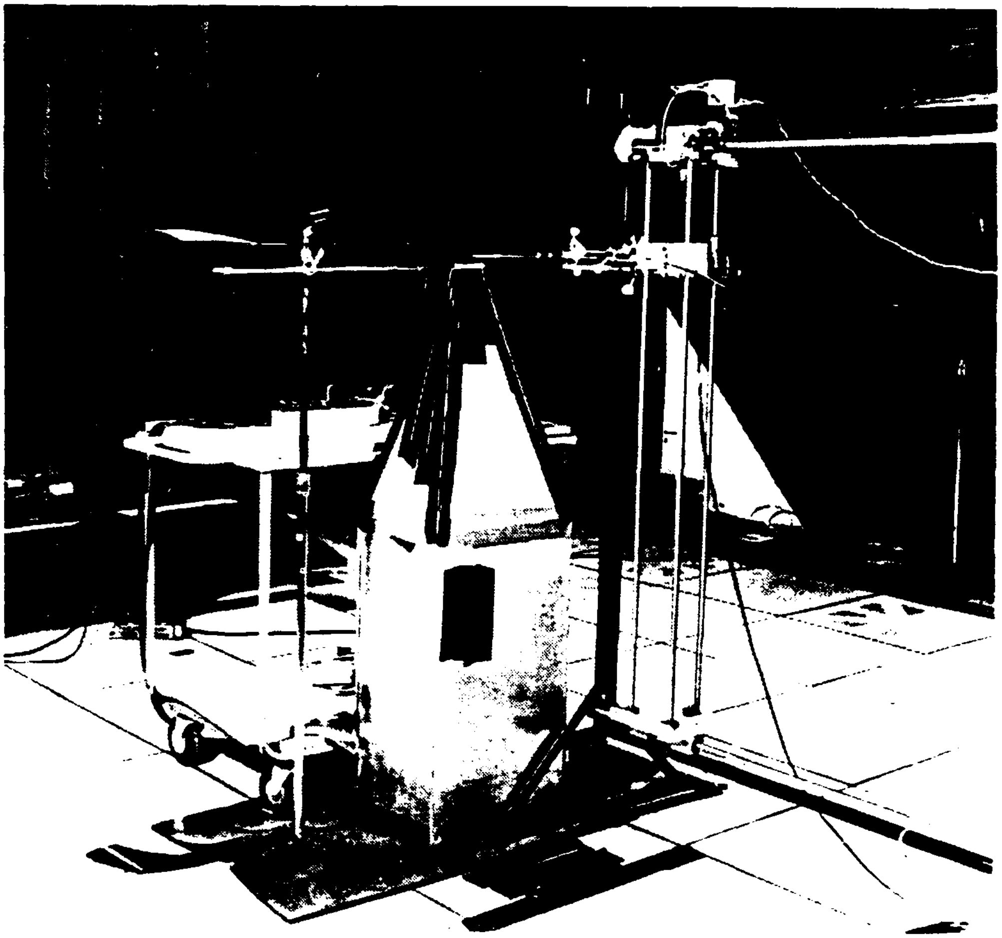

Figure 15. Photograph of Quiet Air Source Installed in Hemi-Anechoic Chamber. The Microphone Positioning System shown in the photo was also used for positioning a hot film sensor in the flow field for the purpose of field characterization.

Chapter 4. General Blower Characterization

Included in this section are results of three different types of measurements made on the model blower in an effort to characterize the overall air performance, the radiated acoustic power, and the distribution of sound intensity near the blower inlet. Details of the measurement methodology used for each set of experiments are given in the appropriate subsection of Section 3.2, "Task-Specific Test Setups."

4.1 Air Performance

The overall air performance of the model blower is given in Figure 16 where the head-flow relationship is plotted. Since the model blower is a 2x scale model of a half-width version of the reference blower with the same tip speed Mach number, an estimate of the relative air performance of the two blowers using the fan laws of Equation (3.1) and Equation (3.2) indicates that they should provide the same amount of air moving capacity.

For convenience, a least squares curve fitting process was applied to the empirical head-flow data to produce approximate expressions that were used to estimate the pressure head P from the flow Q, or vice versa.

$$P = \sum_{i=0}^{5} a_i Q^i \quad ; \quad Q = \sum_{i=0}^{5} b_i P^i \tag{4.1}$$

where

$a_0 = 2.4545 \times 10^{1}$ $\qquad$ $b_0 = 2.4125 \times 10^{2}$

$a_1 = -1.3826 \times 10^{-1}$ $\qquad$ $b_1 = 3.6601$

$a_2 = 5.5515 \times 10^{-4}$ $\qquad$ $b_2 = -4.1015$

$a_3 = 9.9431 \times 10^{-6}$ $\qquad$ $b_3 = 5.8730 \times 10^{-1}$

$a_4 = -9.8724 \times 10^{-8}$ $\qquad$ $b_4 = -3.2484 \times 10^{-2}$

$a_5 = 2.1029 \times 10^{-10}$ $\qquad$ $b_5 = 5.8926 \times 10^{-4}$

and the pressure and flow rate are in mm of water and liters/s, respectively. These expressions were found to be useful for estimates of the flow when performing tests with the model blower attached to the INCE test plenum, where only the static pressure was known.

The *design point* is the operating point associated with the most efficient operation of an air moving device. The terminology used here for the design point is the best efficiency point or BEP. The BEP for the model blower is indicated in the efficiency curve given in Figure 17 and in the head-flow curve of Figure 16. Most of the aerodynamic measurements were made with the blower operating at the BEP. Specifically, determination of the mean and fluctuating velocity components was done at the BEP of the model blower. Sound power determinations discussed in Section 4.2, "Sound Power," were made over a range of operating points, including the BEP.

4.2 Sound Power

The sound power spectral density of the air moving device was obtained using standardized reverberation room methods [4] The comparison method was used utilizing a Bruel and Kjaer Reference Sound Source Type 4204 calibrated in one-third octave bands by the manufacturer. The use of narrow band FFT techniques required an additional, secondary source calibration which was performed in the IBM Poughkeepsie Acoustics Lab using the free-field over a reflecting plane methods prescribed in national and international standards [5].

In all cases the blower assembly was attached to the INCE test plenum which was installed in the reverberation room. Narrow band and one-third octave band sound power levels are shown in Figure 18 and Figure 19. The data have been A-weighted to emphasize the mid frequency range dominance of the noise. The narrow band spectra show no indication of the blade passage frequency tone normally attributable to rotor-stator interactions in the vicinity of the cutoff of the volute. For a rotational rate of 1780 r/min and 26 blades, the frequency of the tone is 770 Hz. The design objective of minimizing the discrete tone noise due to proximity of the blade and tongue thus was achieved. The primary frequency region of dominant random noise from 250 Hz to 2500 Hz is also apparent from the power spectra.

The effect of operating point on the radiated noise is clearly demonstrated by the decrease in noise levels as the BEP is approached. Not only do the overall levels change, but so do the spectral distributions, although not very dramatically for this particular air moving device. This was pointed out by Maling [57] who obtained an empirically based characteristic spectrum for a family of blowers which was dependent on the point of operation; that is, a change in the point of operation was accompanied by a spectral redistribution of the acoustic energy. This phenomenon is consistent with the fact that the incidence angle of the flow is directly related to the volumetric flow rate through the blower (see Section A.3, "Cascade Analysis and Terminology," and Section 5.3, "Measurements Applied to Cascade Analysis," for further discussion of the incidence angle effects).

4.3 Sound Intensity Distribution

In an effort to characterize the radiation field in the vicinity of the inlet to an air moving device a set of experiments was performed to measure the distribution of active acoustic intensity in a plane centered on the air moving device inlet. Details of the measurement procedures are given in Section 3.2.4, "Microphone Positioning System." This section contains the experimental results. Results of the axial fan measurements were published previously in Reference [97], but the centrifugal blower data are new.

The axial fan was mounted in the plane of the reflective floor discharging air under the raised floor. A typical intensity spectrum of the fan operating at free delivery is shown in Figure 20. The intensity distribution of the fan was examined at the fundamental blade passage frequency, at several harmonics, and at other frequencies not related to the rotational speed of the fan. For most of the frequency spectrum, radiation of energy from the fan inlet was uniform and propagating away from the fan with little or no recirculation. This was true even for the second and third harmonics of the blade passage frequency. However, an acoustic recirculation zone was apparent for the fundamental blade passage frequency in which the active intensity vectors were directed toward the fan. This is shown in Figure 21. Recirculation of acoustic energy is characteristic of multipole source radiation or multiple coherent source interactions. See Reference [28] for examples of the intensity field of complex sources. The recirculation indicated for this configuration is consistent with the complex acoustic source distribution established by the partially coherent rotor-stator interactions distributed over the periphery of the fan. The interactions could also be the result of nonuniform blade tip clearance which would cause modulation of the inlet field. Whatever the cause for the apparent acoustic source interactions, they are manifested in the intensity field near the inlet of the air moving device.

In order to measure the intensity field of the model blower, it was installed in the hemi-anechoic chamber in an orientation accessible to the scanning apparatus (see Figure 13 for blower installation details). The intensity spectrum of the model blower contained no indication of discrete frequency energy. This is in contrast with the fan noise which is dominated by narrow band energy related to the rotor-stator interactions. As a result a much wider bandwidth was used in which to examine the acoustic intensity field distribution; 25 Hz for the blower experiments and 3 Hz for the fan data.

The intensity distribution was measured over an area 570 mm × 270 mm high, centered over the blower inlet. In order to reduce the effects of wind gusts for points near the discharge area of the blower a thin sheet of 6.35-mm thick acoustical foam was stretched loosely over the blower exit area. The 60-cm × 120-cm foam sheet was secured at both ends and placed so as to deflect the exhaust air from the sampling region. A thin sheet of plywood was used to support the blower assembly in the upright position. The plywood support was angled away from the discharge area and covered with acoustical foam to minimize its effect on the radiated intensity field.

The 200-point intensity distribution for the frequency band centered on 675 Hz is shown in Figure 22. Comparison of this with the fan data indicates that the source interactions present in the fan are not manifested in the radiated intensity field of the centrifugal blower. This is not surprising since, for the fan, at the frequencies not associated with the rotation of the blades the intensity distribution was quite uniform showing no signs of complex radiation patterns or recirculating acoustical energy. In order for source interactions to occur the source distribution must be at least partially self-coherent. That is, there must be a statistically dependent feature of the multiple sources involved with the noise generation process. For rotating, random aerodynamic sources, where many statistically independent source regions comprise the total source, interactions between regions are not expected to occur.

In summary, it was found that the detailed structure of the centrifugal blower source mechanisms is **not** manifested in the active intensity radiation patterns, even within a fraction of a wavelength of the blower inlet. Some features of the radiation field of complex multipole source configurations were found in the intensity fields of an axial air moving device, indicating the feasibility of local source interactions. These phenomena were associated with rotor-stator source mechanisms and were less prominent at the higher order harmonics of the blade passage frequency and nonexistent for frequencies not related to the rotational speed of the blade set.

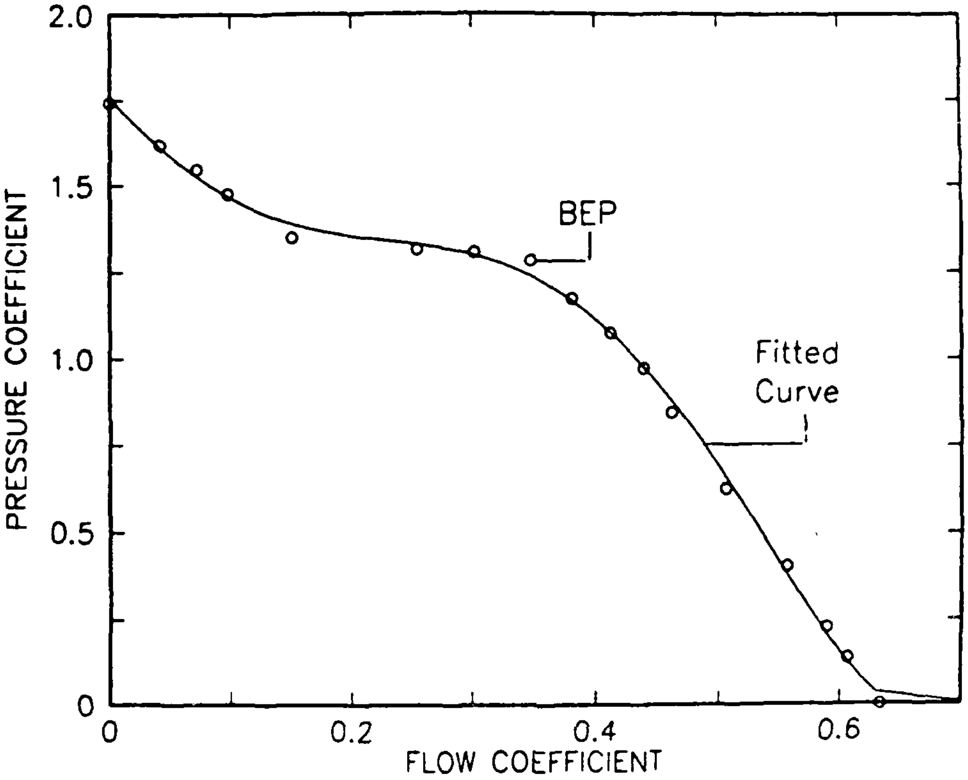

Figure 16. Head-Flow Curve of Model Blower. The discrete data points are indicated with the fitted polynomial shown as a continuous curve. The best efficiency point (BEP) is the point at which the blower was operated for most of the experiments.

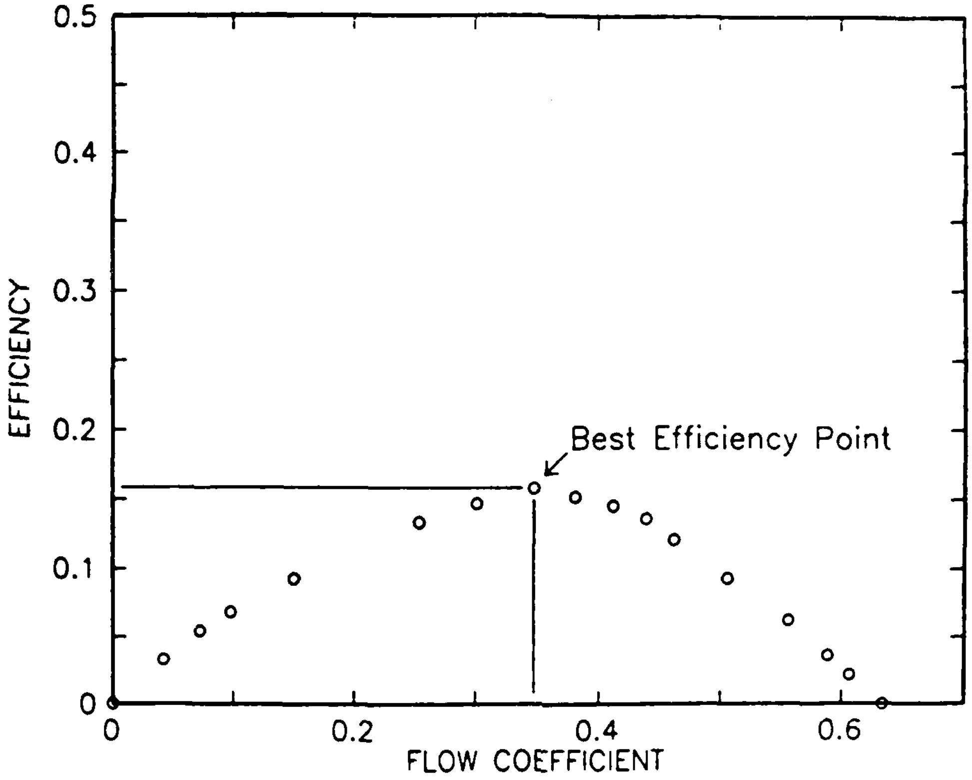

Figure 17. Efficiency of Model Blower. The Best Efficiency Point (BEP) is indicated on the graph. The BEP corresponds to a flow rate of 0.141 m^3/s at a static pressure of 164 pascals (16.7 mm water).

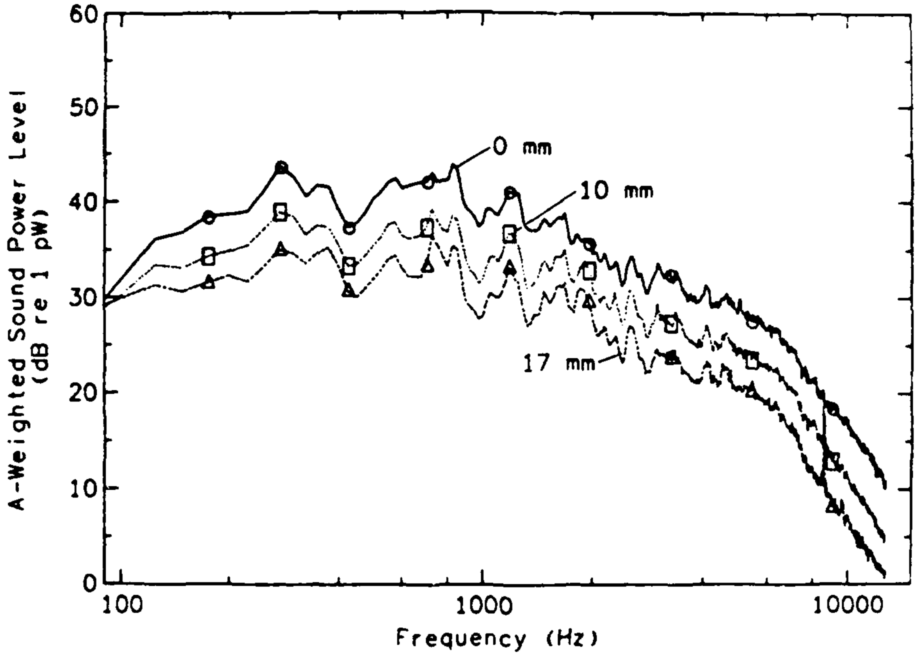

Figure 18. A-Weighted Sound Power Spectral Density of Model Blower. Blower operating at several static pressures attached to INCE test plenum. Overall bandwidth of 12.8 kHz; nominal frequency resolution of 25 Hz; data normalized to 1 Hz bandwidth.

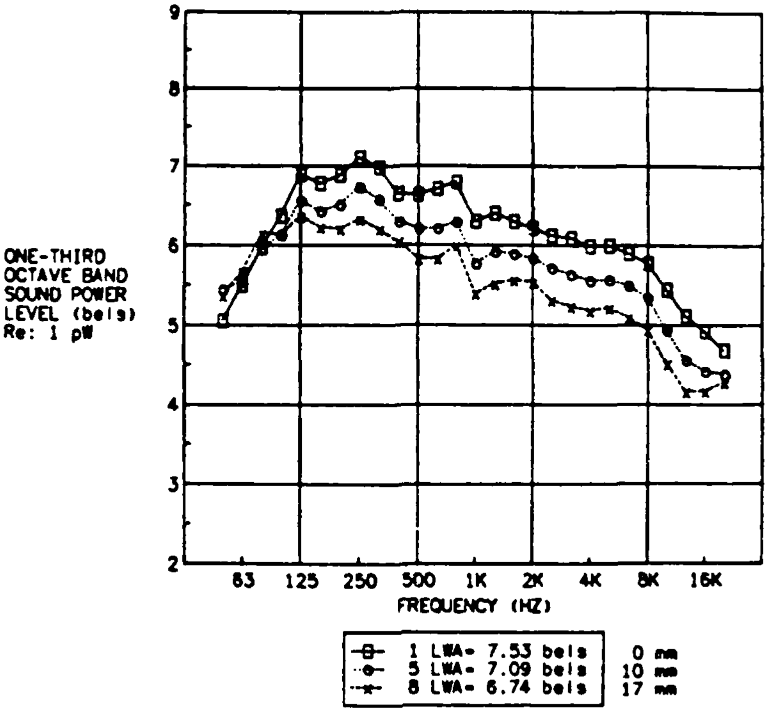

Figure 19. A-Weighted One-Third Octave Band Sound Power of Model Blower. Blower attached to INCE test plenum; operating at same static pressures as for narrow band data shown in the previous figure.

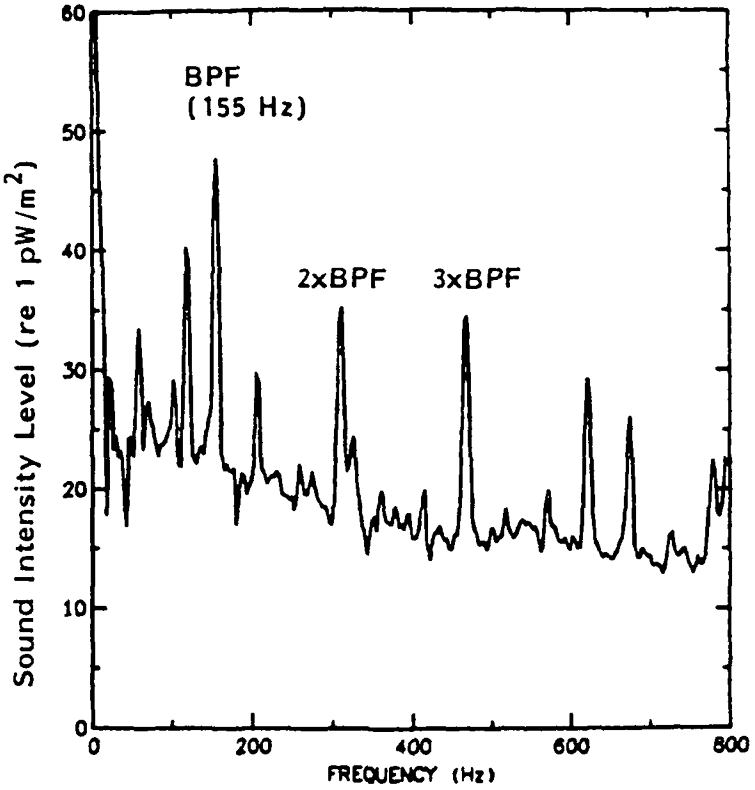

Figure 20. Typical Intensity Spectrum of Axial Fan. Acoustic intensity component measured in direction normal to reflecting plane. Blade passage tone at 155 Hz for three-bladed fan rotating at 3100 r/min. Fan operating at free delivery with unobstructed inlet.

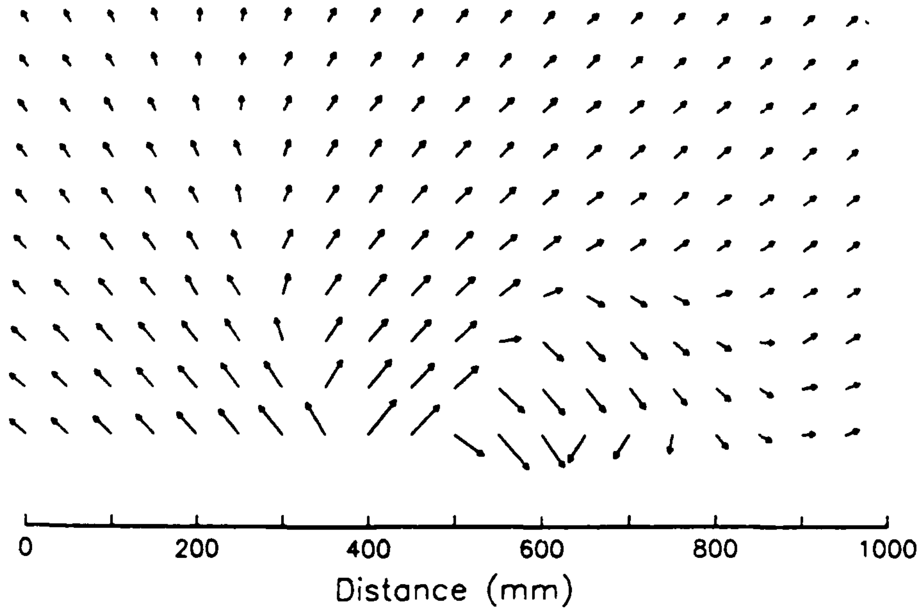

Figure 21. Acoustic Intensity Distribution of Fan at Blade Passage Frequency. The intensity scan was centered over the fan inlet, a vertical distance of 100 mm from the fan. Note the recirculating acoustic field in the right-hand portion of the intensity map.

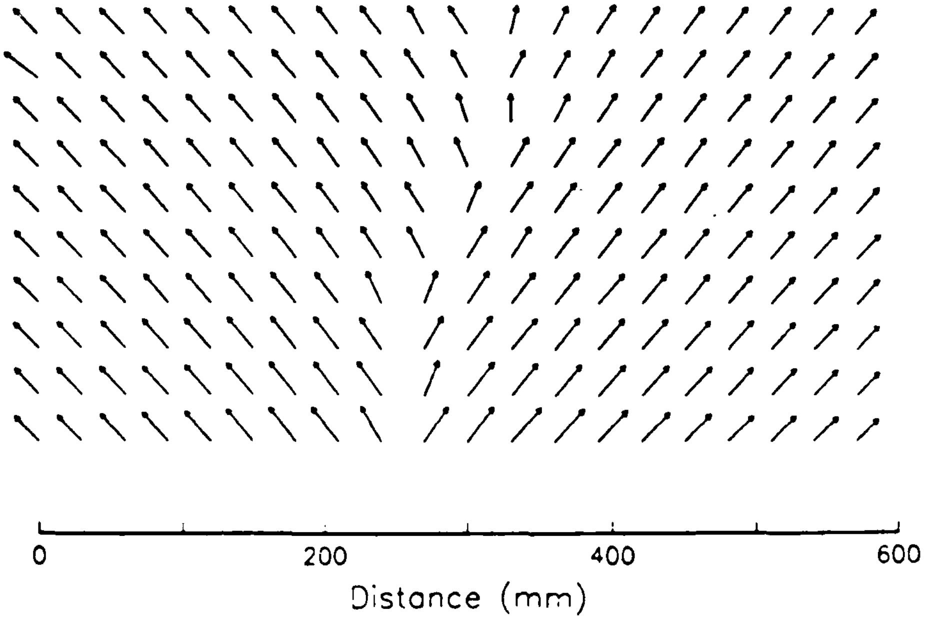

Figure 22. Typical Intensity Map of Centrifugal Blower at 675 Hz

Chapter 5. Aerodynamic Measurements in Model Blower

A key component to understanding the aerodynamic noise generation mechanisms in an air moving device is a knowledge of the mean flow field in the vicinity of the air moving device rotor. This information is crucial for making estimates of the distribution of noise sources since aerodynamic noise generated by an airfoil immersed in flow is largely determined by various parameters of the steady and fluctuating flow field. Measurements were made of the mean and turbulent velocities near the leading and trailing edges of the impeller blade while the model blower was operating at the design point. Results of these measurements are presented in this chapter. Information regarding the mean flow conditions is then used to make estimates of the incidence angle, an important parameter for the analysis or design of an air moving device. These data are preceded by a general discussion of the flow field based on flow visualization experiments.

5.1 Flow Visualization

The importance of flow visualization cannot be overemphasized. A qualitative knowledge of the flow field can be used to formulate alternative approaches to the overall air moving device design, and is indispensable as a first step to a more detailed investigation of the flow field using anemometry or laser doppler velocimetry techniques. There are many different ways to visualize the steady flow.[10] Most direct-injection methods use either neutral helium bubbles or smoke as the visualizing agent.

---

[10] See Chapter 7 of Reference [34] for a good review of the subject.

For the present study, the smoke-wire method was chosen because of its simplicity and because of the improved spatial resolution afforded by the fine smoke streams over the smoke-tube method. Another method of flow visualization, minituft probe, was used at various stages of the project as a means for crudely determining the general alignment of the flow in a particular location inside the blower or in other air streams. This method was used only where smoke streams were not feasible.

Fine smoke streams are generated when a thin resistive wire coated with an oil film is heated. The heated oil forms discrete droplets due to the surface tension of the fluid which vaporize to produce smoke streams. If immersed in a low-turbulence flow field, the streams are entrained by the flow and remain coherent for several centimeters, following the streamlines of the flow. The effectiveness of the smoke-stream method depends on the flow being laminar. This means the wire itself must be quite small to keep from producing a disturbing wake. A maximum Reynolds number of 20 based on the wire diameter has been suggested [34], but, for an average flow velocity of 10 m/s, that would require the use of a wire only 31 microns in diameter! This was not feasible as the wire must withstand a considerable amount of heat in order to vaporize the fluid.[11]

After trying several wires, the best compromise between durability and size was achieved using a 0.38-mm diameter steel wire. The Reynolds number was reduced by moving the wire back from the inlet of the blower thereby reducing the local velocity. The duration of the vaporization, smoke density, and required current through the wire are all interrelated. By reducing the cooling effect on the wire via a smaller local velocity, a lower current could be used thereby increasing the lifetime of the wire and at the same time increasing the duration and density of the smoke streams. Common

---

[11] The inlet velocity of 10 m/s was taken from Table 2 in which the velocity was calculated for the BEP volumetric flow rate through the inlet orifice.

mineral oil was found to produce streams which lasted longer and were more dense than the model-train smoke frequently used for this purpose. This was probably due to the high natural viscosity of the mineral oil which allowed a thicker coat of oil to adhere to the wire.

Smoke streams were used to visualize the inlet flow field of the model blower. The orientation of the wire relative to the blower inlet is shown in Figure 23 on page 112. The blower assembly was attached to the INCE test plenum to maintain the proper operating point. All flow visualization experiments were performed with the blower operating at the BEP. The oiled wire was stretched horizontally across the inlet area of the blower and located approximately 10 cm upstream of the inlet orifice. The horizontal wire orientation prevented the oil droplets from creeping along the wire during vaporization, which was a problem when oriented vertically. Wetting a sufficient portion of the wire allowed the flow across the entire width of the inlet to be visualized with each run. Appropriate selection of the height of the wire allowed various inlet regions to be visualized.

Documenting the visualization experiments was challenging. The lighting conditions were poor in general, especially when attempting to photograph reflective surfaces such as an aluminum impeller. To complicate the situation the smoke streams only last for 1-3 seconds for each run. Many have devised timing circuits to automatically trigger photographic equipment at the precise moment of optimal smoke density. One such circuit is described in Reference [34]. After unsuccessful attempts at real time photography, it was decided to capture the events using video equipment and photograph the video display during playback at a later time. This approach produced good results, and has the added value of repeated views of the flow phenomena.

The wire was positioned at several heights, covering the entire inlet field. A photograph of a typical flow pattern is shown in Figure 24 on page 113. Since it was particularly difficult to obtain clear photographs from the marginal-quality video recordings, the following discussion on the observed phenomena and trends is based on repeated viewings of the flow using video playback.

Efficient Method. The smoke-stream technique was a very effective method for obtaining useful information with a relatively small investment in time or equipment. While high-quality documentation is difficult, reasonable results were obtained using consumer-grade, monochrome video equipment.

Sensor Orientation. The use of single- or multi-element hot film sensors in flow requires *a priori* knowledge of the general direction of the mean velocity vectors. The flow visualization studies showed that the flow in the inlet of the blower was characterized by a strong axial component near the inlet which was converted to radial through-flow from the midspan region to the hub. This information allowed the use of a single-element hot film sensor oriented parallel with the axis of rotation, and placed near the blade leading edge for determining the radial component of the mean velocity. This particular orientation took advantage of the cosine directivity characteristic of the hot film sensors to minimize the effect of the axial component.

Velocity at Leading Edges. The photographs indicate that, at the inlet to the blade channels, the tangential component of the mean velocity is almost negligible. That is, there is very little swirl in the inlet flow field.

Flow Nonuniformities. Both spanwise and circumferential inlet flow nonuniformities were observed. In the spanwise direction, over most of the circumference, the region near the inlet was dominated by purely axial flow with little evidence of air being ingested into the blade channels. In the circumferential direction there was a deficit in the ingested flow in the region near the cutoff and downstream of the cutoff. Both of these trends were confirmed by the hot film sensor data.

Large-Scale Turbulence. As the smoke streams neared the inlet to the blade channels they became unstable and began to deviate in a random fashion from the projected path — *dancing streams*. This phenomenon is believed to be due to large-scale, high-level turbulence in the inlet region. It was not due to ingested eddies from the external environment, otherwise *stream dancing* would have occurred upstream of the blade channels closer to the bellmouth inlet.

Further discussion of the overall flow distribution in the blower impeller is provided in the next section.

5.2 Blade Channel Inlet/Outlet Velocities

The flow field of centrifugal devices has been studied by many researchers [2, 26, 27, 35, 36, 42, 43, 61, 78, 79, 83]. While some studies concentrated on high-speed compressors and others on low-speed centrifugal blowers, all results indicate a common trait among device flows patterns; the detailed flow structure is very complex and usually exhibits considerable secondary flow mixing. A complete understanding of the details of the internal flow patterns has eluded investigators. The objective of this phase of the research is to obtain a general understanding of the overall flow distribution inside the model blower using a conventional anemometry system and straightforward measurement procedures. The intent is to be able to confirm fundamental flow characteristics typically found in similar air moving devices, and to use this information to better understand the distribution of, and mechanisms responsible for, aerodynamic noise sources. An underlying premise in this approach is that for a given volumetric flow rate and static pressure, the minimum noise level is achieved with a uniform distribution of the flow through the impeller, all other things being equal.

Quantification of the mean and turbulent flow was achieved via measurement of the flow velocities at the leading and trailing edges of the impeller blade channels. Details of the measurement procedures can be found in Section 3.2.3, "Blade Channel Inlet/Outlet Velocity Determinations," and will not be reiterated here. In general, the mean and rms radial velocity levels were measured at the inlet and outlet to the blade channels at several locations in the model blower. The measurement sampling grid is shown in Figure 10. A particular measurement location is identified using an alphanumeric code. For example, L/3E denotes the leading edge, circumferential position 3, and spanwise location E.

5.2.1 Mean Flow Distribution

The basic steady flow structure through the blade channels is exhibited in Figure 25 on page 114. Proper orientation of the hot film sensor enables discrimination against axial flow at the leading edge and tangential flow at the trailing edge, thus providing an approximate measure of the radial velocity component at both locations.[12] At the leading edge (L/1C) the flow deficit is due to the passage of the blade edge and the associated boundary layer. The upstream effects of the complex

---

[12] On the inlet, the sensor directivity allows measurement of the radial velocity by orienting the sensor parallel with the axis of rotation (assuming a small tangential component). At the exit of the blade channels, alignment of the sensor perpendicular to the axis of rotation produces an output proportional to the vector sum of the axial and radial components. Here, the axial component is known to be negligible.

channel flow are evidenced by the periodicity in the velocity profile as the flow enters the blade channel. The channel profile is slightly skewed toward the suction side of the blade channel on the inlet.[13] At the trailing edge the wake structure of the blade channel is more pronounced with a clearly defined region of high through-flow near the center of the blade channel associated with lower flow velocities near the blade surfaces. This general wake structure is typical of flow in centrifugal blowers. For the data presented in Figure 25, a slight skew of the radial velocity profile exists in the inlet profile and is further developed at the exit. The skew in this case is toward the suction side of the blade channel. This is consistent with data presented in [27], but inconsistent with profiles measured by Raj [78].

Relative levels of the total velocity $\vec{v}$ and the radial velocity $\vec{v}_r$ are given in Figure 26 where the trailing edge velocity components (location T/1C) were resolved using two sensor orientations. The increased level of $\vec{v}$ over $\vec{v}_r$ implies a strong tangential velocity component. This is to be expected at the blade channel exit as a result of the transfer of energy from the impeller to the fluid, and the effects of the forward-curved blade shape.

Mean flow nonuniformities were found in both the circumferential and spanwise directions. Those results are presented followed by a discussion of the distribution of turbulent energy based on the measurement of turbulence intensity levels.

In the circumferential domain there was a general tendency for the flow to migrate toward the portion of the scroll opposite the cutoff region (i.e., toward regions 6, 7, 8, and 1). This trend is depicted in Figure 27 on page 115 for the leading edge and in Figure 28 for the trailing edge. For both the blade channel inlet and outlet, the data shown was taken at the position nearest the hub (position E). The velocity pro-

---

[13] For a given blade in a moving blade row, the pressure side passes a stationary sensor before the suction side of the same blade.

files measured in the circumferential regions near the cutoff (position 3) and downstream of the cutoff (positions 4,5) did not fluctuate with the passage of the blade channel and therefore are **not** indicative of the jet-wake pattern characteristic of flow through a blade channel. This trend of low through-flow downstream of the cutoff was observed at all spanwise positions between midspan and the hub. The aperiodic traces indicate a strong tangential velocity, but the direction of flow cannot be determined with the present measurement procedure.

The second region exhibiting reduced through-flow was found to be over the entire circumference, but just in the spanwise region near the inlet shroud (i.e., positions A and B in Figure 10 on page 79) The effects of the starved inlet area were not as prevalent at the leading edges as at the trailing edge, but nevertheless did exist in both areas. The measured radial velocity profiles for position 6 (225° clockwise from the top of the scroll) are shown in Figures 29 and 30 on page 116 for the leading and trailing edges, respectively. The jet-wake pattern characterizing dominant blade passage through flow is significantly enhanced for the regions near the hub (positions C, D, and E). Through-flow in the leading-edge inlet shroud area (positions A and B) however is lower at position A and marginally lower at position B than at the inner hub positions C, D, and E (see Figure 29), and for the trailing edge the effect is even more pronounced (viz., positions A and B in Figure 30).

The mean flow patterns are best summarized by averaging the radial velocity data across the blade channel and examining the circumferential variation at both the leading and trailing edges. The data presented in Figure 31 are for the leading edge variations, and the trailing edge data are shown in Figure 32. Caution should be exercised in averaging data of this type since the effects of a strong tangential component at the leading edge and a strong axial component at the trailing edge are inherent in the sensor response. The resulting average may not display the same trends which were obtained from inspection based on periodicity information. In this case the averaged data do exemplify the flow patterns just discussed. In particular, at the leading edge (see Figure 31 on page 117) a wide variation in the average velocity across the span occurs near the cutoff which indicates a nonuniform flow profile across the blade span. At other circumferential locations, the reduced flow near the inlet shroud is depicted by the lower average velocity at position A. At the trailing edge (see Figure 32) the through-flow deficit at and downstream of the cutoff is quite pronounced. In addition the reduced flow region near the inlet shroud is evidenced by lower average flow velocities at positions A and B. The final simplifying step was to average over one more dimension producing traces in Figure 33 and Figure 34. The general trends previously discussed are clearly shown in these two figures.

This completes the mean flow distribution pattern identification. A brief discussion of measured turbulence levels will be presented next, followed by use of the mean flow data to estimate incidence angles in Section 5.3, "Measurements Applied to Cascade Analysis."

5.2.2 Turbulence Intensity Levels

The turbulence intensity (TI) levels were measured in the leading and trailing edge areas at 8 circumferential locations (positions 1-8 as defined in Figure 10 on page 79), all at the midspan position C. The same sensor orientations were used for TI determinations as for radial mean velocity measurements; that is, parallel to the axis of rotation at the leading edge and perpendicular to the axis of rotation for the trailing edge. Care was taken to ensure that the triggering circuit was stable, and this was verified by visualizing the *frozen* blade row during the measurements. Variability in the trigger location could produce excessively high TI levels due to the spatial variation in the mean flow patterns (i.e., jet-wake profile). It was also important to avoid any disturbances in the inlet flow field during these measurements which might result from inlet obstructions such as the measurement apparatus or other support hardware.

The turbulence levels were generally quite high, considering that upstream of the inlet TI levels of approximately 1-5% were found. Figure 35 on page 119 shows a typical turbulence velocity profile taken at the midspan position, trailing edge, circumferential location 1 (top of scroll), superimposed with the corresponding mean velocity (SS and PS in the figure correspond to suction and pressure side locations, respectively). This particular trace was not normalized to the local velocity to yield turbulence intensity in percent because of the periodic nature of both the mean and rms velocities. There is useful information in the time history of the velocities (viz., the relationship between periodicity and through-flow) that would be lost or distorted if normalized. Two features of the turbulent flow are demonstrated in Figure 35 that were found at most of the other locations around the impeller:

- The turbulence profiles were periodic at both the leading and trailing edges of the blades. The rms velocity levels depended not only on the spatial location around the impeller (i.e., *circumferential, spanwise, and chordwise*), but on the specific location relative to the blade channel.

- The spatially periodic turbulence levels were consistently higher near the suction surface of the blades with reduced turbulence near the pressure surface, although at some trailing edge locations the region of increased turbulence nearly filled the entire blade channel. This is consistent with separated flow or shed vortices from the suction surface of the blade, and a steady, turbulent boundary layer on the pressure side.

The overall trends in turbulence are demonstrated in Figure 36 which is a plot of the turbulence level averaged across three blade channels for measurements taken at the midspan position C. These data have been normalized to the local velocity to produce turbulence intensity in percent of the mean radial velocity. Normalization does not cause any distortion in this case since the spatial fluctuations have been averaged out. The two primary features of the turbulent field are:

- At the leading edge, excessively high turbulence intensity is present at the scroll cutoff and downstream of the cutoff region. Turbulence intensity in these areas is markedly higher than over the rest of the scroll circumference, and even exceeds levels at the trailing edge. This phenomenon is characteristic of the turbulent, low through-flow aerodynamic field which exists in this region as discussed in the previous section.

- In regions other than at the cutoff, the turbulence intensity levels are significantly higher at the blade passage outlet than at the inlet. This phenomenon is typical of blade channel flow and is consistent with results presented by other researchers [78].

It is also interesting to note that the turbulence levels are in fact quite low over most of the blade channel inlet area, thus indicating relatively smooth inlet conditions; that is, minimal effects from inlet protuberances.

5.3 Measurements Applied to Cascade Analysis

A general cascade analysis approach is presented in Section A.3, "Cascade Analysis and Terminology." This section will build on the model established in that section and employ data from Section 5.2, "Blade Channel Inlet/Outlet Velocities," on the mean flow velocities to estimate the incidence angle of the flow relative to the tangent leading edge camber line of the blade.

Knowledge of the rotational speed of the impeller, the blade geometry, and the mean flow velocity relative to a fixed reference frame allows calculation of the incidence angle.[14] A typical inlet velocity profile was shown in Figure 25 which indicated a mean radial velocity range if 5-10 m/s with the low end of the range corresponding to the flow at the blade surface. It has generally been assumed in this investigation, and verified through-flow visualization, that the tangential flow at the blade channel inlet is negligible; thus the measured velocity vectors have been referred to as radial components.

For a rotational speed N of 1780 r/min and impeller blade leading edge radius r of 64 mm, the tangential blade speed U is

$$U = \Omega r = (2\pi \times N/60) \times r \cong 12 \text{ m/s} \tag{5.1}$$

A cascade is defined as the intersection of the blade row with a stream surface. Assuming a negligible axial component, the intersection of the stream surface with the blade row produces a simplified two-dimensional cascade flow model. This assumption is valid at the trailing edge across the entire blade span, and at the leading edge for the inner blade span near the hub. There remains some question about the axial flow at the leading edge near the inlet shroud, but there is such low through-flow in this region that the applicability of this simplified cascade analysis is a moot point. From the velocity diagram shown in Figure 79 on page 196 the inlet *fluid angle* is the angle formed by the flow velocity and the normal to the line connecting the blade tips (i.e., the *pitch line*). The inlet *blade angle* is determined by the geometry of the impeller and

---

[14] The *incidence angle*, as defined in Section A.3, "Cascade Analysis and Terminology," is the angle between fluid flow and the blade camber line at the inlet to the blade.

is defined as the angle between the normal to the pitch line and the tangent to the camber line at the leading edge of the blade. Thus, the *incidence angle*, ι, is the difference between the inlet blade angle γ'_1 and the inlet fluid angle γ_1. For the design point of the model blower, the radial velocity at the leading edge in the midspan region is of the order of 5 m/s. Thus, the inlet *fluid angle* is approximated by

$$\gamma_1 = \tan^{-1} \frac{U}{|\vec{v}_r|} \cong \tan^{-1} \frac{12}{5} = 67^\circ \tag{5.2}$$

Therefore, since the blade angle is 15°, the incidence angle is 52°. The incidence angle is schematically depicted in Figure 37. This simplified analysis has assumed a negligible tangential velocity component. If in fact, the measured velocity component (5 m/s) contains a tangential component such that the inlet swirl is in the direction of rotation, then the incidence angle of 52° would decrease by an amount equal to the angle between the radial unit vector and the direction of the actual vector sum of the radial and tangential velocities.

As discussed in Section A.3, "Cascade Analysis and Terminology," the incidence angle is an important factor in the design of an air moving device and provides some measure of the flow geometry over the individual blade. It is sufficient to say that for this particular impeller configuration, the incidence angle deviates significantly from an ideal of grazing incidence. Excessive incidence angles can lead to flow separation over a large portion of the suction surface. Separated flow over the blade surfaces has the compound effect of directly generating excessive noise due to the local turbulence, and, decreasing the air moving device efficiency (which has an indirect effect on the noise level by requiring a larger air moving device for a given pumping requirement). The experimentally determined information that $\iota > 0$ will be used to develop a fluid flow model using numerical techniques. This topic is covered in Section 6.1, "Results of FLUENT Model of Single Blade."

5.4 Conclusions

Measurements have been presented on the mean and turbulent flow field distribution in the model blower operating at the design point. This information has been coupled with the flow visualization experiments to reach the following conclusions:

1. The mean flow in the model blower is nonuniform in both the circumferential and spanwise directions. There is evidence of a flow deficit over the entire circumference for the spanwise region near the inlet shroud covering the outer 20-40% of the blade span. There is also a region just downstream of the scroll cutoff in which the flow through the blade passages is deficient.

2. The turbulent field exhibited high turbulence intensity levels over most of the circumference at the trailing edges, and near the cutoff region at the leading edges. This pattern is consistent with item 1, above.

3. The turbulence levels measured at the leading edges increase significantly in the low through-flow region just downstream of the cutoff. This is due to the random nature of the flow field in that region possibly due to insufficient scroll-to-blade-tip clearance.

4. Measurement of the mean flow velocity at the inlet to the impeller enabled estimates of the incidence angle. These estimates indicate an excessively large incidence angle which could cause an enlarged separation region over the suction

surface of the blade. This behavior is consistent with the circumferential distribution of turbulence within a single blade passage at the blade channel exit which shows increased turbulence near the suction surface side of the blade channel exit.

The above conclusions are in general agreement with previously published data [78], with a more extensive treatment of the blade channel inlet region presented here.

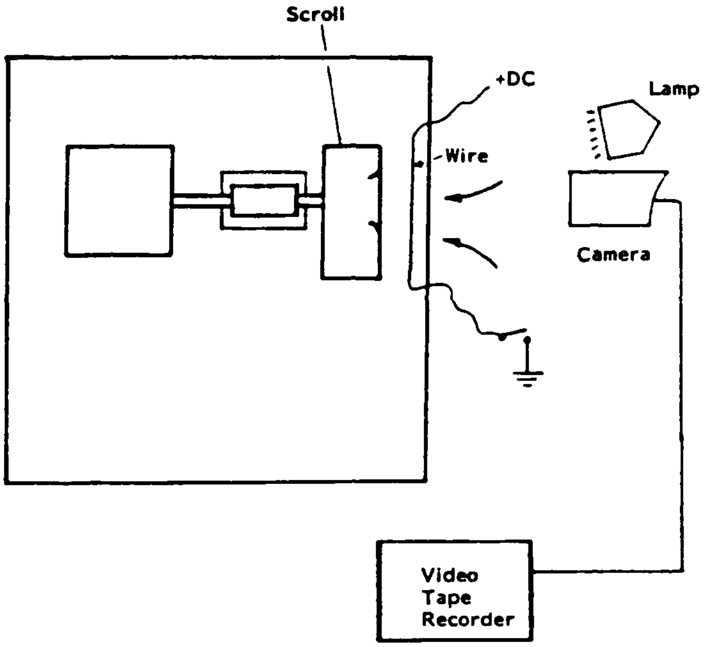

Re - 240 *
Steel wire diameter - 0.38 mm (0.015")
Resistance - 0.0217 ohms/cm
Current - 6 amps
Time - 1-3 sec.

Figure 23. Schematic of Flow Visualization Setup. The wire was positioned so that the streams were ingested into the inlet at various locations. Each row of streams provided information on a different cross section of the blower inlet.

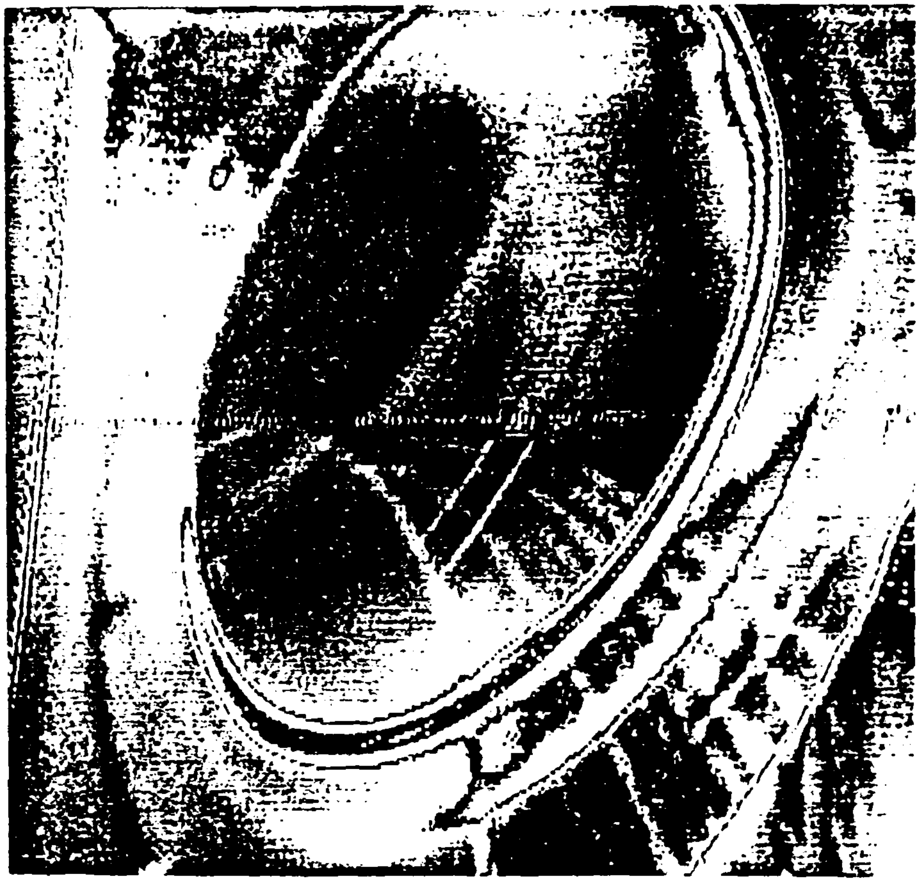

Figure 24. Enhanced Photograph of Flow Visualization of Model Blower Inlet. Blower operating at BEP and smoke wire placed opposite the lower edge of the inlet bellmouth. Note the starved region just past the bellmouth where little or no through flow is indicated. (This photograph was obtained by capturing and digitizing a single frame of the video signal, then enhancing the digitized image. The output was printed on an IBM Model 4250 Printer with a resolution of 600 lines per inch. The author acknowledges the efforts of Robert Moorhead and Thomas McCarthy of IBM Research Division for the digitization and image enhancement.)

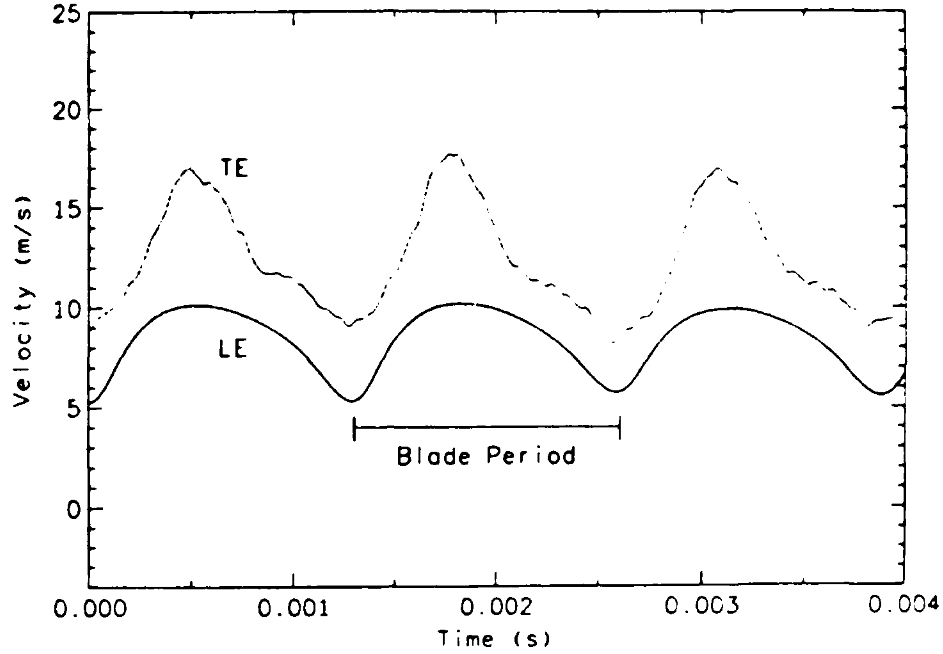

Figure 25. Radial Velocity Profile at Positions L/1C and T/1C

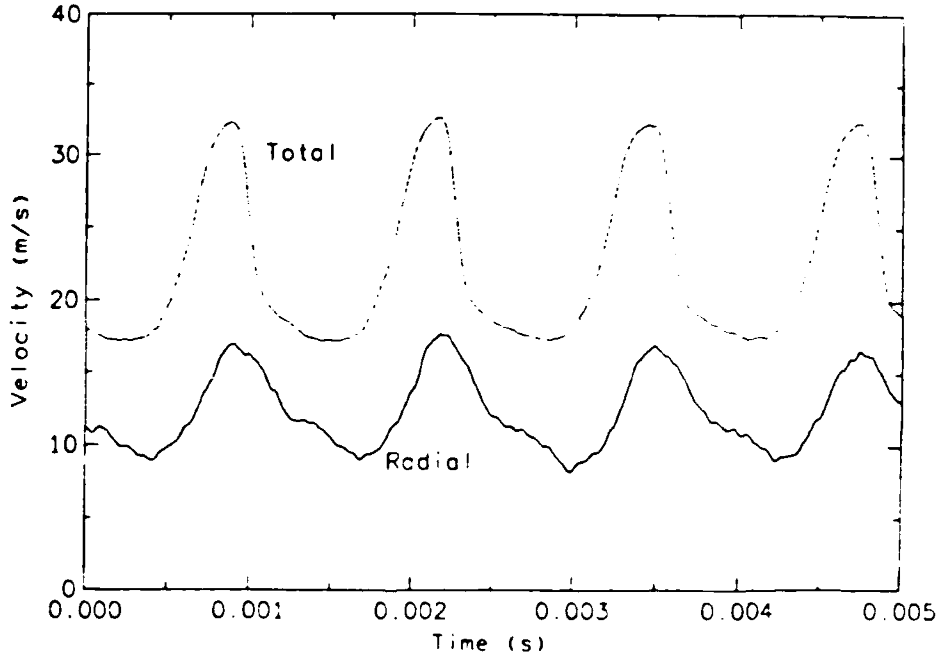

Figure 26. Total and Radial Velocity Levels at Trailing Edge

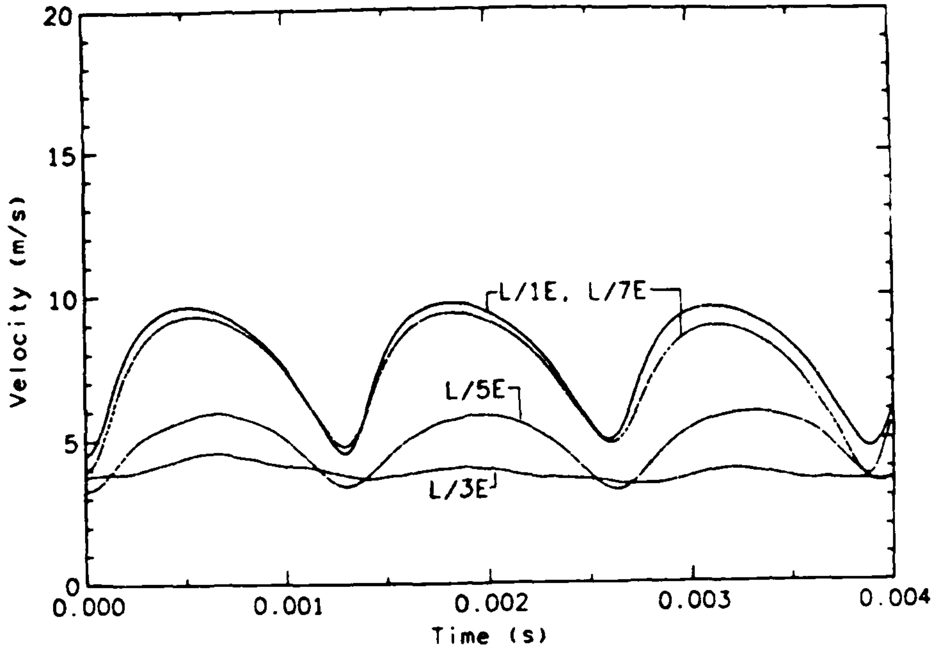

Figure 27. Mean Radial Velocity — Leading Edge, Circumferential Variation.

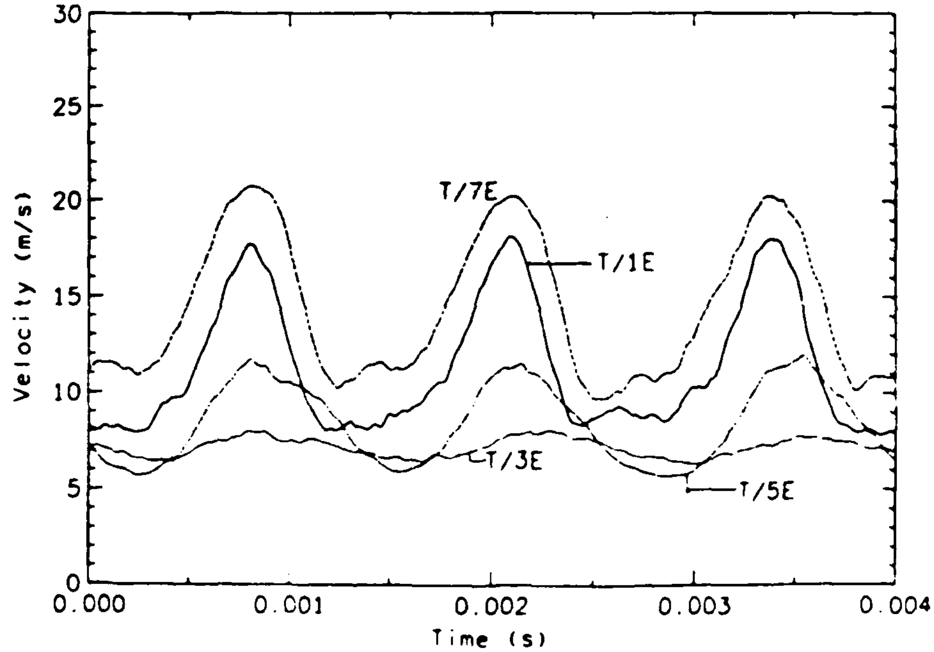

Figure 28. Mean Radial Velocity — Trailing Edge, Circumferential Variation.

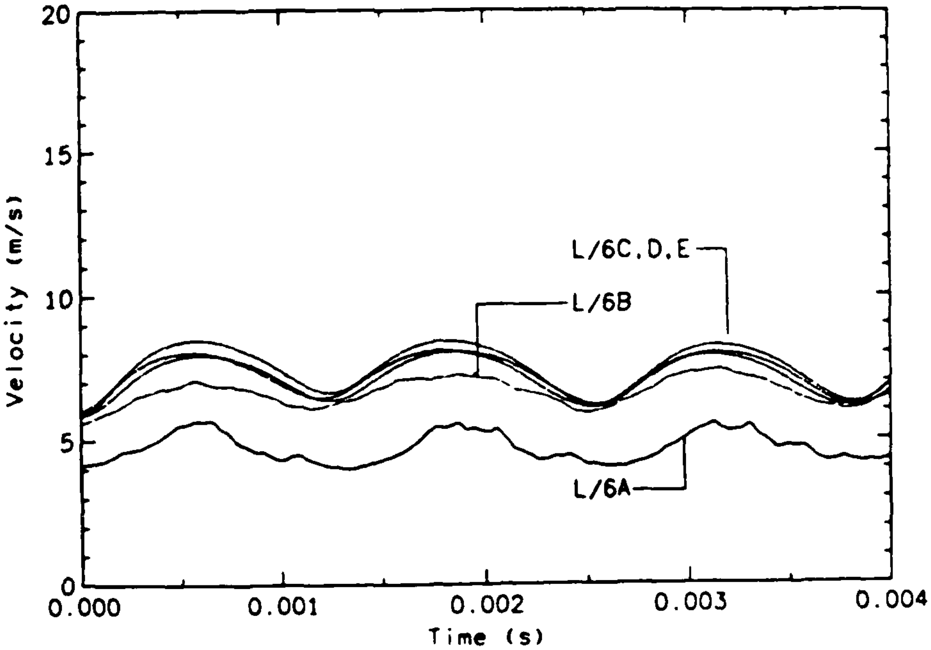

Figure 29. Mean Radial Velocity — Leading Edge, Spanwise Variation.

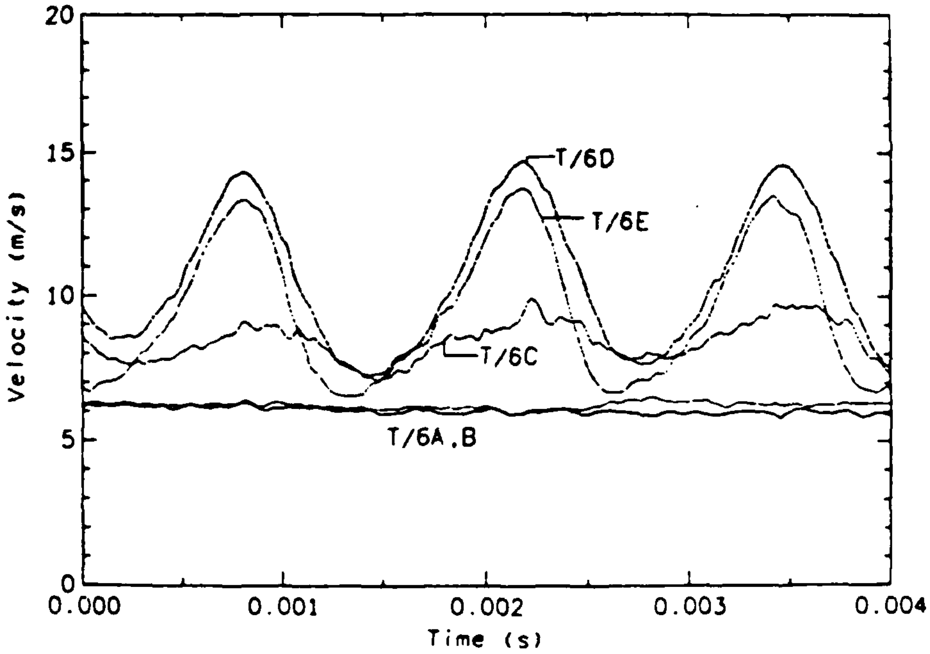

Figure 30. Mean Radial Velocity — Trailing Edge, Spanwise Variation.

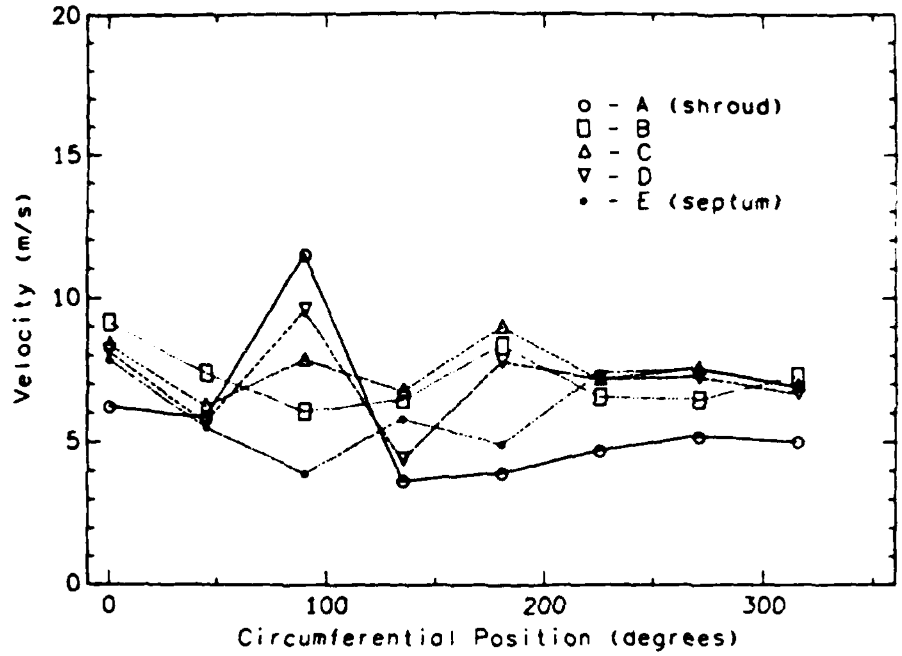

Figure 31. Mean Radial Velocity Averaged Across Blade Channel — Leading Edge.

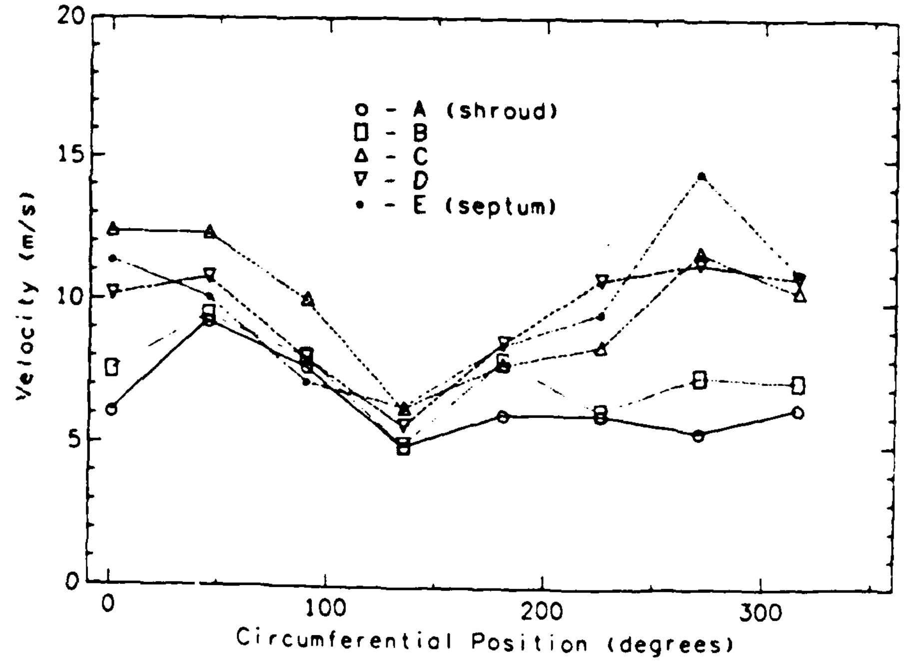

Figure 32. Mean Radial Velocity Averaged Across Blade Channel — Trailing Edge.

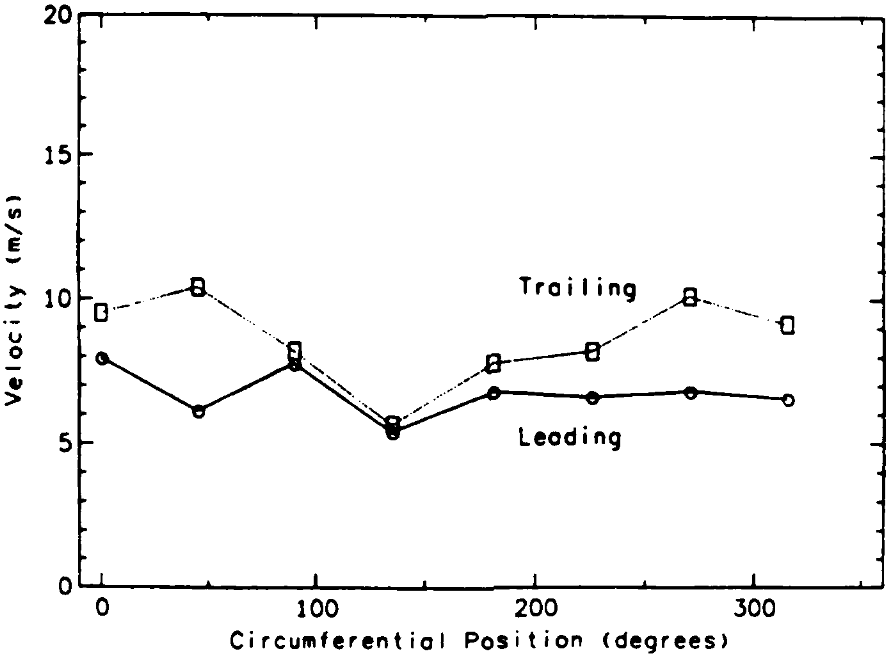

Figure 33. Average Radial Velocity vs Circumferential Position.

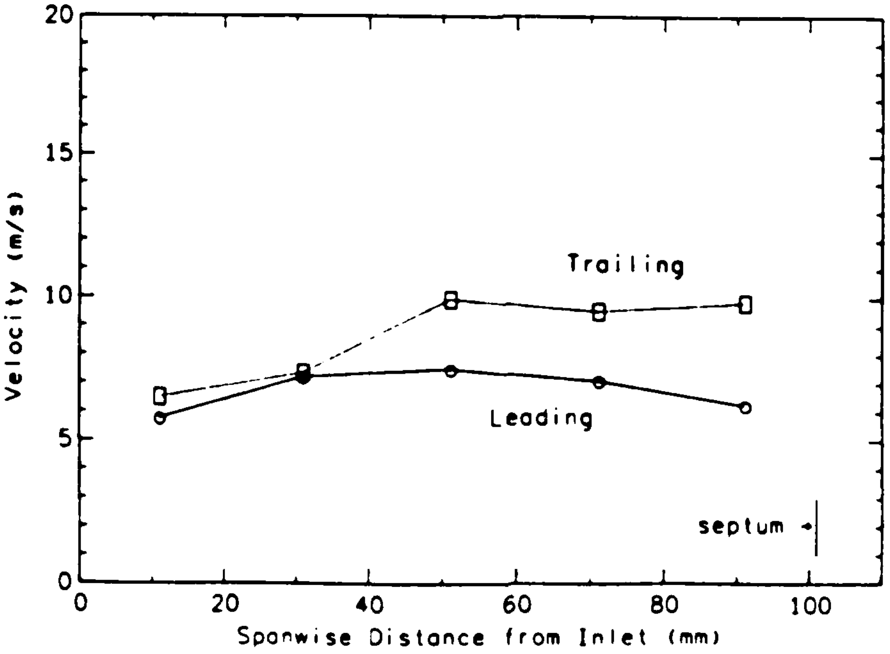

Figure 34. Average Radial Velocity vs Spanwise Position.

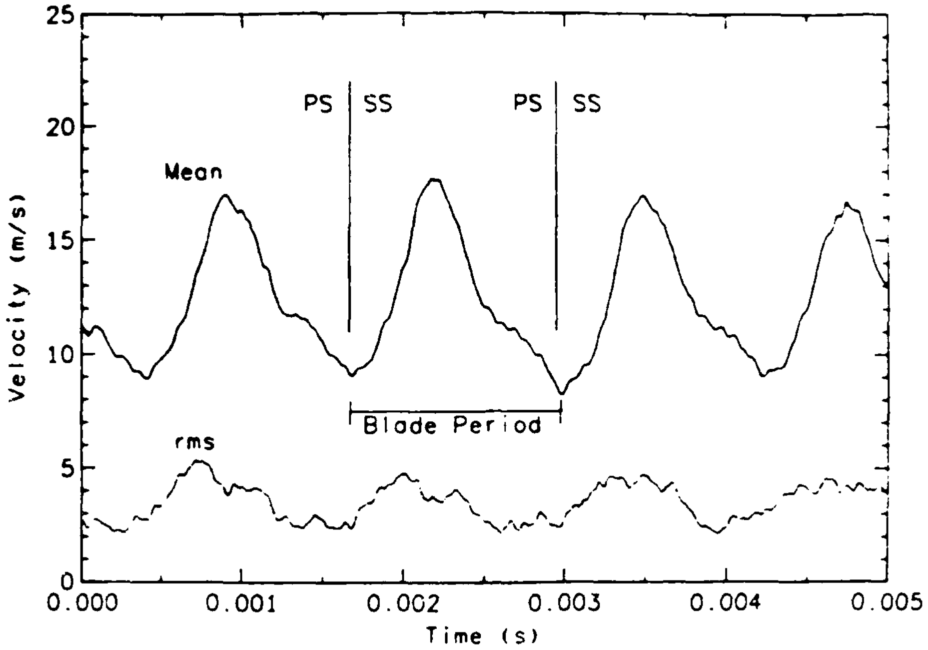

Figure 35. Mean and rms Velocity Profiles at Trailing Edge Position T1/C.

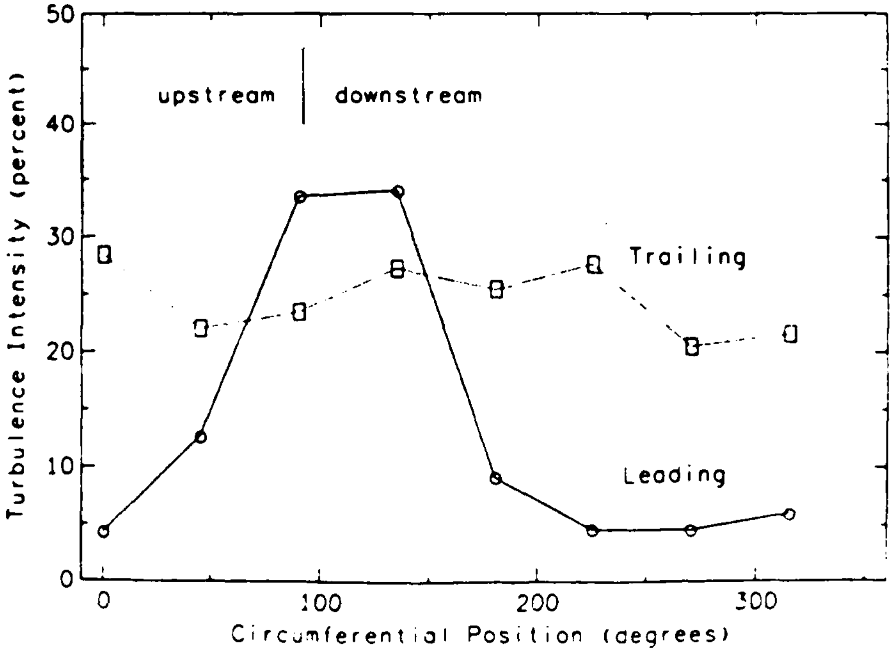

Figure 36. Turbulence Intensity Distribution Averaged Across Blade Channel.

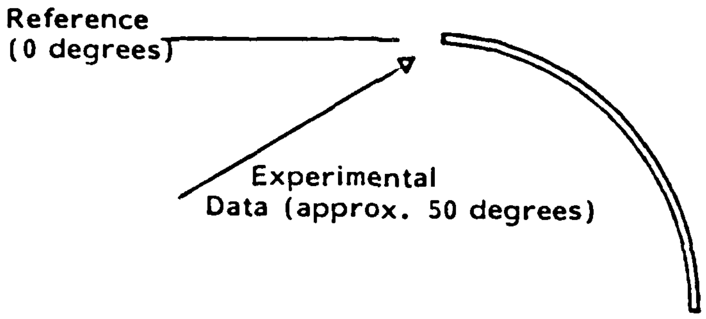

Figure 37. Schematic of Incidence Angle Computed From Measurements. Large incidence angles are normally associated with blade stall and increased noise.

Chapter 6. Single Blade Investigations

Several experiments were performed using a single blade from the model blower impeller immersed in a controlled flow field. In addition, the two-dimensional, steady flow over a single blade was modelled using a numerical fluid flow modelling program. This chapter contains the results of those efforts.

In a general sense, the broad band, random noise generated in a low Mach number centrifugal blower is due to turbulent interactions with the rotating blade row and with the stationary housing. Aerodynamic source identification within the air moving device requires knowledge of the flow field causing the turbulence, and an understanding of the relationship between the flow field and the resultant noise generation for that particular geometry and flow condition. The results of experiments aimed at understanding the details of the flow distribution in and around the blade row were presented in Chapter 5, "Aerodynamic Measurements in Model Blower." Investigations similar to these have appeared in the literature in the past.

The next logical step would involve direct measurements of the blade forces and correlations of these with the radiated noise. Several investigators have been successful at measuring the blade surface pressures in an operating impeller; however, attempts at determining the strength of the correlations between local blade aerodynamic forces and the generated acoustic noise, if any, have not been successful, or at least have not appeared in the literature. This is not at all surprising considering the complexity of the problem. Assume, for the sake of discussion, that the noise is due entirely to the fluctuating normal forces on the blade surfaces. If the overall source region on each blade surface is taken to be comprised of a collection of sub-regions, each with time histories that are statistically independent from any other sub-region, then the collection of independent sources distributed over the entire rotating blade row may be treated as a multiple input/output problem. Even if the turbulence-induced blade surface pressures are well correlated over each entire blade (which is an unlikely assumption) but independent from blade to blade, spectral analysis methods would involve measurements between signals with a noise-to-signal ratio of approximately 14 dB (for a 26-bladed impeller). This, coupled with the added difficulties of performing measurements in a rotating frame of reference, force the conclusion that it is an impossible proposition, given current experimental technologies and signal processing techniques.

The approach taken for the research reported in this thesis was to isolate a single blade in a controlled flow field under favorable acoustical conditions (i.e., non-rotating frame, and no nearby reflecting surfaces) and use the information obtained under those conditions to infer similar behavior in an operational blower. The disadvantages of using the single blade as a model of a blade in an operating, rotating impeller are:

- The primary energy transfer mechanisms in the impeller (centrifugal forces on the fluid) are not present in the model.
- Isolating a single blade in the flow field neglects the possibility of inter-blade interactions.
- An important field parameter in the rotating impeller is the local hydrodynamic pressure gradient over the blade surface. This is impossible to control in the free jet flow used for the single blade investigations.

Despite these shortcomings, the single blade analysis establishes a solid foundation for the understanding of the active noise source mechanisms. In addition, using the knowledge gained as a result of the aerodynamic measurements made on the operating blower (see Chapter 5, "Aerodynamic Measurements in Model Blower"), the flow field over the single blade immersed in a jet flow can be made to approximate realistic conditions by proper placement of the blade in the spatially varying field. Blade-to-blade interactions can be accounted for to some extent by the use of a cascade imbedded in the controlled flow. While this was not done for this project, cascade analysis represents a natural extension of the current work. Also, the analytical approach presented in Chapter 2, "Theory of Aerodynamic Noise Generation," was used for the first time in the single blade studies and will continue to be developed for future investigations of more complex geometries.

6.1 Results of FLUENT Model of Single Blade

As a first step in the investigation of the flow field near a single blade immersed turbulent flow, a numerical model of the mean flow was developed using a commercial, computational fluid dynamics (CFD) computer program, FLUENT®, available from Creare, Inc.. FLUENT is a finite-volume, elliptic solver which offers turbulent as well as laminar fluid flow models. The main advantage to the use of elliptic solution methods is that the flow field solution can take into account downstream effects. A parabolic solver, on the other hand, progressively solves the field from inlet to outlet, with downstream effects having little bearing on the overall solution.

Two turbulent models models are available with FLUENT; the two-equation, k-ε model and an algebraic stress model. The k-ε model is the simpler of the two and is based on a Boussinesq hypothesis for the turbulent viscosity as a model for the Reynolds stress terms [49]. The transport equations for turbulent kinetic energy, k, and dissipation rate, ε, are modeled, and the effective turbulent viscosity, μ_t, is given by,

$$\mu_t = \rho\ C_\mu\ k^2/\varepsilon \tag{6.1}$$

where $C_\mu = 0.09$ is a proportionality constant. The Reynolds stresses are related to the turbulent viscosity by [74],

$$-\overline{u_i u_j} = -\frac{2}{3}\, k\, \delta_{ij} + \frac{\mu_t}{\rho}\left(\frac{\partial U_i}{\partial x_j} + \frac{\partial U_j}{\partial x_i}\right). \tag{6.2}$$

The primary shortcoming of the k-ε model is the inherent assumption that the eddy viscosity is scalar; hence the Reynolds stress terms modelled by Equation (6.2) are insensitive to direction — the turbulence is locally isotropic. This assumption is particularly poor for anisotropic flow fields such as those with a high degree of swirl. For the present problem, flow over a curved surface, only gross effects of flow separation around the blade surface were required. Hence the simpler, less numerically intensive, k-ε model was used. When flow past a circular cylinder was used as a test case, the overall flow structure was not significantly affected by the choice of the turbulence model.

FLUENT (Version 2.8) solves the steady partial differential equations for fluid flow (mass, momentum, and energy) using an iterative process which starts from arbitrary initial conditions and converges to a solution of the discretized equations of motion. Since time dependence is neglected in the version used for this work, it is important to make a proper interpretation of the *steady* solutions produced by FLUENT, at the Reynolds numbers of interest, to a quasi-steady problem such as the flow past a cylinder or over an airfoil. Since the time that these models were developed, Creare, Inc. has released a version of FLUENT which incorporates time dependence into the solution (Version 2.9) by implementing a *fully implicit* time integration scheme [22, 73].

FLUENT (Version 2.8) uses a time-marching iterative approach in which the momentum equations are solved based on a "guessed" pressure. A pressure-correction equation (incorporating continuity) is then solved to obtain the pressure field corrections and, in turn, to adjust the velocity components and to solve for other field parameters. The entire process is then repeated for the next iteration, with the effects of the previous iteration factored into the solution using an *underrelaxation factor* (a default value of 0.2 is provided by FLUENT). For an unsteady problem, the iteration process indirectly corresponds to the time evolution of the flow field simply because omission of the time dependence is manifested in the residual errors or correction terms for each iteration. The relationship between a single iteration and the actual time increment is an indirect one because the solution to the flow field is controlled by the underrelaxation factor, which is independent of the flow field. Depending on the relationship between the underrelaxation factor and the unsteadiness of the physical problem, the residual errors for the problem may become quite small, and hence the problem would appear to have converged to a steady solution. While the convergence is artificial in a sense, the solution can be thought of as an approximation to the flow field at some fixed time during the evolution.

The flow over a single blade was considered as a two-dimensional problem for reasons discussed in the section on cascade analysis. A polar cylindrical coordinate system was selected since a constant radius of curvature blade profile was to be modelled. The circular domain was configured in such a way as to approximately simulate flow through a constant cross-section two-dimensional duct by defining various outer cells around the periphery as boundary cells. The duct walls were kept far enough from the modelled blade so as not to influence the local flow field around the blade. The inlet velocity boundary conditions at one end of the duct had to be specified in radial and tangential velocity components due to the coordinate system. Each inlet cell velocity was individually specified to produce an inlet velocity field containing vectors in a direction parallel with the walls of the duct. A nonuniform problem grid was defined in order to concentrate most of the solution cells near the pressure and suction surfaces of the blade. As a result, the grid structure was quite coarse near the outer boundary of the domain.

In order to test the ability of FLUENT to make a reasonable prediction of the separation point over a curved surface, a test case was used which consisted of a cylinder immersed in a turbulent flow field. The curvature of the cylinder was chosen to match that of the impeller blade to simplify the definition of the problem. That is, the blade was merely a section from the thin-walled cylinder. An inlet turbulence intensity level of 10 percent was chosen for the problem to simulate typical conditions found in the inlet of a centrifugal impeller. An inlet velocity of 10 m/s and cylinder diameter of 20 mm was specified; the Reynolds number was 1.4×10^4. The solution to this problem, which consisted of approximately 10,000 cells, required about 85 minutes of processor time on an IBM Model 3081 computer system (mainframe) before reasonable convergence was achieved. This illustrates the complexity of CFD algorithms, and the order of magnitude of processing capability required to solve a relatively simple problem (simple in the sense of requiring only a steady solution and using the less computationally intensive k-ε turbulence model). More extensive solutions, such as those requiring time dependence, would benefit from the capabilities of computers with specialized vector processing capabilities, such as an IBM Model 3090 Vector Facility.

The resulting velocity field is graphically depicted in Figure 38 on page 128. The separation point for a cylinder immersed in flow using exact solutions of the steady-state boundary layer equations is 108.8° from the stagnation point (see Chapter 9 of Schlichting [82] regarding the solutions of Blasius). The results shown in Figure 38 reasonably predict that behavior.

By redefining a section of the cylinder wall to be part of the active flow field, the desired blade shape was obtained. Results of the flow simulation over the blade oriented at an angle of 0° relative to the incident flow velocity are shown in Figure 39 on page 129. The steady flow field predicted by FLUENT is shown to separate from the suction side of the impeller blade section at a chordwise point very close to the leading edge of the blade! The separation bubble encompassed most of the blade surface. An additional counter-rotating eddy was formed at the trailing edge due to the incident pressure-side flow mixing with the recirculating leading-edge eddy. Such a flow field is not characteristic of an effective airfoil design. This was the primary result of the flow simulation. A second blade orientation was used to examine the effects of the incidence angle on the simulated flow field. Rotating the blade by 30° allowed the incidence angle to be affected. Figure 40 on page 130 shows the predicted steady flow field for a 30° incidence angle with enhanced eddy formation over the suction surface of the blade. It is clear from these simulations that, for velocities typical of those found in the model centrifugal blower, the flow over a section of the impeller blade is not well behaved. A high incidence angle was found to correspond to the formation of two counterrotating eddies in the wake. This structure is characteristic of flow past a blunt body and the formation of a periodic vortex street. When considering a rotating blade row rather than an isolated airfoil, an increased incidence angle would tend to exaggerate blade-to-blade interactions through adjacent blade-wake interference. It would be interesting to model these effects, but the current implementation of FLUENT is not suitable to a full cascade simulation.

It should be noted that since the flow solutions presented in this section were obtained by a steady solver, the results must be interpreted by considering the limitations imposed by the solution algorithm. Specifically, it is probable that the eddy structure observed near the airfoil in the above figures is indicative of the unsteady formation and shedding of discrete vortices from the suction surface of the blade (rather than the existence of a steady separation bubble), since that is characteristic of flow past a cylinder of the same curvature and Reynolds number. However, information on the unsteady properties of the flow was not available from the FLUENT program.

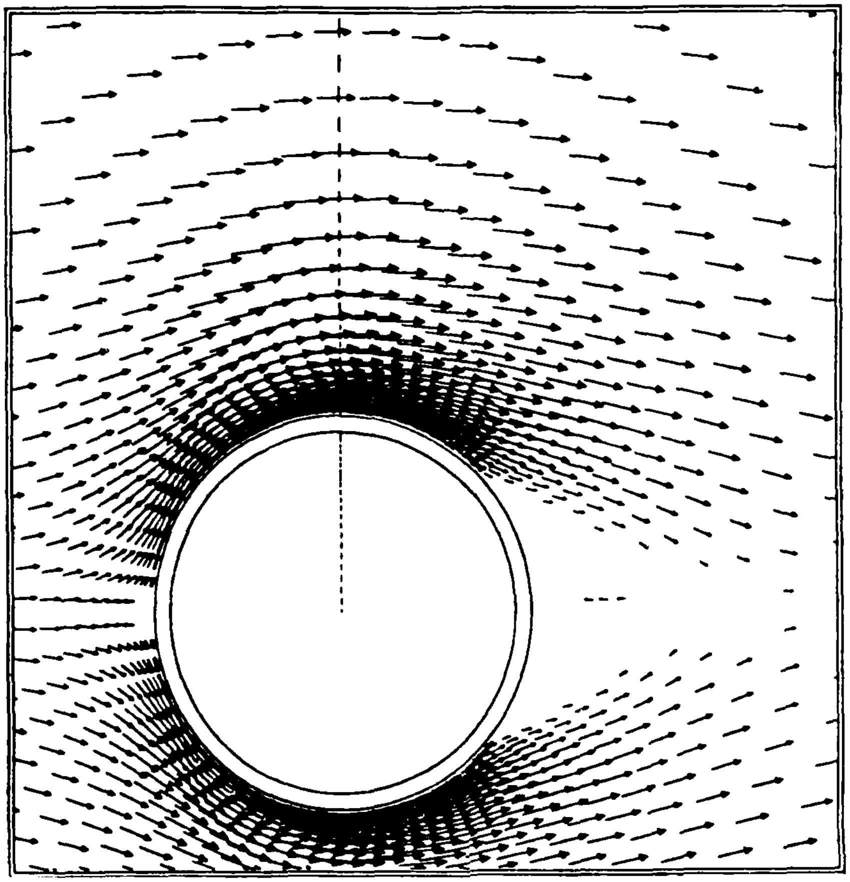

Figure 38. Simulated Flow Field Past Cylinder Using FLUENT

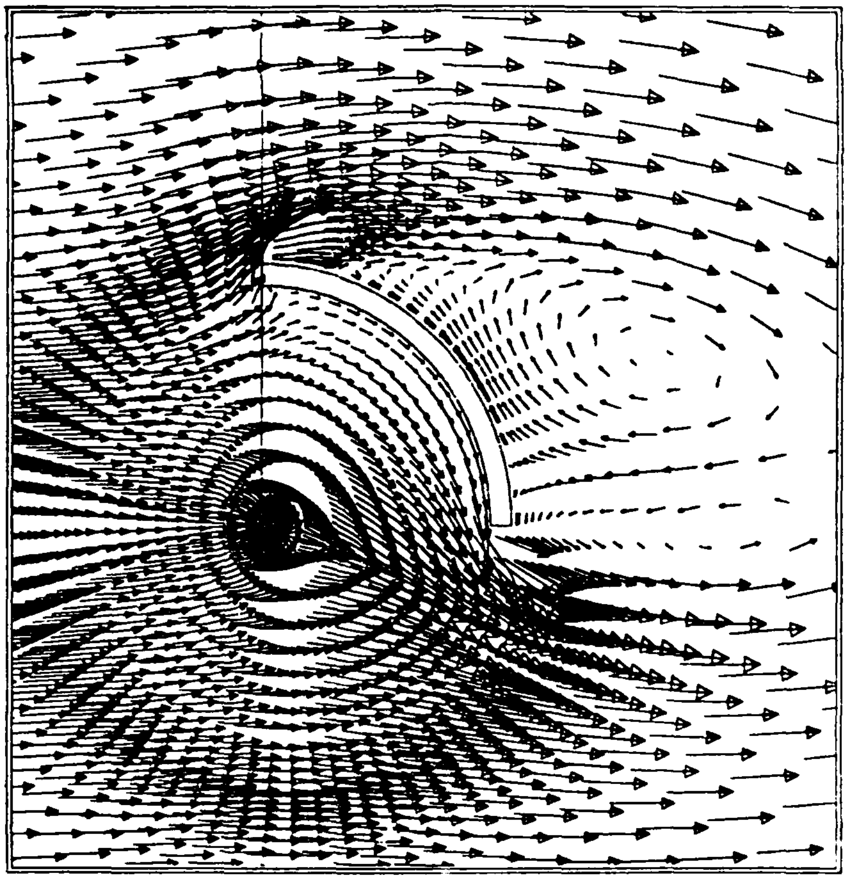

Figure 39. Simulated Flow Over Model of Impeller Blade at 0° Incidence

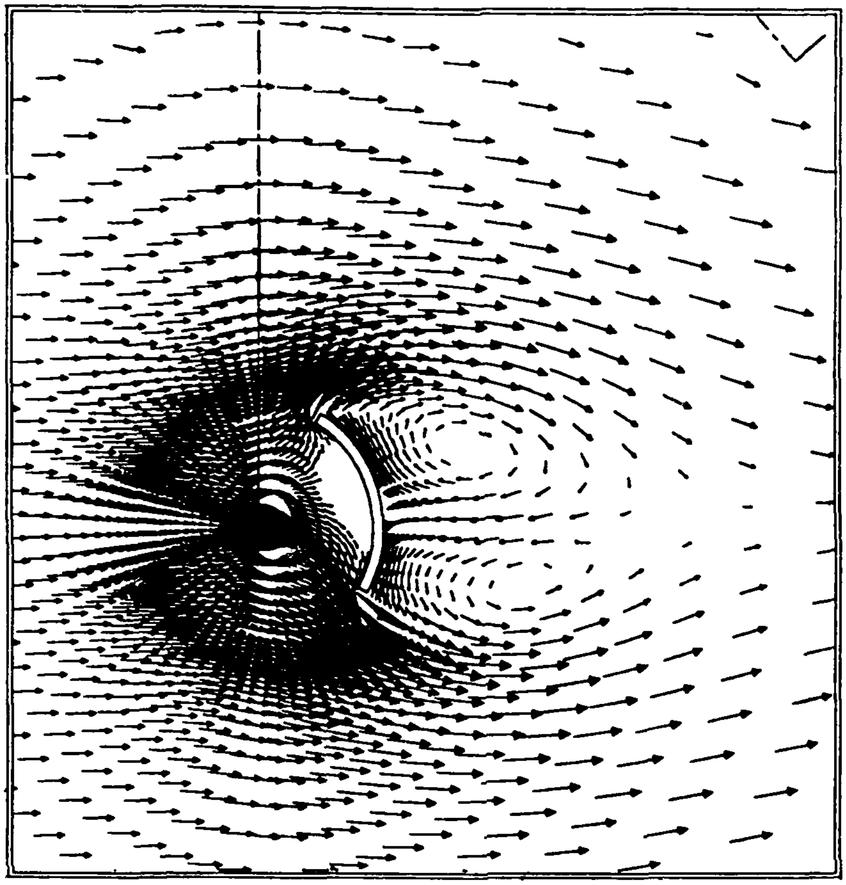

Figure 40. Simulated Flow Over Model of Impeller Blade at 30° Incidence.

6.2 Experimental Investigations Using Frequency Domain Theory

This section contains the experimental results of investigations of noise radiated from a single impeller blade immersed in a flow field of both low and high degrees of turbulence. Experiments were performed in the hemi-anechoic chamber facility using the the air flow source described in Section 3.2.5, "Quiet Air Source," and a single blade of the same blade shape as those used in the model blower impeller. The blade was immersed in the flow field at two different locations, to simulate high and low turbulence levels incident on the blade. Both aerodynamic and acoustic parameters were measured:

> **Aerodynamic** — The mean and turbulent flow distributions were measured at several points within the flow. Both total rms levels and frequency-dependent information were obtained for the turbulent field. In addition to characterization of the flow field external to the blade, measurements were made of the blade surface pressures and the associated statistical nature of the surface pressure field.
>
> **Acoustic** — Acoustic measurements included determination of the sound pressure level at various points around the blade, and measurement of the correlation between the radiated acoustic field and the local blade surface pressures. The correlation data were used to make estimates of both the correlation area over the blade surface and the distribution of the dipole source strength.

The results of the flow field characterizations external to the blade surface are presented in Section 6.2.2, "Quiet Air Source Characterization," the blade surface pressure data appears in Section 6.2.3, "Blade Surface-Pressure Statistics," and the correlations between the acoustic and aerodynamic field are given in Section

6.2.4, "Correlation Area — Sc," and Section 6.2.5, "Dipole Source Strengths — dGpp/dS." The measurement configuration for the blade surface pressure investigations and the acoustic-aerodynamic correlations will be described in the following paragraph.

All measurements of the blade surface pressure were done at the midspan position on both the pressure and suction sides of a single blade immersed in the jet flow. Single point measurements were made at three chordwise locations, referred to as the LE, MC, and TE (leading edge, midchord, and trailing edge, respectively). In addition to the single-point measurements, two-point correlations were determined in which spanwise as well as chordwise coherence was examined. The sensor locations are shown in a plan view of the blade surface in Figure 41 on page 160. Both the low-profile pressure transducers (Kulites) and the probe-tube microphones were used for the surface pressure determinations. The Kulites were imbedded in elongated slots machined into the blade surface and retained with clay. The ends of the probe-tube microphones were inserted flush through small holes drilled to fit the tube then sealed with clay from the opposite side of the blade. Chordwise measurements on the pressure side were obtained using all three Kulites mounted along the chord. The transducers were removed and replaced with opposite orientation for the suction-side data. Simultaneous measurement of the pressure- and suction-side pressure was performed with a pair of Kulites mounted back-to-back in each chordwise position. As the Kulites were difficult to remove and replace, and since only three were available, the spanwise correlations were determined using chordwise Kulites and a probe-tube microphone located consecutively, opposite each one of the Kulites along the blade span.

Aerodynamic-acoustic correlations were based on estimates of the cross-spectral density between the blade surface pressure and the radiated acoustic pressure sampled at a point removed from the flow. The far field microphone was located 0.2 m from the blade surface along a radial line from the blade center of curvature through the blade midchord position. This configuration is pictured schematically in Figure 42 on page 160, and a photograph is shown in Figure 43 on page 161.

6.2.1 Transducer Calibration

Since all of the measurements presented in this portion of the analysis were performed in the frequency domain, rather than in the time domain as in earlier work [88], the possibility existed for compensating for transducer effects using frequency domain calibration techniques which have become an integral part of modern experimental methodology. With digital FFT signal analysis techniques the complex frequency response of transducers can normally be measured with a high degree of precision. Transducer effects may be removed from a frequency domain measurement through complex normalization of the result by the previously measured transfer functions of the transducers used for the measurement. The calibration process is even further simplified when post-processing capabilities are an integral part of the instrumentation, in which case calibration can be performed automatically during the measurement or after the measurement has been completed.

Digital, frequency domain calibration techniques have brought about two primary changes in modern experimental methods. First, extremely high measurement accuracy is achievable with commonplace instrumentation. The most obvious example of a measurement method that has benefitted from this is the use of the finite-difference technique for estimating acoustic intensity. Experimental verification of complex intensity patterns were difficult at best until the advent of digital FFT-based calibration procedures and associated instrumentation which allow laboratory calibration of measurements that can be influenced by extremely small transducer anomalies. The second effect of digital calibration on experimental methods is the ability to select from a much wider range of sensor types since the particular sensor response can be "calibrated out" rather easily. Physical or environmental constraints for a particular experiment can often be overcome most effectively by compromising transducer performance in return for miniaturization or durability. This compromise is not possible (with currently available instrumentation) when limited to time-domain analysis as it is much more difficult to compensate for sensor anomalies in the time domain.

It is the latter effect which has enabled the use of microphones fitted with small probe-tube adapters for the measurement of blade surface pressures. Probe tubes have several advantages over conventional miniature pressure sensors but have found little use in acoustical measurements due to the inherently poor frequency response characteristics resulting from acoustical transmission line effects of the tube extension. However, probe-tube calibration transfer functions were measured and successfully used to compensate for the influence of the tubes. The primary motivation for using probe-tube microphones was to take advantage of the exceptional dynamic characteristics of condenser microphones — uniform frequency response, wide dynamic range, and high sensitivity.

Not all experimental determinations of the blade pressure statistics were amenable to the use of probe tubes. Specifically, due to the physical interference of the probe tubes with the flow field, simultaneous measurement of the pressure- and suction-side blade surface pressure at the same chordwise location required the use of miniature, low-profile pressure transducers manufactured by Kulite Semiconductors (see Section 3.3.2, "Instrumentation," for transducer specifications).

In general, transducer effects are characterized by the complex frequency response H. If the *desired* signal for channel i, $u_i(t)$ passes through a transducer to produce the *measured* signal u_i, then the autospectral density of the measured signal $G_{x_ix_i}$ is related to the desired autospectral density $G_{u_iu_i}$ through the transducer response:

$$G_{x_ix_i} = X_i^* X_i = |X_i|^2 = |H_i|^2 \, G_{u_iu_i}. \tag{6.3}$$

Using the same notation, the cross-spectral density between two measured signals is,

$$G_{x_ix_j} = X_i^* X_j = = H_i^* H_j \; G_{u_iu_j} \,. \tag{6.4}$$

where $G_{u_iu_j}$ is the desired cross-spectral density. Knowledge of the transducer frequency response functions H allows the desired result to be obtained from the measured result by straightforward frequency-domain operations.

For most of the measurement results presented, the desired quantity was the acoustic and/or hydrodynamic pressure, and the measured quantity was typically the electrical analog of the pressure. Since the response of transducer i relative to the reference transducer ($H_{ir} = H_r H_i^{-1}$) is a quantity that can be readily measured, then the cross-spectral density of the pressure between two points p_1 and p_2 is given by

$$G_{p_1p_2} = \frac{G_{x_1x_2}}{H_1^* H_2} = G_{x_1x_2} \frac{H_{1r}^* H_{2r}}{|H_r|^2} \,. \tag{6.5}$$

Equation (6.5) represents the calibration relationship used for the data presented in this section. A Bruel and Kjaer 12.7-mm diameter microphone Type 4165 was used as the reference transducer. The amplitude of H_r was compensated for using a pistonphone calibrator operating at 250 Hz. It was assumed that the *amplitude* response of the reference microphone was uniform for the frequency range of interest, thus the denominator of Equation (6.5) is assumed to be unity. The *phase* response of the reference microphone however does *not* have an effect on the computed cross spectrum $G_{p_1p_2}$ since it is an inherent part of the measured calibration transfer functions H_{ir} and since the phase of the reference transducer response H_r cancels out in the numerator of

Equation (6.5). The next two sections contain descriptive information on the procedures used to measure the transducer response functions.

6.2.1.1 Probe-Tube Calibration

Calibration of the 12.7-mm diameter microphones fitted with probe tubes was performed with the use of a closed air cavity excited by a small earphone (see Figure 44 on page 162).[15] A reference microphone and the probe-tube microphone were simultaneously attached to the small cavity and thus exposed to the same uniform sound field inside the cavity. The earphone was driven by a broad band random noise source over a frequency bandwidth of 3.2 kHz using the internal source from the Hewlett Packard HP5420 FFT Analyzer.

Calibration transfer functions for each probe-tube microphone were obtained relative to the response of the reference microphone over the frequency range of interest. A frequency-independent calibration factor, obtained from a single-frequency pistonphone attached to the reference microphone, was then applied to the transfer functions to compensate for the microphone sensitivity. The resulting calibration transfer function was a measure of the relative response between the reference microphone and the probe-tube microphone.

Two probe tubes were used and fitted to three different microphones to determine the combinations with the best amplitude and phase response. The probes were constructed from 2-mm diameter tubes provided with the probe kit and were cut to an overall length of approximately 70 mm, including the conical microphone adapter. Acoustical resonances in the tubes can be minimized using damping material such as

---

[15] The probe tube calibration apparatus was a part of the Bruel and Kjaer Probe Microphone Kit Type UA 0040.

loosely packed fibers or fine steel wool, but no such material was used for these experiments as the effects would have been difficult to control over time, especially since the tubes were to be immersed in an air stream.

Transfer functions between the reference microphone and each of four probe-tube microphone combinations are compared in Figure 45 on page 163. Three of the combinations were well matched, and the fourth was quite different. Notice that the probe, when attached to different microphones, behaves differently. This is due to the source impedance of the microphones interacting with the acoustic transmission line effects of the probe. For this reason the procedure of calibrating the microphones and probe tubes independently could *not* be used, and the complete probe-tube microphone assembly had to calibrated for each combination. The calibration transfer functions were found to be repeatable within a few degrees and a fraction of a decibel over the entire frequency band.

In order to verify that the source impedance interaction would not affect the free field response of the probe tubes, a pair of probe tubes were calibrated using a free-field switching method in the hemi-anechoic chamber. The free-field method involved exposing the probe-tube microphones to a *similar* sound field produced by a loudspeaker suspended above the reflecting plane of the chamber, measuring the transfer function between the sensors, then interchanging the microphones in space so that they were exposed to the sound field previously incident on the opposite microphone. Manipulating the two transfer functions measured under these conditions allows the relative response of the sensors to be determined as though they had been exposed to identical signals (i.e., the differences in the pressure fields at the two microphones cancel). Results of the free-field experiments are shown in Figure 46 on page 164 where the *worst* probe-tube microphone combination was used as one of the sensors so as to exaggerate any differences in the two methods. The excellent agreement confirms that the coupler calibration method is accurate and that the differences between the coupler response and free-field response of the probe-tube microphones were negligible.

6.2.1.2 Kulite Pressure Transducer Calibration

The Kulite pressure transducers were calibrated with the same coupler used for calibration of the probe-tube microphones. Up to three Kulites could be inserted into the cavity at one time. The opening in the coupler wall normally used for a probe tube was just large enough to accommodate the flat cable from the Kulites. Clay was used to seal the opening during measurements.

Due to the low sensitivity of the pressure sensors, extreme care was taken to minimize the noise floor of the Kulites. Batteries were used as the power supply to reduce the effects of line frequency noise. Other researchers have devised special circuits for these transducers to eliminate common mode noise associated with electromagnetic interference or other stray noise sources. For the current project the outputs of the transducers were fed directly into high quality laboratory amplifiers with a gain of 70 dB using a short section of coaxial shielded cable. For most of the measurements this was sufficient, however extraneous noise did become a factor in some cases.

The minimum effective sound pressure level measurable by the Kulites is shown in Figure 47 on page 165 along with the sound pressure level of the noise produced inside the coupler for the calibration transfer function measurements. The pressures levels have been normalized to a 1 Hz bandwidth (i.e., spectral density). The third data set in Figure 47 was taken with the earspeaker output attenuated by placing clay over the outlet port of the speaker. The purpose of this experiment was to verify that the output of the transducer was indeed due to the acoustic field and not the result of an induced voltage from the electromagnetic field of the earphone, as was the case when the wire leading to the earphone speaker was within a few millimeters of the Kulite output cables.

The sound pressure level inside the coupler as measured by the reference microphone deviates from the Kulite response for frequencies above 2 kHz. This deviation is indicative of the relative frequency response of the Kulites and was responsible for the nonuniform calibration transfer functions measured between the reference microphone and the Kulites.

The ordinary coherence function is a measure of the input/output relationship between the two signals, and was used to monitor the integrity of the calibration signals. The extreme sensitivity of the Kulites to extraneous noise is demonstrated in Figure 48 which shows the effect of the overhead fluorescent lights on the coherence between the Kulite and the reference condenser microphone. The ordinary coherence function is especially sensitive to noise introduced into one channel only. The measurement was taken with the reference Bruel and Kjaer microphone as one of the measurement channels, hence the electromagnetic noise was induced in only one of the channels (that is, the channel with the Kulite transducer). The lights were subsequently powered off for all measurements involving the Kulites. The lighting system in the hemi-anechoic chamber is incandescent and did not affect the Kulite output. Experience with the Kulites has shown them to be especially sensitive to electromagnetic interference and input power supply noise. Efforts to reduce the noise floor by shielding were only marginally successful.

The relative response between the Kulites and the reference microphone was quite uniform up to about 2 kHz where the decrease in sensitivity to high frequencies by the Kulites became evident (see Figure 49 on page 166). This response pattern was also indicated in Figure 47. All Kulites measured were found to have incorrect polarity.[16] This was easily corrected by interchanging the output leads relative to the factory specification. The Kulites were quite well matched in both amplitude and phase, as shown in Figure 50.

Initially, Kulite calibration was attempted by flush mounting the Kulites and the reference microphone to a termination plate at the end of an impedance tube. The resulting transfer functions showed evidence of the longitudinal resonances of the duct[17] and, despite efforts to damp the resonances using glass fiber, the measured curves were not nearly as smooth as those obtained using the probe tube coupler. The impedance-tube method was abandoned.

In summary, microphones were fitted with probe tubes and successfully calibrated using a small closed cavity and a reference microphone. Results were repeatable and found to be in close agreement with, and smoother than, those obtained using a free-field method. Miniature, low-profile pressure sensors (Kulites) were also calibrated in a coupler using the transfer function method. The low sensitivity and inherent noise of the Kulites limited their application to high turbulence regions. Probe tubes were used where physically feasible and where low turbulence levels existed. Efforts to reduce electromagnetically induced noise in the Kulites were only marginally successful.

6.2.2 Quiet Air Source Characterization

The jet flow field produced by the quiet air source, described in Section 3.2.5, "Quiet Air Source," was quantified by determination of the mean and fluctuating velocities using a single-element hot film sensor. Since the length-to-width ratio of the

---

[16] This problem was verified using acoustic pressure pulses with known polarity (e.g., a clap or bursting balloon).

[17] The *small* Bruel and Kjaer impedance tube was used.

exit orifice was approximately 5:1, the hot film sensor was aligned parallel to the longer dimension of the orifice so as to be sensitive to the velocity components which lie in the plane perpendicular to the longer dimension of the exit orifice. Measurements were performed at points in the flow which corresponded to the location of the leading edge, midchord, and trailing edge of the single blade when the blade was immersed in the flow, but measurements were made with the blade removed from the flow. The three streamwise locations were taken at the mid span of the blade width. The mean and total rms velocity levels were determined using a digital oscilloscope and associated software.[18]

Two blade locations, termed the *core* and *mixing* regions, were used for the experiments described in this section. These terms refer to the locations of the leading edge of the blade relative to the center of the 23 mm x 110 mm exit orifice, with the blade oriented at a 0° incidence angle. For the core measurements, the blade was centered over the exit orifice at a height of 20 mm above the duct edge. The mixing region location corresponded to placement of the leading edge of the blade vertically aligned with the back edge of the exit orifice (with the blade curvature away from the core region) at a height of 55 mm above the duct exit. A schematic of the blade positions and measurement locations is given in Figure 51 on page 168.

The blade was attached to the end of a steel support rod and clay was used to produce a smooth transition from the blade surface to the rod cross section. The opposite end of the cantilevered blade was attached to a small, stiff wire secured to the air supply which was used primarily as a spatial reference point. The blade was cemented to the support wire to reduce vibration levels.

A summary of the corresponding mean and rms velocity levels is given in Table 3. Additional information is contained in the frequency distribution of the tur-

---

[18] The velocity computation procedure is discussed in Section 3.3.2, "Instrumentation."

bulent energy. Since the radiated noise is a direct result of the turbulent interactions of the flow with the blade surface, the incident turbulent energy distribution is of fundamental importance to understanding the noise source mechanisms. For the purposes of determining the spectrum of the velocity fluctuations, the hot film sensor output was analyzed using the Hewlett Packard HP5420 FFT Analyzer. The results are shown in Figures 52, 53, and 54, beginning on page 169. Several aspects of the turbulence are apparent from these data. First, the decay of the turbulence with distance from the jet exit is evident for both the core and mixing regions. This would imply that the turbulent energy incident on the blade from the free stream is strongest at the leading edge, and possibly the midchord for the mixing region. There is no information here however on the blade-generated turbulence (e.g., separation) since these measurements were made without the blade present in the flow field.

Table 3. Velocity Distribution in Jet without Blade Present

	Mixing Region		Core Region	
Location	**Mean (m/s)**	**Turbulent TI(%)**	**Mean (m/s)**	**Turbulent TI(%)**
Leading	7	30	14	5
Midchord	4	40	14	2
Trailing	1	70	14	2

The second feature of the flow is that in the core region a *dominant frequency* is apparent in the frequency range from 400-800 Hz. This particular characteristic is likely to be due to the irregular internal structure of the flow duct; the result of large scale vortex shedding and stretching at the jet exit. Regular vortex patterns typically form in the wake of structures over a wide range of Reynolds numbers up to about 3×10^5 for a constant Strouhal number ($S = fD/U$) of about 0.2.[19] For a maximum jet velocity of 15 m/s, the characteristic dimension of the interfering structure is of the

---

[19] See, for example, Schlichting [82] for a general review.

order of 5 mm. While the internal duct discontinuities are considerably larger than 5 mm, any internally shed vortices would be contracted and stretched before exiting the conical transition section of the duct, thereby decreasing the time scale of the eddies (conservation of angular momentum). This concept of energy redistribution through vortex stretching is discussed by Tennekes and Lumley [91] and is shown to be an integral part of the energy cascade process by which large scale eddies transfer energy to smaller scales for eventual viscous dissipation. The decay of the dominant frequency effects may be seen in Figure 53 where the eddies appear to decay in strength and in the characteristic time scale with distance from the jet exit.

In addition to the above measurements, which were performed with the blade removed from the flow, several points in the flow were sampled with the blade present in order to characterize the blade wake region. The velocity spectral densities are shown in Figures 55 and 56, and the mean and rms velocity levels are shown in Figures 57 and 58. A characteristic blade wake structure is evidenced by the mean distribution in the mixing region. Core region data demonstrates a uniformly low velocity field, mainly due to the obstruction of the blade in a laminar flow. The large scale turbulence present in the mixing region prevents the formation of a large velocity deficit directly behind the blade, thus creating a much narrower wake structure. The turbulence spectra are uniformly decreasing with frequency.

6.2.3 Blade Surface-Pressure Statistics

As discussed in Section 2.2, "Frequency Domain Analysis," the fluctuating blade surface pressure is closely related to the noise generation process over the blade surface. In fact, some investigators have taken the surface pressure to be a direct measure of the surface dipole source strength by assuming negligible effects of complex surface pressure interactions and measuring the surface pressure independent of the radiated acoustic pressure [77, 78]. The blade surface pressure is quantified in this section. Inferences are made relative to the structure of the incident flow field and the resulting effects on the surface pressure from point pressure measurements and two-point correlations.

The primary quantity used for examining the pressure correlations is the *complex* coherence between two points on the blade surface,[20] γ_{12}, which is defined as [13],

$$\gamma_{12} = \frac{G_{12}}{(G_{11}\, G_{22})^{1/2}} . \tag{6.6}$$

The phase of the complex coherence is the same as for the cross spectrum, and the magnitude is just the square root of the ordinary coherence, γ_{12}^2, which is given by

$$\gamma_{12}^2 = \frac{|G_{12}|^2}{G_{11}\, G_{22}} . \tag{6.7}$$

The chordwise distribution of the blade surface pressure for both the suction and pressure surfaces for the blade immersed in the mixing region of the flow is shown in Figures 59 and 60 on page 173. (Low turbulence levels at the trailing edge limited measurements to the frequency range below 1 kHz.) A comparison of the pressure data for the suction surface (Figure 59) and the velocity measurements made in the mixing region (Figure 54 on page 170) indicates that the suction side pressure reflects

---

[20] The complex coherence is sometimes referred to as the *normalized cross spectrum*[17] , but this terminology is misleading since the spectral shape of the cross spectrum is generally quite different from that of the complex coherence.

the fundamental features of the *external* velocity field. The leading edge and midchord regions exhibit similar spectral shapes and intensities with decreasing levels at the trailing edge. This is an indication that the suction-side surface pressure was dominated by the incident flow field and not by the local boundary layer formation. Conversely, the pressure-side surface pressures are more uniform along the chord indicating little change from leading to trailing locations. The effects of low transducer sensitivity are evident in these data. The spikes beginning at 300 Hz represent odd harmonics of the line frequency beginning at the fifth harmonic.

The convective eddy structure plays an important role in the generation of noise. As large and small scale eddies are convected past a fixed point the eddy structure may change due to the transient nature of turbulence. A measure of this time dependence may be obtained in the frequency domain from an estimate of the coherence function. The coherence function between two points aligned in the streamwise direction provides qualitative information on the decay or growth of eddies. A high value of the coherence function indicates the transport of a coherent structure that remains essentially unchanged as it is convected past the two streamwise points. Hence information regarding eddy decay is manifested in the streamwise coherence function. Similarly, the coherence between two spanwise points provides some measure of the physical size or length scale of the eddies since an eddy is presumably passing both points at the same time [17].

The magnitude of the complex coherence between two streamwise points spaced 6 mm apart for both the pressure and suction sides is given in Figures 61 and 62 on page 174, respectively. The corresponding spanwise coherence data for a spanwise spacing of 5 mm are presented in Figures 63 and 64 on page 175. The most noticeable feature of these data is the decreasing coherence with increasing frequency. The spanwise data imply that the large eddies are those whose time scale is the largest (i.e., low frequency), and the high streamwise coherence for these low frequencies indicates a slowly decaying eddy structure. In addition, increased low frequency coherence found in the spanwise coherence at the trailing edge of the suction surface (Figure 64) is typical of trailing edge vortex formation where the separation point is uniform in the cross-stream direction [16]. On the pressure side the spanwise coherence is significantly higher at the *leading* edge. This would imply that the large scale eddies in the mixing layer are oriented in a way which enhances separation at the leading edge — edge scatter effects. The pressure side also shows reduces trailing edge coherence and enhanced leading edge coherence. This is indicative of incident free stream turbulence effects.

The complex coherence in the streamwise direction was also measured on the suction side for various angles of incidence of the flow on the leading edge of the blade. The data, shown in Figure 65 on page 176, demonstrate the effects of local flow patterns which are affected by the angle of attack. For flow incident from angles greater than 0° the enhanced coherence at low frequencies may be interpreted as an increased separation region over the suction blade surface due to the incident angle which would cause large scale eddy formation. Conversely, for angles of incidence less than 0° the flow over the suction surface is more uniform and the streamwise coherence is primarily due to the incident free-stream turbulence.

The phase of the complex coherence function, or the cross spectrum, between two streamwise points is related to the convection velocity of the eddies by the expression [21]

$$\theta_{12} = \frac{\omega \xi}{U_c} \tag{6.8}$$

where the streamwise separation distance is ξ and the convection velocity is U_c. In general, the convection velocity may or may not be a function of frequency. The phase of the cross spectrum (streamwise) for a constant separation distance is shown in Figure 66 on page 177 and Figure 67, for the pressure and suction surface, respectively. The phase data suggest that two different frequency regions exist for both the pressure and suction side — both frequency regions exhibiting a nearly linear dependence of convection velocity on frequency, but each with a characteristic convection velocity.[21] The division between these low and high frequency regions occurs at the same frequency for both the suction and pressure side of the blade (approximately 750 Hz), but characteristic velocities are quite different for the regions. It is interesting to note that it is at about the same frequency that the *magnitude* of the coherence becomes negligibly small, but the regularity in the *phase* would imply that some correlation still exists over the entire frequency range. It should also be noted that while the phase data indicates inordinately high values of U_c (e.g., $U_c \sim 10$ m/s and the free-stream velocity was measured at the leading edge position without the blade present as 7 m/s), several factors must be accounted for, such as, the accuracy of the anemometer linearizers for turbulence levels of the order of 40 percent of the mean flow, the direction of the convection velocity relative to the free-stream flow, and the effect on the flow field of the presence of the blade.

6.2.4 Correlation Area — Sc

The concept of a *correlation area* S_c was discussed in Section 2.2, "Frequency Domain Analysis." Results will be presented in this section of estimates of the *frequency-dependent* correlation area at the leading edge, midchord, and trailing edge positions on the suction surface of the single blade immersed in flow which is incident at an angle of 0°.

---

[21] Linear phase implies a convection velocity which is **independent** of frequency.

Since estimates of the dipole source strength and correlation area were based on the cross spectrum between the blade surface pressure and the acoustic pressure in the far field, it was important to identify the frequency range over which the noise due to the presence of the blade in the flow was dominant. Figure 68 shows the sound pressure level measured in the hemi-anechoic chamber at the same microphone position used for the correlation area and source strength determinations (i.e., 200 mm from the blade along the radial midchord line). These data indicate a sufficient signal to noise ratio for all frequencies above 200 Hz, regardless of whether the blade was located in the core or mixing layer regions. The low frequency noise was due to the air supply blower that was installed under the raised floor of the hemi-anechoic chamber Thus, low frequency measurements were limited to approximately 150 Hz.

The spectral *hump* (280 Hz) that occurs in the noise from the blade in the core region was initially thought to be due to a dominant frequency in the inlet turbulence spectrum. However, the characteristic frequency of the inlet turbulence was at a much higher frequency (approximately 750 Hz) as shown in Figure 52. The 280-Hz peak in the "core" spectrum corresponds to a Strouhal effect due to the periodic wake structure of the blade immersed in a laminar flow. The frequency of 280 Hz implies that for a constant Strouhal number of 0.2, the characteristic dimension of the obstructing object is 10.7 mm.[22] This dimension is roughly that of the blade as *seen* by the incident flow.[23] The resulting periodic interactions influence the broad band noise generation

---

[22] The constant of $S = 0.2$ holds over a wide range of Reynolds numbers. The Reynolds number here was estimated as 10^4 which is in the range where the Strouhal number of 0.2 corresponds to a periodic wake structure (Karman vortex street) [82].

[23] The characteristic dimension of the blade in this case is the effective width of the obstruction in the flow. For the blade orientation of 0° relative to the incident flow, the effective width, or projection of the blade chord, is 11 mm.

and produce a narrow band effect. In most of the data reported in this thesis, the measurements were performed with the blade located in the mixing region. Not only was the signal-to-noise ratio much better, but the Strouhal effects were minimized by effectively increasing the incident turbulence level.

The spatial variation of the mean square pressure in the acoustic field was examined to verify that a) the cosine directivity factor could be ignored over the range of angular locations of the microphone relative to the blade surface, and b) the acoustic pressure field was relatively uniform and did not exhibit any indications of standing waves or reflections from objects in the hemi-anechoic environment. Samples taken at two angular positions corresponding to $\theta = 0°$ and $\theta = 30°$ are shown in Figure 69. The measured sound pressure level variation reasonably approximates the $\cos^2\theta$ directivity nature of the dipole sources (i.e., $20 \times \log[\cos 30] = -1.2$ dB) for frequencies above 100 Hz. Below that frequency the influence of high background noise can be seen.

Determination of the correlation area was performed with the blade immersed in the mixing region of the flow field. From a practical viewpoint, the correlation area represents the region over the rigid surface in which the eddies are well correlated. This area is only partially related to the correlation length scales of the eddies since S_c is derived from the the cross spectrum between the surface pressure and the radiated acoustic field pressure and not from a measure of the turbulent velocities.[24] Hence, the correlation area contains information regarding the local acoustical source interactions and interferences. A large correlation area corresponds to a point on the surface that is well correlated with the surrounding turbulent sources, and is in some sense efficiently radiating (or absorbing) acoustical energy. This distinction between the corre-

---

[24] A complete discussion of the dipole source strength and correlation area, as defined by Equations (2.59) and (2.61), is given in Section 2.2, "Frequency Domain Analysis."

lation area and turbulent length scales, which are normally measured using velocity correlations, is similar to an underlying point made by Siddon [88]. He noted that pressure-deduced length scales are approximately 60 percent of the velocity length scales due to the variation of pressure in turbulence with the square of the velocity.

The correlation area was estimated using Equation (2.61) which is based on the *real* part of the complex correlation area. The measurement configuration is shown in Figures 42 and 43 beginning on page 160. The measured cross spectrum between the blade surface pressure taken at the leading edge, and the radiated acoustic pressure is shown in Figure 70 on page 179. The nearly linear phase shift, characteristic of the propagation time delay for 200 mm, indicates that the local surface pressure and resultant acoustic pressure are in phase. Also, the phase of the cross spectrum is a more sensitive indicator of the validity of the cross-spectral estimation than the coherence function, so a deterministic phase such as that shown in Figure 70 indicates a causal relationship between the surface pressure and radiated acoustic pressure.

The correlation area was estimated from measurements taken at the leading and trailing edges, and at the midchord location, all on the suction side of the blade using the Kulite transducers. The results of these measurements are shown in Figure 71 on page 180. Measurements made at the trailing edge suffered from a poor signal to noise ratio, and thus only the valid frequency range is shown. Recall that for complete coherence over the entire blade surface, the correlation area is equivalent to the blade surface area, S_a. This represents the maximum noise radiation condition for a given surface pressure autospectrum. Therefore, the correlation area shown in Figure 71 was normalized to the blade surface area, S_a. The portion of the single blade immersed in the flow field was approximately 100 mm × 18 mm (span × chord) for a total wetted surface area (including both pressure and suction surfaces) of 3.6×10^{-3} m^2.

The results indicated by the correlation area estimates imply an increasingly large correlation area at the trailing edge for decreasing frequency. This is consistent with the notion established in Section 6.2.3, "Blade Surface-Pressure Statistics," that the large eddies correspond to those with the longer time scales (low frequency). It should be kept in mind that the correlation area is related to the *efficiency of radiation* and not necessarily a direct measure of the strength of the radiating noise source. The latter is better estimated by examining the source strength per unit area, the theory of which is discussed in Section 2.2.1, "Dipole Source Strength — dGpp/dS," and the experimental results presented in Section 6.2.5, "Dipole Source Strengths — dGpp/dS."

The correlation area was also estimated using probe-tube microphones to measure the surface pressure. These devices are significantly more sensitive and thus were useful when making measurements in regions with low turbulence (e.g., trailing edge surface pressure). The results of the probe tube measurements are shown in Figure 72 on page 180 where the data over the entire frequency range has been included. Similar trends are demonstrated by both sets of data, and differences are attributed to a slightly different spatial location (in the flow field) which was chosen for Figure 72.

In general, the data of both Figures 71 and 72 indicate that the noise radiated from the blade surface is reasonably well correlated over as much as 50 percent of the blade surface near the trailing edge. The radiation enhancement shown for the trailing edge could be due to a large separation region covering the area between the midchord and trailing edge locations, similar to the phenomena demonstrated by the numerical fluid flow model discussed in Section 6.1, "Results of FLUENT Model of Single Blade." Separation from the blade suction surface would have two-dimensional tendencies where the separation point would occur at about the same distance from the leading edge, along most of the blade span. This behavior would also explain the increased spanwise coherence of the surface pressures measured at the trailing edge as shown in Figure 64 on page 175. The regions of low correlation correspond to high frequencies, where the scale of the turbulence gets progressively smaller.

Negative correlation areas were measured at the leading edge of the blade. The existence of negative values for the correlation area may be explained by considering the alternate form for the radiated acoustic pressure given by Equation (2.41) in which the total mean square pressure consists of the surface integral of the product of the mean square surface pressure and the correlation area. This formulation highlights the fact that correlation area is related more to the radiation efficiency at a point than to the concept of an area. For a complex source distribution, some regions act as *sources* and some as *sinks* of acoustical energy. Sinks are characterized as regions which absorb acoustical energy and thus contribute *in a negative manner* to the radiated acoustical power. Hence, negative values of the correlation area correspond to destructively interfering source regions at the blade surface, or sinks. It is plausible that the frequency ranges with negative correlation areas indicate and interaction of that area with other source regions in such a way as to destructively interfere with the noise generation process.

6.2.5 Dipole Source Strengths — dGpp/dS

Determination of the dipole source strength per unit area, dG_{pp}/dS, is achieved from an estimate of the cross spectrum between the surface pressure at a point on the blade surface, and the far field acoustic pressure. Since the cross spectrum is a complex quantity, the full expression for dG_{pp}/dS is complex. The real part corresponds to the actual contribution of the dipole sources to the mean square acoustic pressure; as discussed in Section 2.2.5, "Multiple Input/Output Analysis," the negative terms have similar meaning to those of correlation area; that is, destructive interference between source regions. The experimental results presented in this section were obtained by calculating the source strength per unit area from Equation (2.59), which represents the real part of dG_{pp}/dS.

The geometry of the measurement setup is shown in Figure 42. As discussed above, the approximation $\cos\theta \sim \pm 1$ was used; the sign dependent on whether pressure- or suction-side surface pressures were measured. The blade was located in the mixing region of the flow for three reasons: 1) increased blade noise thereby minimizing the influence of ambient noise due to the air supply apparatus, 2) to avoid Strouhal effects present in the core region (see Figure 68 and related discussion), and 3) increased blade surface pressures (due to turbulence) thereby improving the signal/noise for use with the (insensitive) miniature pressure transducers (Kulites).

The dipole source strength per unit area was estimated at three streamwise locations (LE, MC, and TE) and, for some estimates, on both the pressure and suction sides of the blade. Figure 73 on page 181 shows an estimate of the dipole source strength based on measurements taken at the leading edge of the blade for flow incident at 0°. The ordinate is displayed in linear units to preserve the information contained in the sign of dG_{pp}/dS. Several conclusions regarding the leading edge noise may be drawn based on Figure 73. First, the spectral distributions of the pressure- and suction-side source strengths are quite similar. Both are primarily limited to the frequency range below 1 kHz with most of the energy concentrated in the 200-450 Hz band. The spectral distribution of the noise sources at the leading edge was similar to those at other locations on the blade surface. The general trend of source strength uniformity over the surface is consistent with data presented earlier in the thesis, and is best explained by considering that a spatially uniform coherence level existed over most of the blade chord implying a fairly uniform source distribution. In addition, rather large, low frequency correlation areas were also measured which indicates a large eddy scale. There are some differences however which are especially noticeable in the frequency range below 300 Hz where the pressure side source strength at the leading edge is dominant.

The dipole source strength per unit area was also determined for the blade located at a slightly different position in the flow, but using probe-tube microphones rather than the miniature pressure sensors. The results of these measurements are shown in Figure 74 on page 182. Here the dominant source regions are clearly located near the trailing edge of the blade, over most of the low frequency range. A small amount of noise generation occurred at the leading edge in the range above 1 kHz. This was likely due to the incident turbulence interacting with the finite-thickness leading edge.

Two different methods may be used to estimate the dipole source strength per unit area, depending on the information available. The **direct** method utilizes the cross spectrum between the surface pressure and the radiated acoustic pressure. Another estimator for the dipole source strength per unit area may be obtained from Equation (2.41) in which the product of the surface pressure and correlation area is proportional to dG_{pp}/dS. As a practical matter, the cross spectral terms are often not available or difficult to measure accurately. In that case, the product of the surface pressure auto spectrum and some estimate of the correlation area may be used, with some error. This will be referred to as the **indirect** method for estimating dG_{pp}/dS. The result of the indirect method produces a spectrum which is just the surface pressure spectrum with the time derivative effect applied (i.e., $\omega^2 \times G_{p_s p_s}$). The difference between the two estimators for the dipole source strength per unit area is a measure of the error that would be incurred by estimating the contribution to the radiated acoustic pressure using blade surface pressure autospectral data only.

Figures 75, 76, and 77, show a comparison of the indirect and direct methods for estimating the dipole source strength per unit area at the chordwise blade locations on the suction surface, where the correlation area used for the indirect method is the surface area of the blade, S_a. Since this is the maximum that the correlation area can be, it is not surprising that the surface-pressure-based spectrum is considerably higher than that based on a direct measurement of the cross spectrum. The key difference between the results lies in the spectral distribution of energy. The decrease in efficiency of radiation by high frequencies is clearly demonstrated in these figures.

One of the most commonly applied models for the noise generation process on an airfoil consists of attributing the radiated noise to the fluctuating lift force over the blade surface. The instantaneous lift force can be defined at a point on the blade as the difference between the pressure- and suction-surface fluctuating pressures. This model takes into account the correlation between the two surface pressures and associates each chordwise and spanwise point with a lift force and presumably a source strength. An estimate of the dipole source strength per unit area is thus obtained by subtracting the pressure-side source strength from the suction-side dipole source strength per unit area.[25] Even though the cross spectra need not be measured simultaneously,[26] the probe-tube microphones would tend to interfere with the radiated sound field when measuring surface pressures on the opposite side of the blade from the far field acoustic microphone. The practical problems of measuring the pressure and suction side surface pressures at a given location using probe-tube microphones were resolved by the use of the miniature Kulite sensors, mounted in a back-to-back configuration.

Since calculation of the dipole source strength per unit area includes the $\cos\theta$ term which changes the sign of the cross spectrum between the acoustic pressure sampled opposite the suction side and the pressure-side surface pressure, the resultant

---

[25] Since addition is a linear operation, taking the cross spectrum between a reference signal and the output of a sum or difference amplifier ($x_{\pm}(t) = x_i \pm x_j$) is identical to subtracting the two cross spectra between the reference signal and each individual signal (i.e., $G_{y\pm} = G_{yi} \pm G_{yj}$).

[26] This was verified by comparing the cross spectrum obtained using a differencing amplifier with that computed from the difference between two cross spectral measurements.

dipole source strengths associated with the fluctuating lift force at a point may be obtained from the **sum** of the pressure-side and suction-side source strengths per unit area. The results of measurements made at the three chordwise locations are shown in Figure 78 on page 185. Contained in these data is information needed to rank-order each chordwise location as a function of frequency on the basis of the overall strength of the dipole sources related to the blade surface pressures. For the blade configuration under investigation, the leading edge turbulence interactions are responsible for most of the radiated noise over the mid-frequency range. Above 1 kHz the pressure sensors were not sensitive enough to resolve the associated source strengths which decay rapidly with frequency.

6.3 Conclusions

A series of experiments were performed using a single impeller blade immersed in an accessible and quantifiable flow field in an effort to better understand the radiation characteristics of the surface-pressure noise. The flow field was quantified using hot film anemometry and found to be typical of jet flow containing a central core region which is nearly laminar, and a mixing region which contains high turbulence levels. The blade was subdivided into three chordwise regions; leading edge, midchord, and trailing edge. Measurements were made in these regions on both the pressure side and suction side. The blade surface pressure statistics were determined from single- and dual-point measurements using both miniature pressure transducers and probe-tube microphones. The relationship between the surface pressure and radiated noise field was determined using frequency-domain cross-spectral density measurements between the local surface pressure and the far field acoustic pressure. These data were then used to estimate the dipole source strength per unit area and the correlation area at each point on the blade surface using equations which were derived in Chapter 2, "Theory of Aerodynamic Noise Generation."

The blade surface pressure data indicated that the low frequency fluctuations were associated with large scale eddies. This is in agreement with data presented by Brooks and Hodgson [17] who investigated the turbulent boundary layer pressure field on an airfoil. They found a slight frequency dependence of the convection velocity estimated from the phase of the cross spectrum. For the single blade configuration evaluated in this thesis, two distinct frequency regions existed which were associated with quite different values of convection velocity. The difference between the two regions was particularly noticeable for the pressure side, where a very high convection velocity was indicated by a nearly constant phase angle from 100 Hz to 750 Hz, with a linear slope to the phase above 750 Hz.

The surface pressure data show influences of both the local turbulent boundary layer development on the blade surface, and the free-stream turbulence characteristic of the mixing region. Incidence angle effects demonstrated an important feature of the surface pressure behavior. Relative to the grazing incidence flow condition, the streamwise, low frequency coherence as measured on the suction side (i.e., on the side opposite the incident flow) was enhanced, where the coherence on the pressure side decreases at low frequencies and increases at high frequencies indicating a relatively high level of broad band coherence. These trends may be explained by associating the enhanced low-frequency coherence with increased separation over the suction side (see flow simulation results) leading to the formation of large, low-frequency eddies. As a result of the blade orientation, the pressure side is more directly exposed to the incident free-stream turbulence which contains a wide range of eddy sizes.

Determination of the correlation area provided information similar to that obtained from the two-point surface pressure measurements, but in a more comprehensive manner (since the cross spectrum contains a summation of several two-point cross spectra). The correlation area is a measure of the efficiency of conversion of turbulent to acoustic energy. Correlation area measurements showed that the noise generation process was more efficient near the trailing edge than at the leading edge (for low frequencies; below 1 kHz). That is, more noise would be generated for the same source strength, or, as was the case for the single blade experiments, the same noise radiation would be produced from a region of lower source strength. The increased trailing edge efficiency is difficult to explain, but is probably related to the process of wake formation and vortex shedding from the trailing edge. It was also determined that the correlation area was as much as 25% of the blade surface area, and typically 10% or less. Correlation areas of this magnitude imply that the resolution of different source regions in the streamwise direction is difficult due to the high correlation between points. The magnitude of the correlation area is an important parameter for analyzing the full scale rotating impeller since the primary obstacle in correlating the rotating blade surface pressure with the radiated noise field is the poor coherence between the signals. A correlation area of 10% implies that, for a 26-bladed impeller, the signal from a single correlation area is approximately 25 dB below the level of the uncorrelated noise radiated from other portions of the blade surfaces.

Dipole source strength per unit area is a direct measure of the noise radiated from a specific point on the surface. The source strength distribution provides a complete picture of the relative importance of various acoustic source regions over the blade surface. For the single blade experiments, the region on the blade surface with the strongest source strength was the leading edge. This distinction was primarily at low frequencies, and became less significant above 1 kHz. The source strength determination was sensitive to blade location and thus the characteristics of the incident turbulence.

The concept of a fluctuating lift force was employed by correlating the surface pressure difference between the pressure and suction sides of the blade with the radiated noise. It was found that the lift force correlation could accurately be determined from the difference between two cross spectral density measurements, without the need for measuring the cross spectrum using the difference signal from a real-time differencing circuit. The pressure and suction side correlations should however be determined using the identical experimental setup since any disturbance would cause the estimate of the difference signal cross spectrum to deteriorate.

The effects of local surface pressure interactions were clearly demonstrated from the comparison of the direct and indirect methods for estimating the dipole source strength per unit area. Source interactions among the high frequency, small scale turbulence on the blade surface are confined to a relatively small region surrounding the measurement point. Hence the efficiency of conversion to acoustical energy is significantly decreased from that of the low frequency turbulence.

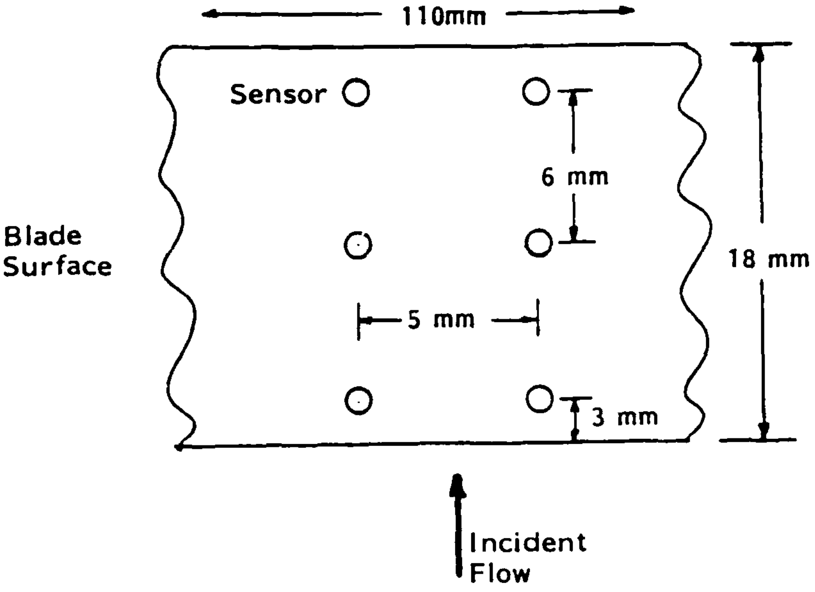

Figure 41. Schematic of Sensor Locations on Blade Surface.

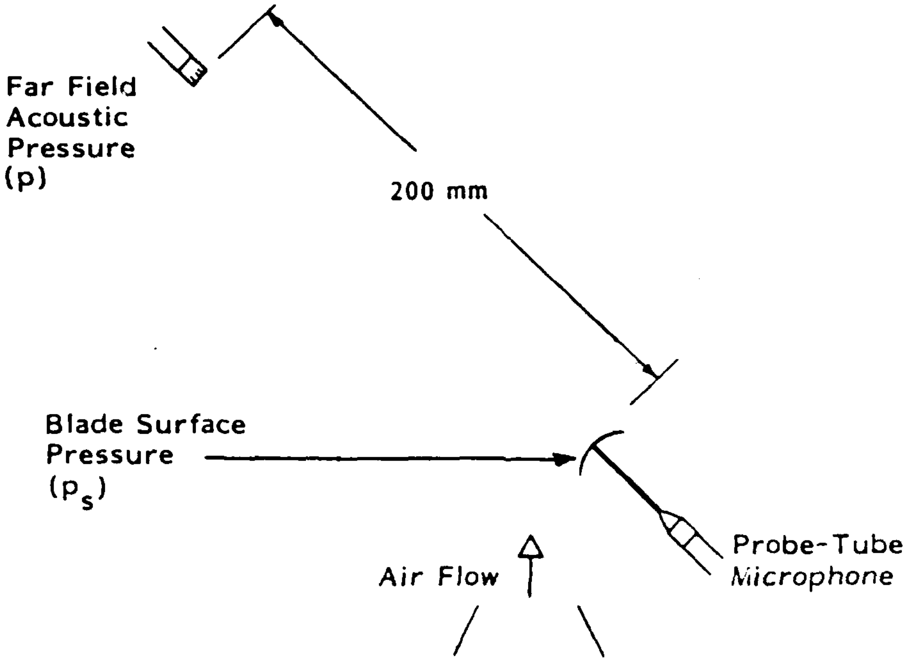

Figure 42. Schematic of Single Blade Measurements.

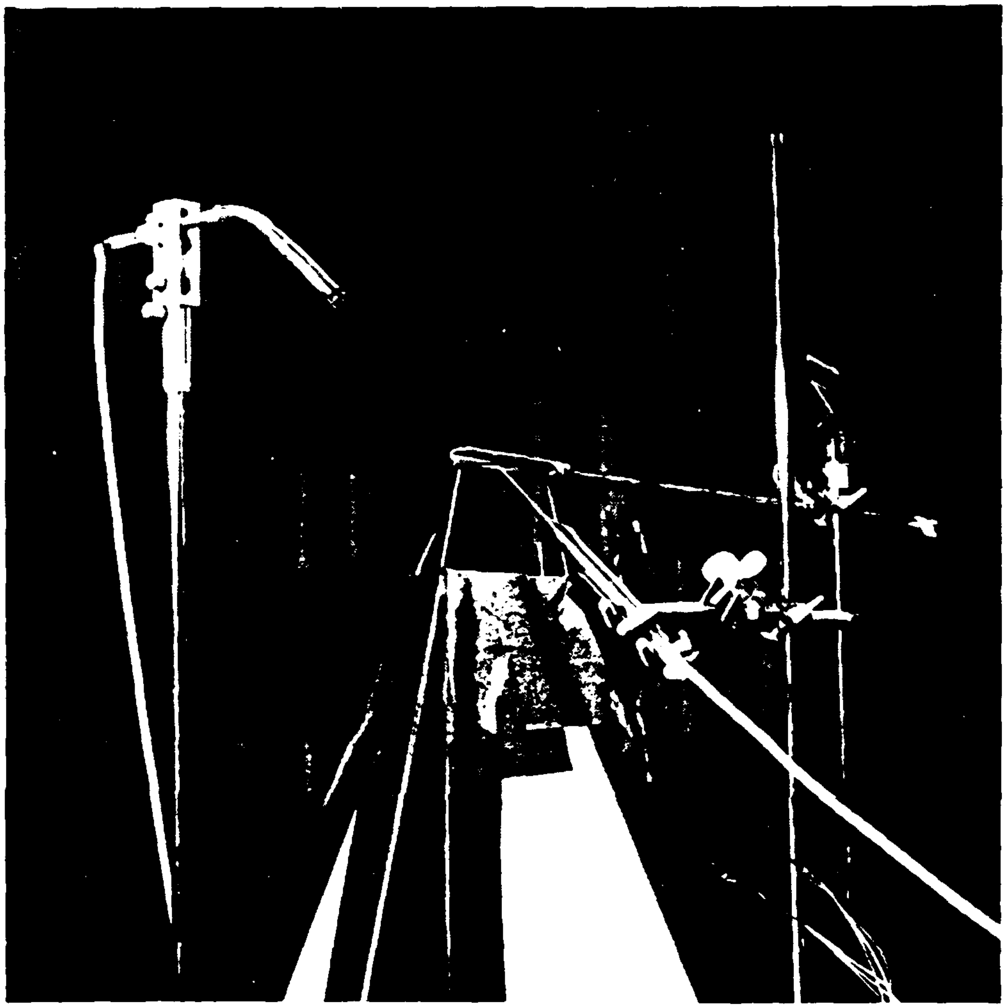

Figure 43. Photograph of Single Blade Experimental Setup

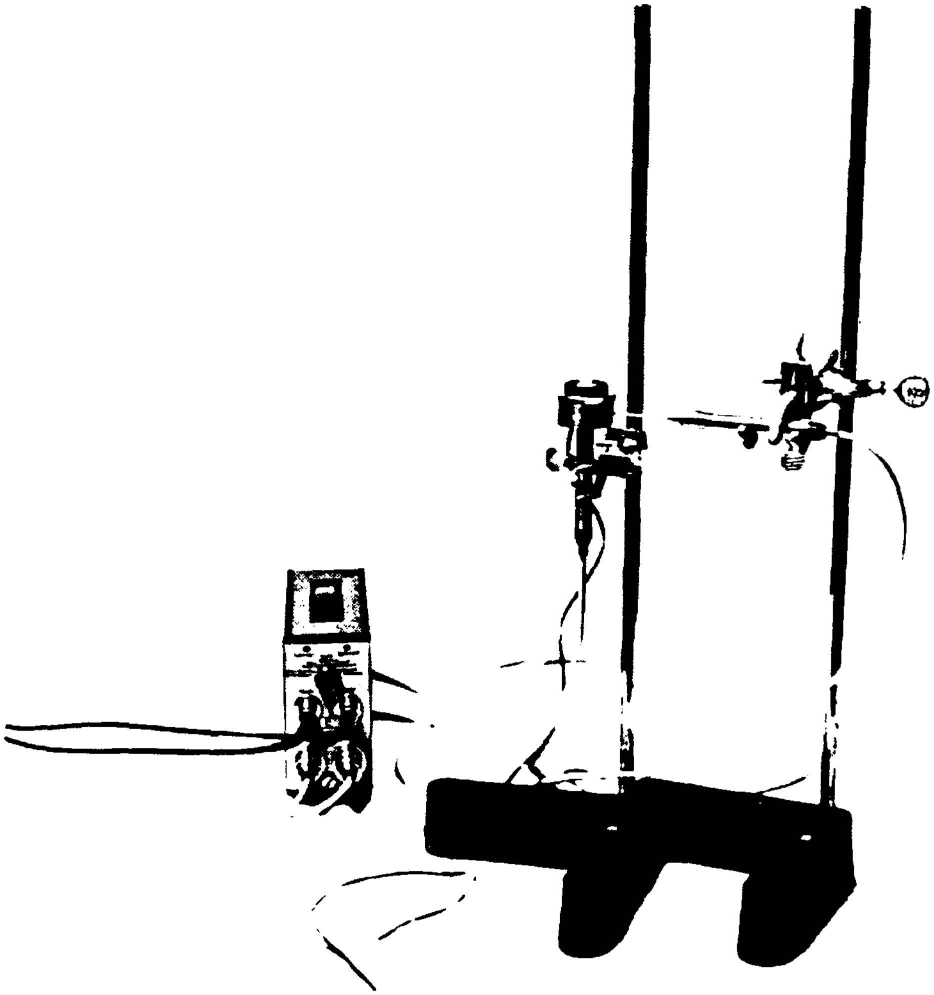

Figure 44. Photograph of Probe-Tube Calibration Apparatus The same coupler was used for calibrating the Kulite transducers as well.

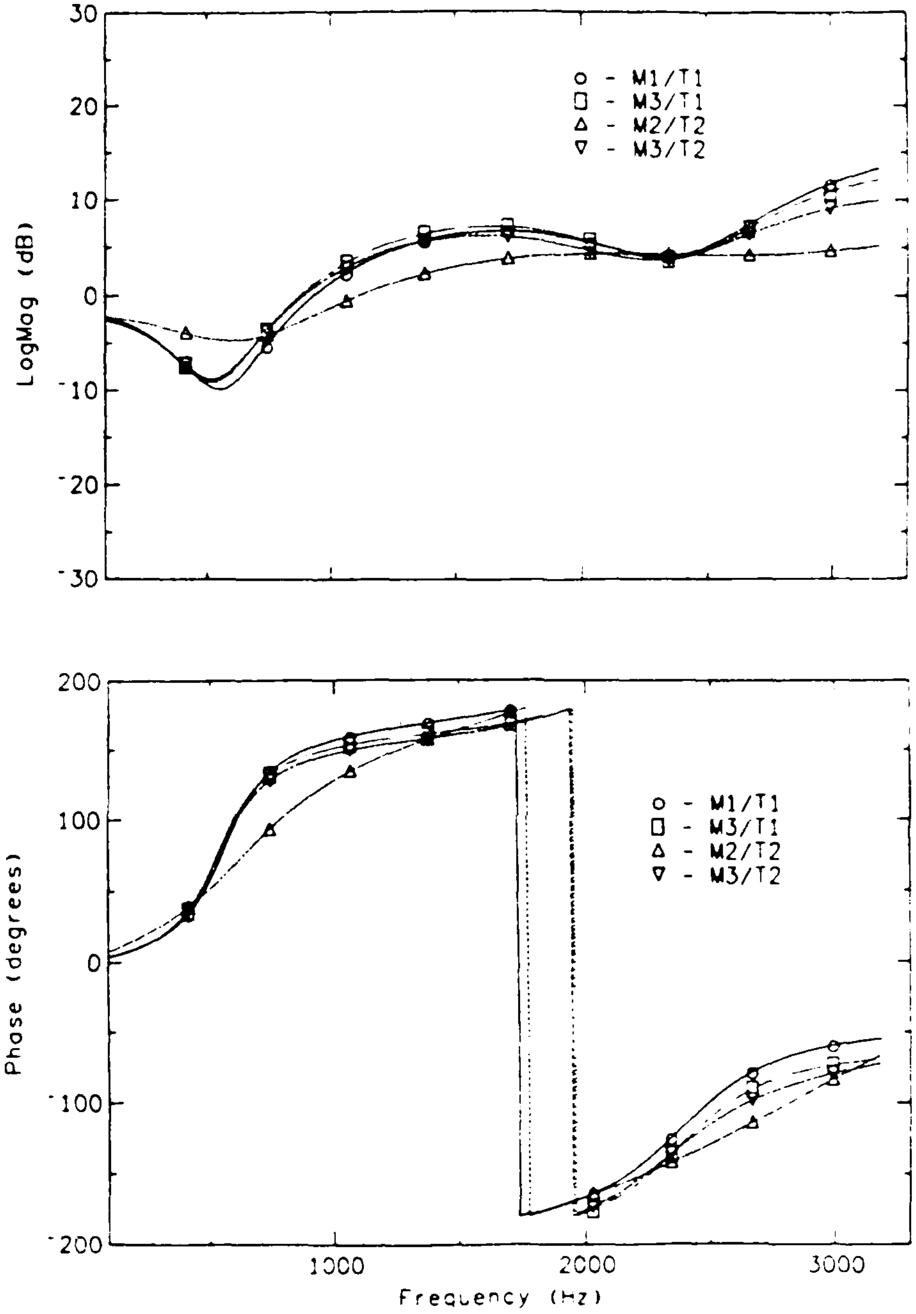

Figure 45. Calibration Transfer Functions for Probe-Tube Microphones. Each transfer function is relative to a reference Bruel and Kjaer microphone.

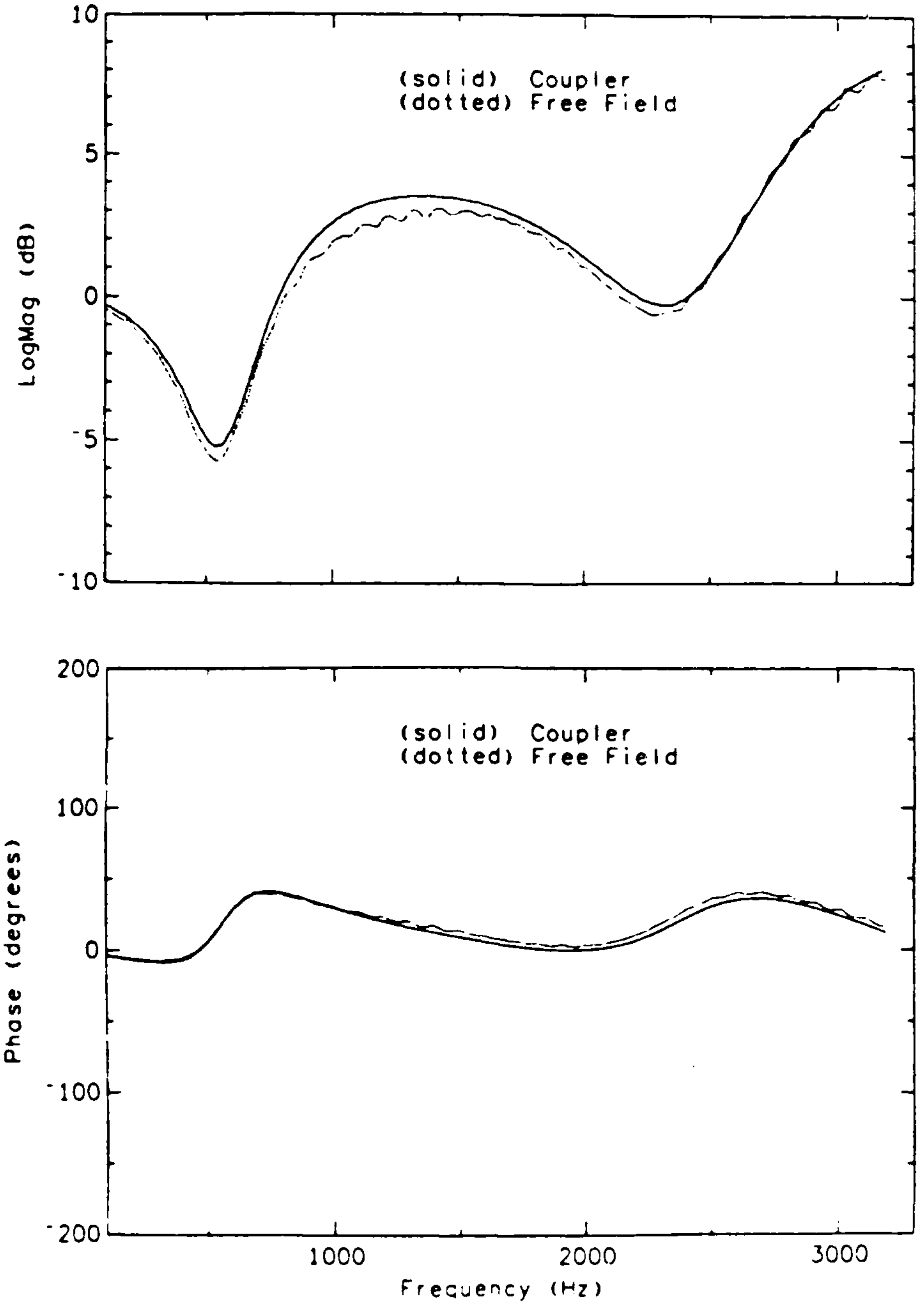

Figure 46. Free Field vs Coupler Calibration Data. Free field measurements were made in an anechoic room in the plane wave region of a monopole loudspeaker source.

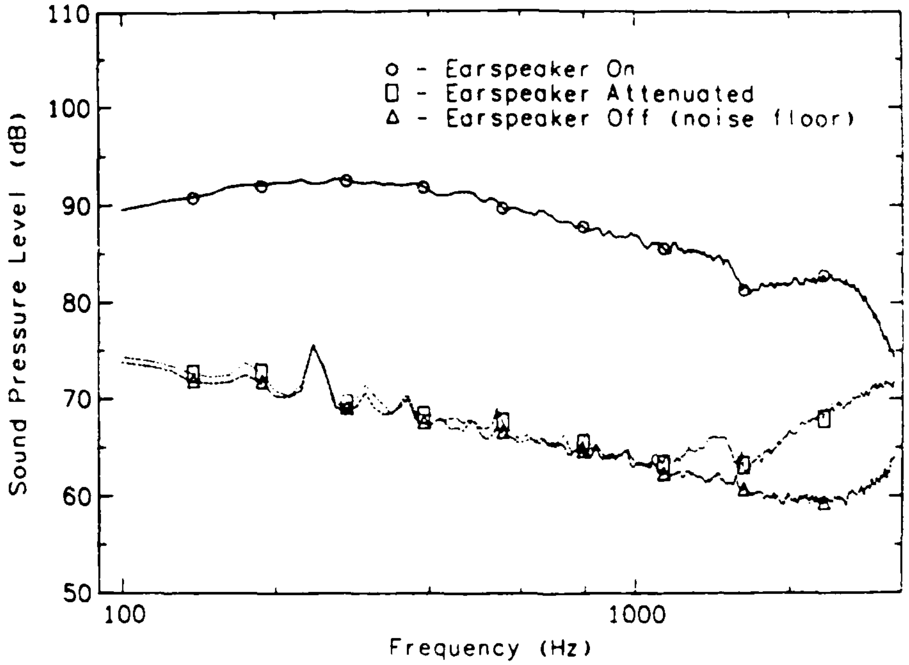

Figure 47. Sound Pressure Level in Acoustic Coupler as Measured by Kulites.

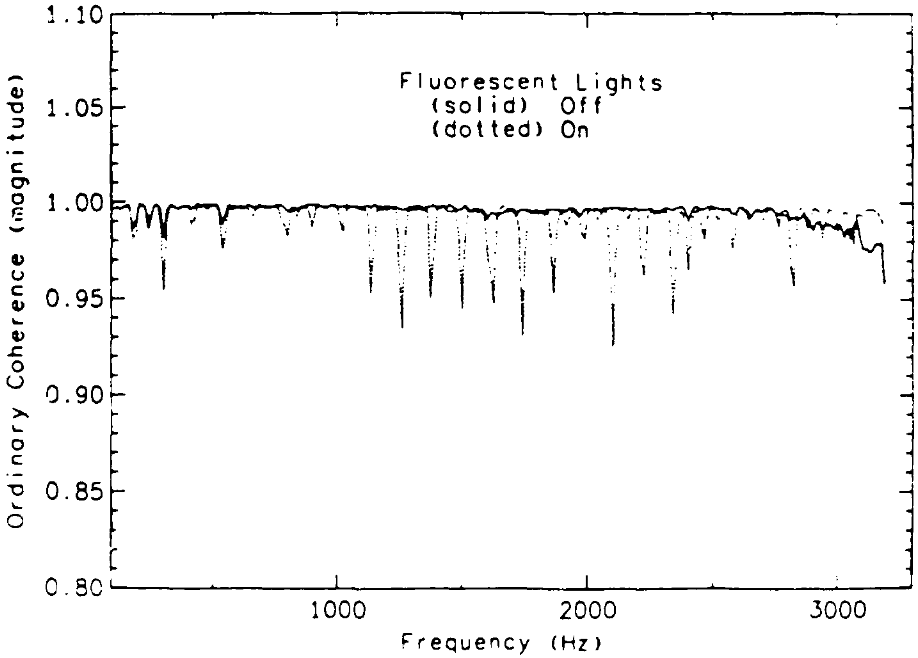

Figure 48. Effect of Fluorescent Lights on Kulite Output.

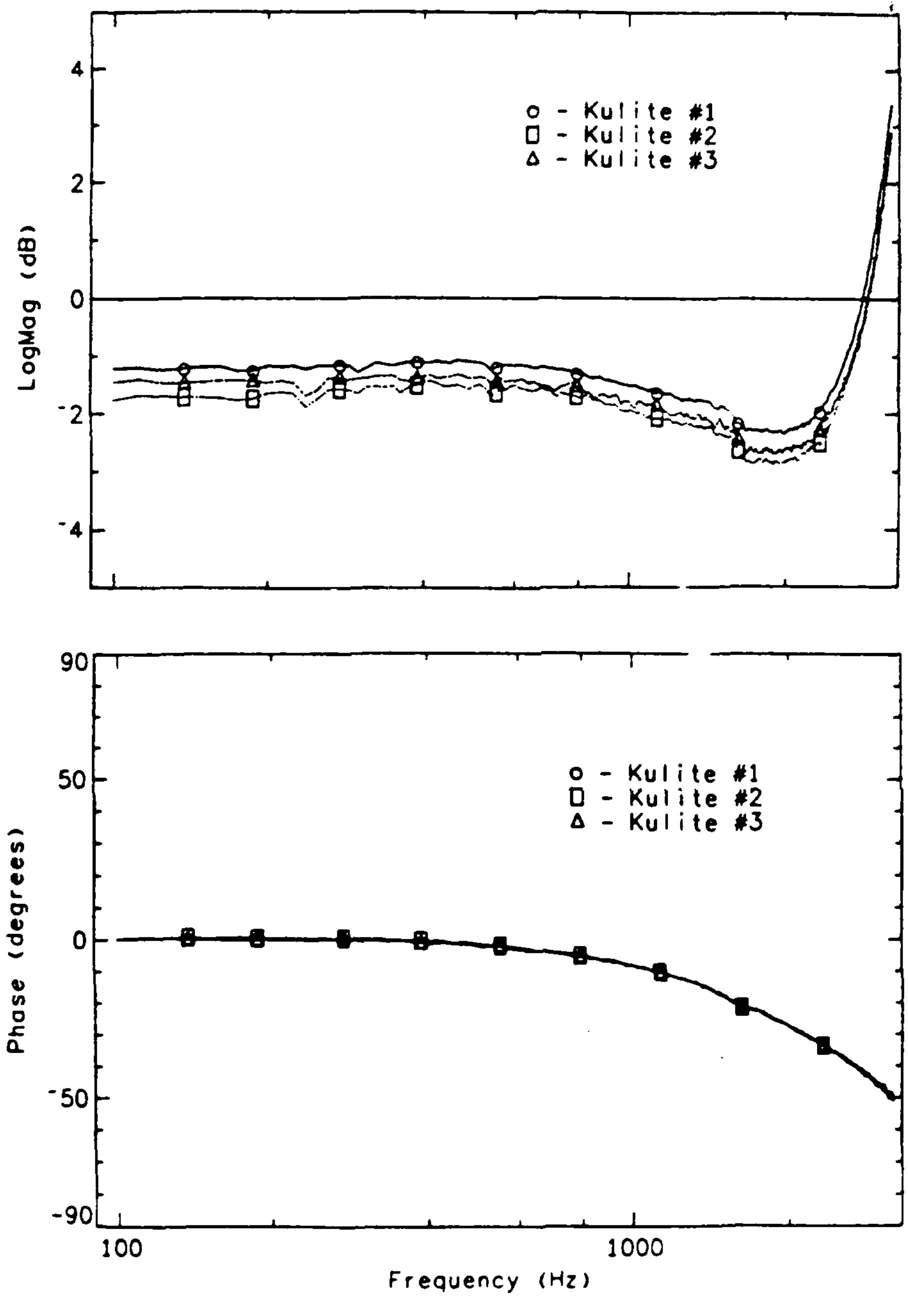

Figure 49. Kulite Calibration Transfer Functions. The data shows the relative response between the Kulite transducer and the reference microphone.

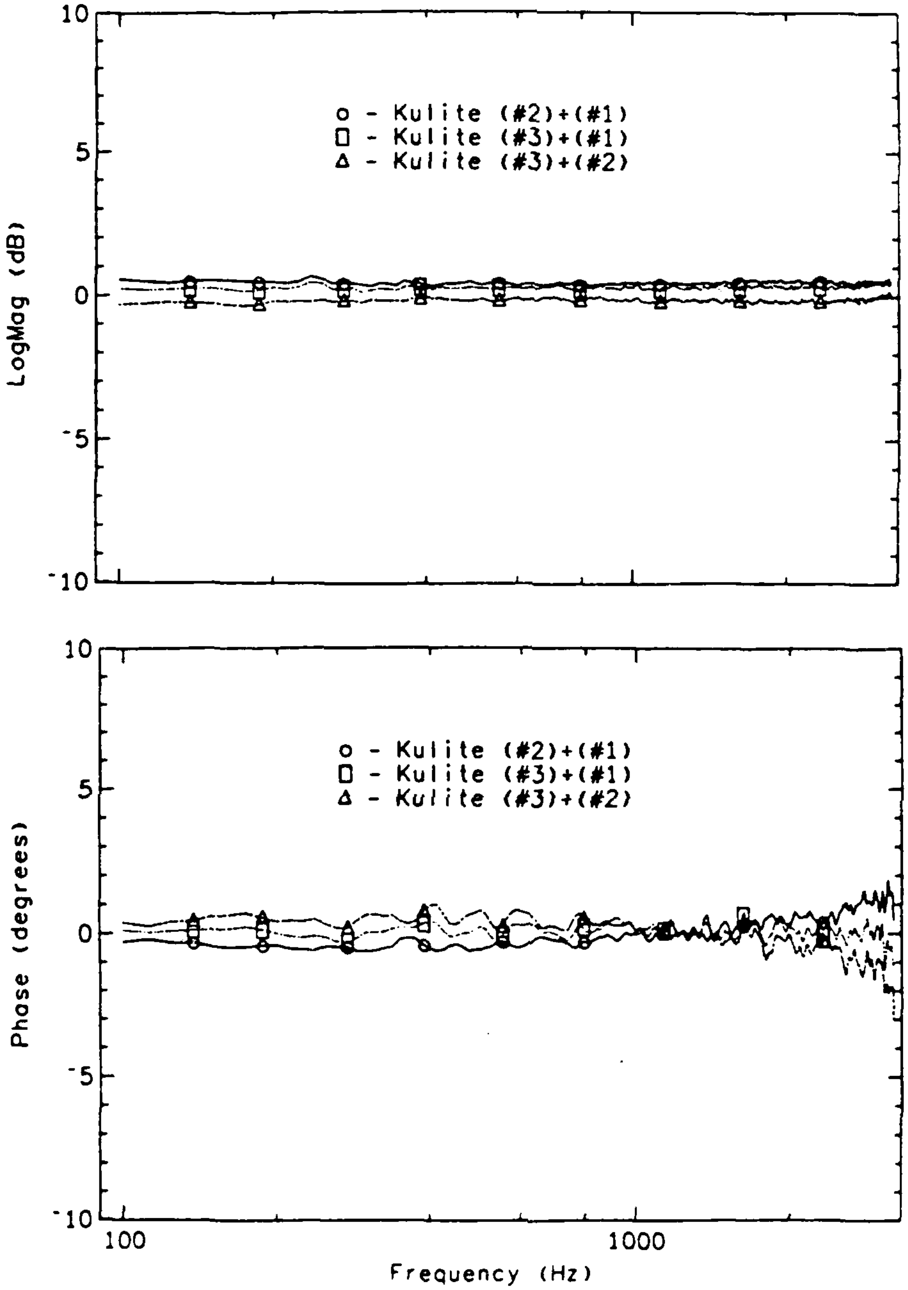

Figure 50. Relative Response Between Kulites. The Kulites were well matched as evidenced by the similarity in the transfer functions taken between the Kulites.

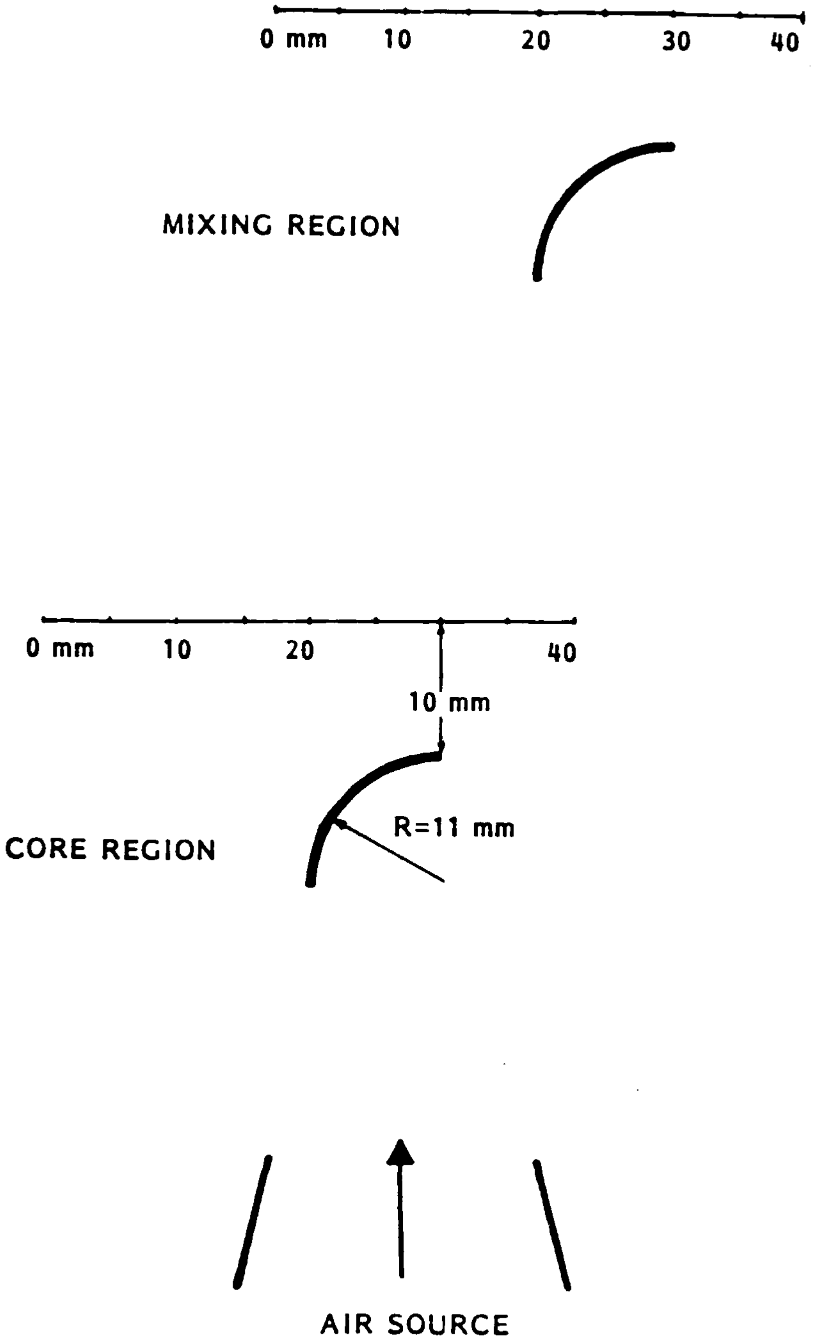

Figure 51. Schematic of Blade Position and Blade Wake Measurement Locations.

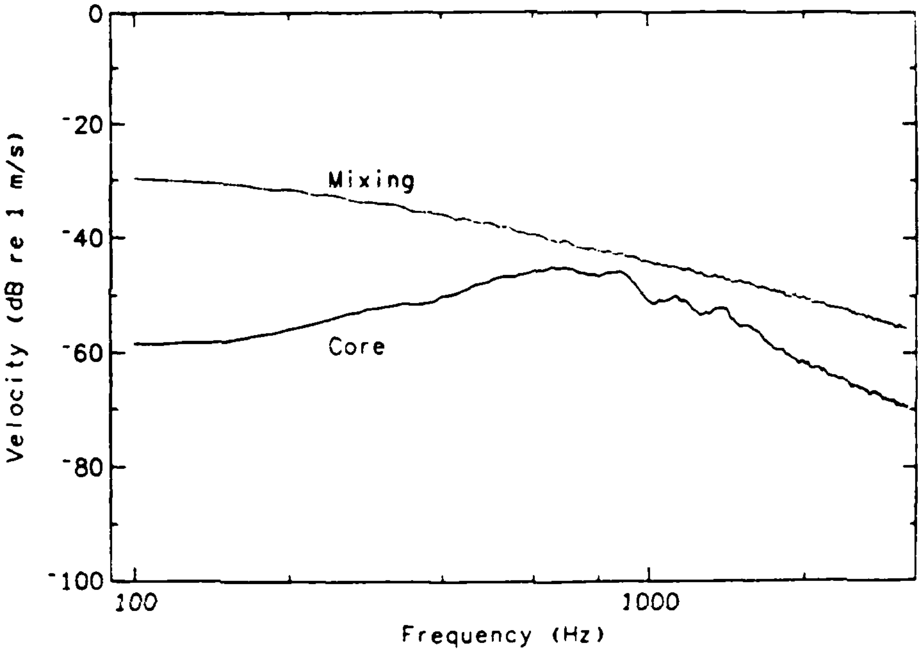

Figure 52. Velocity Spectra in Jet without Blade Present — Leading Edge.

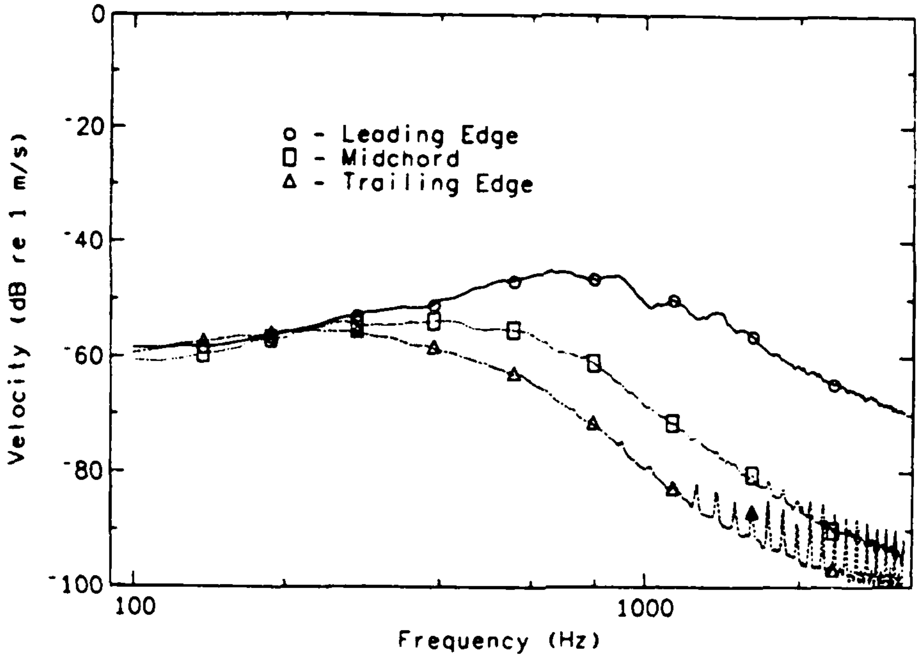

Figure 53. Velocity Spectra in Jet without Blade Present — Core Region.

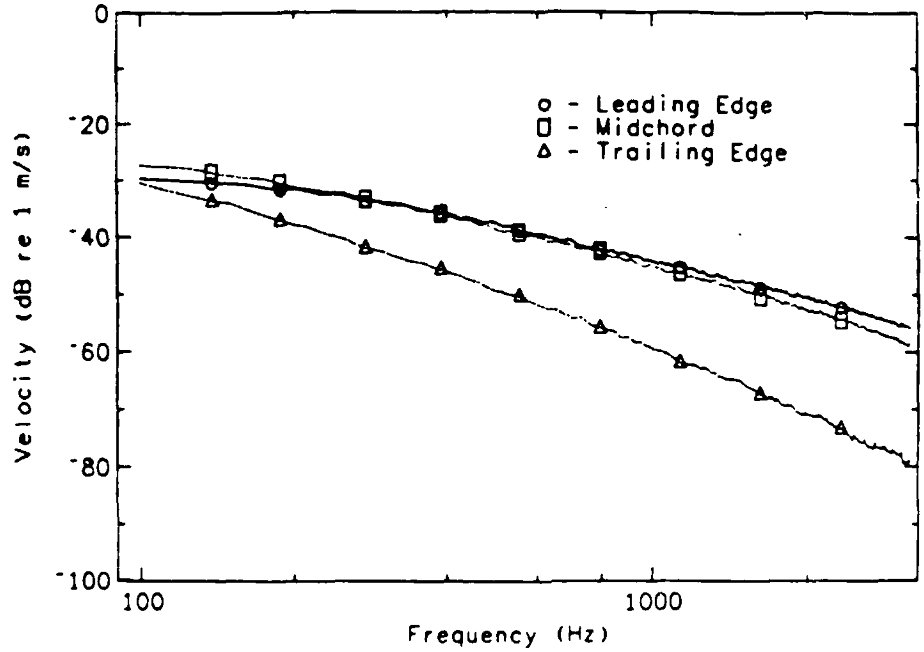

Figure 54. Velocity Spectra in Jet without Blade Present — Mixing Region.

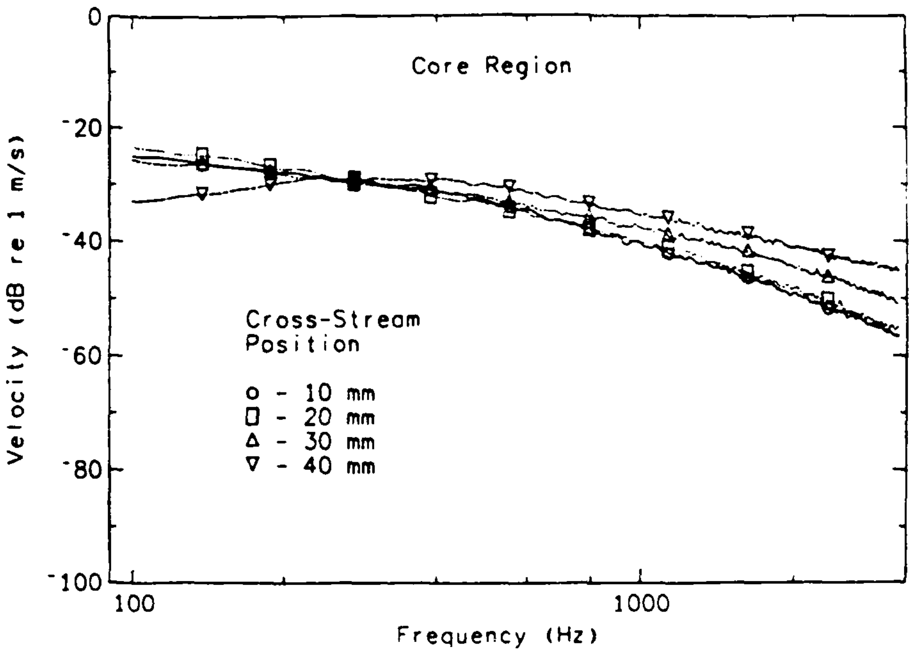

Figure 55. Velocity Spectra in Jet with Blade Present — Core Region.

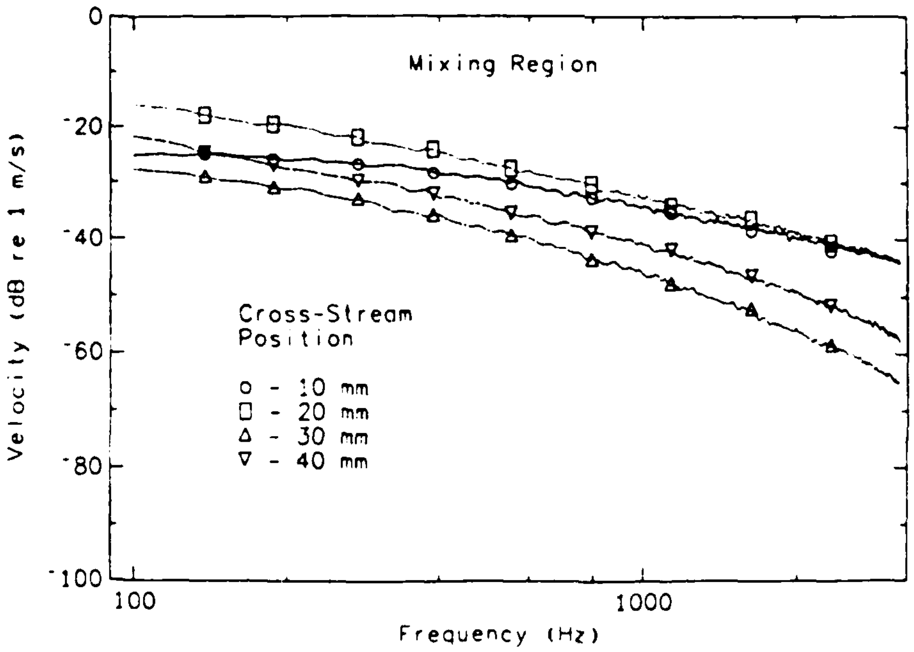

Figure 56. Velocity Spectra in Jet with Blade Present — Mixing Region.

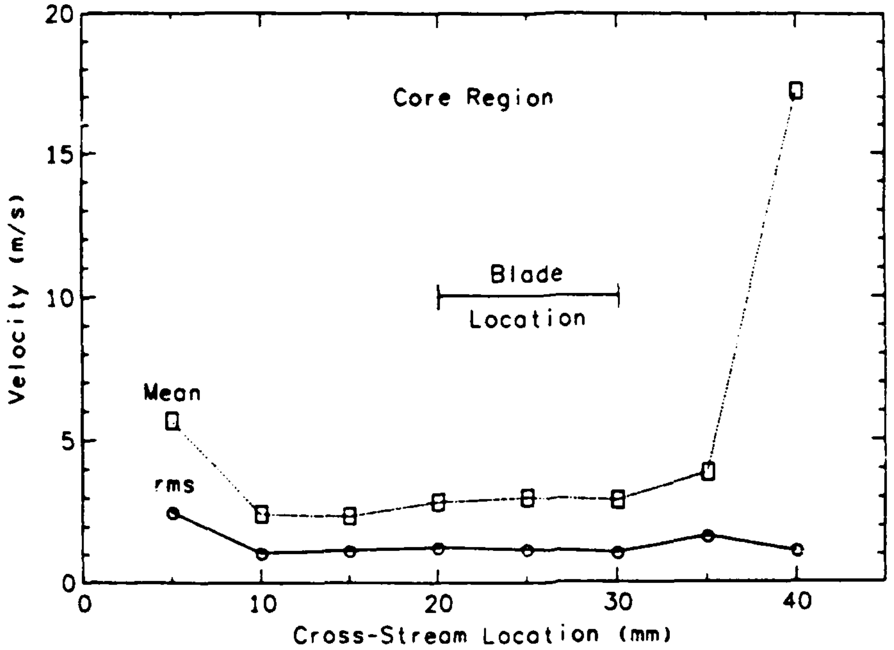

Figure 57. Velocity Distribution in Jet with Blade Present — Core Region.

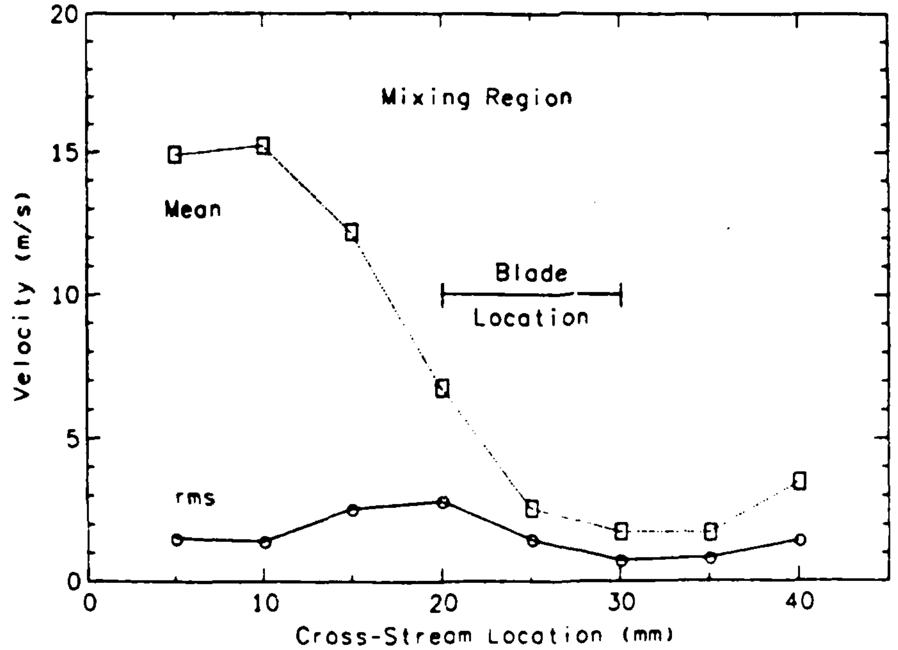

Figure 58. Velocity Distribution in Jet with Blade Present — Mixing Region

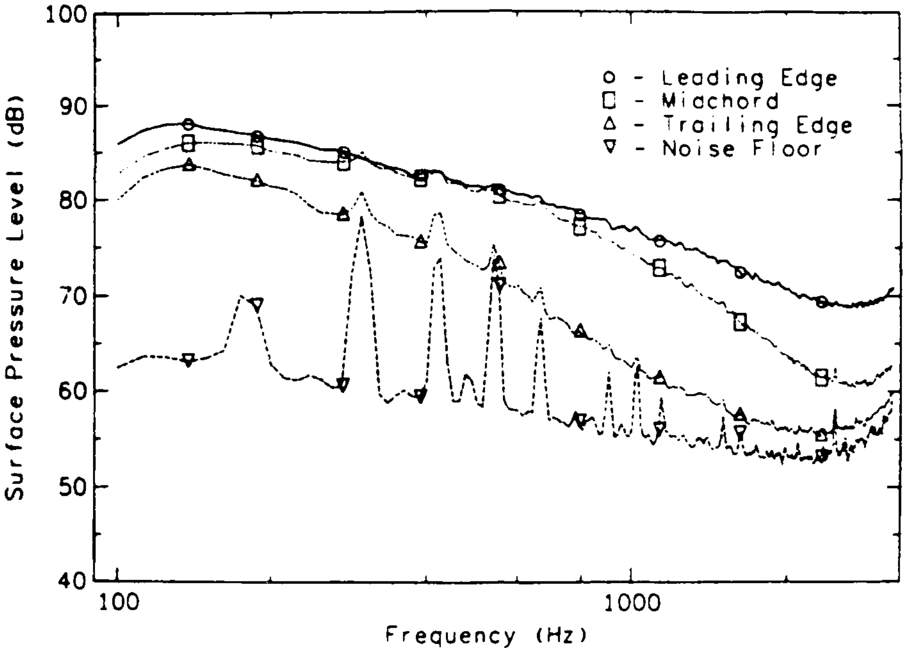

Figure 59. Blade Surface Pressure in Mixing Region — Suction Side.

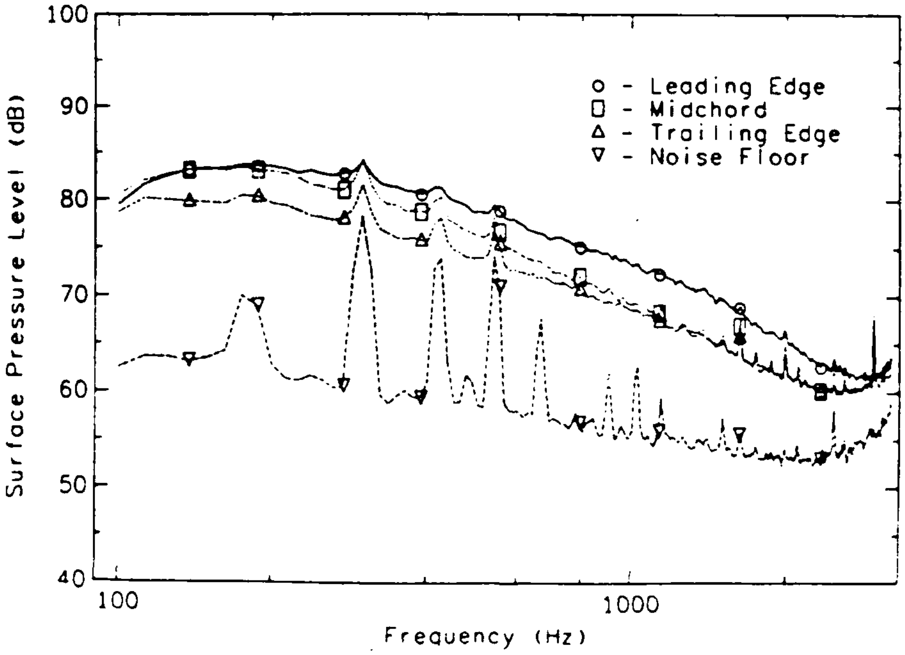

Figure 60. Blade Surface Pressure in Mixing Region — Pressure Side.

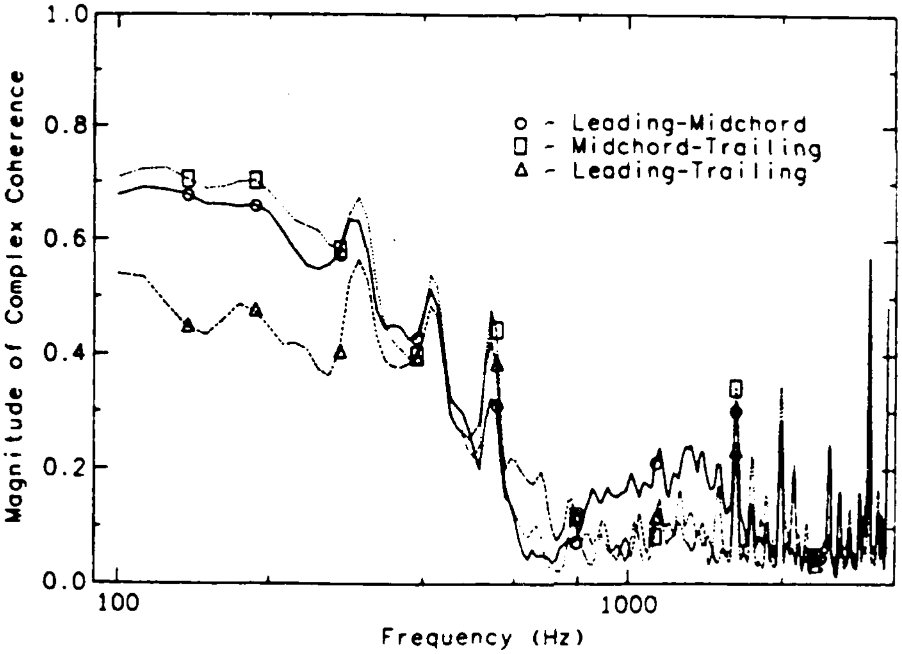

Figure 61. Complex Streamwise Coherence in Mixing Region — Pressure Side.

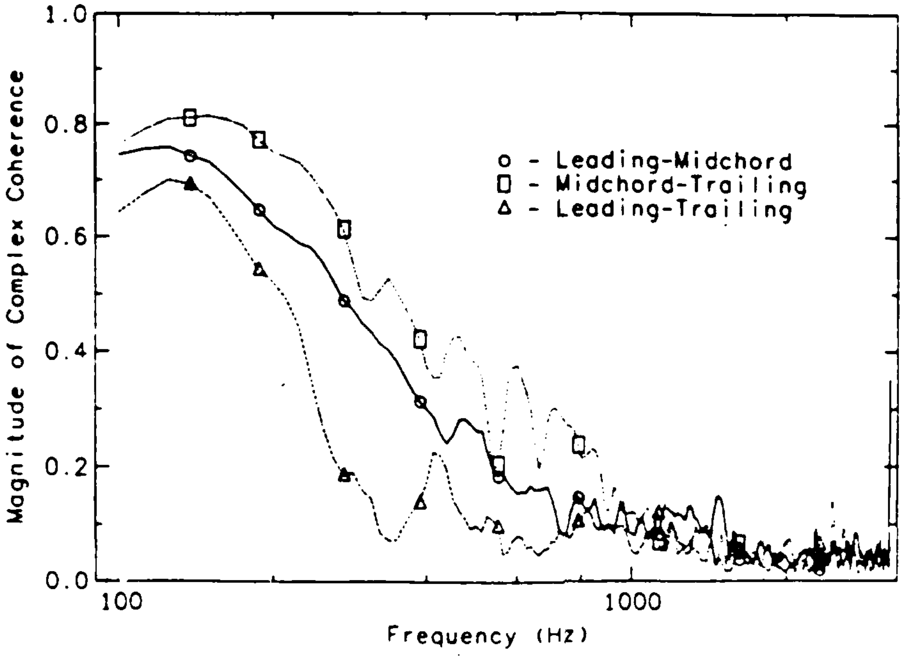

Figure 62. Complex Streamwise Coherence in Mixing Region — Suction Side

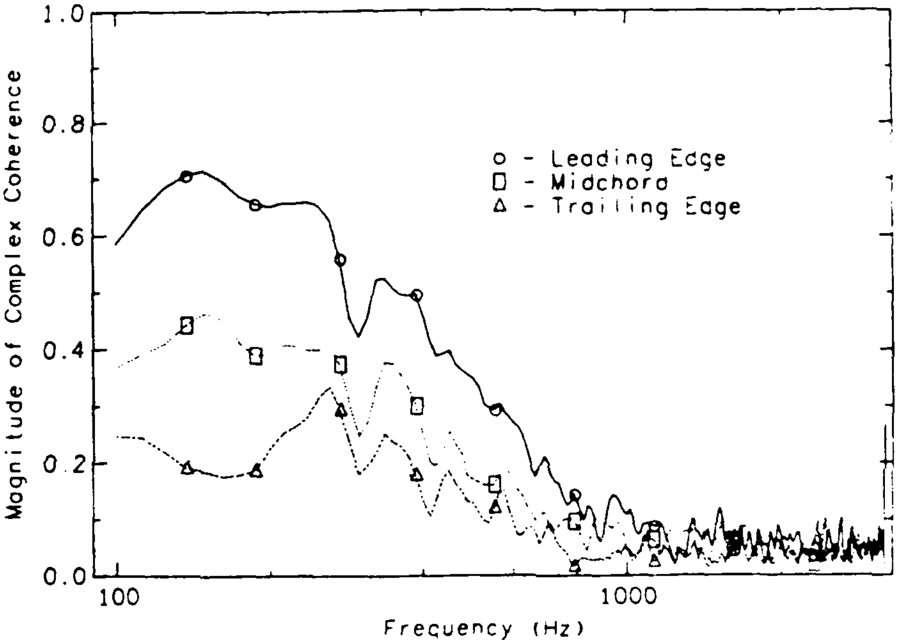

Figure 63. Complex Spanwise Coherence in Mixing Region – Pressure Side

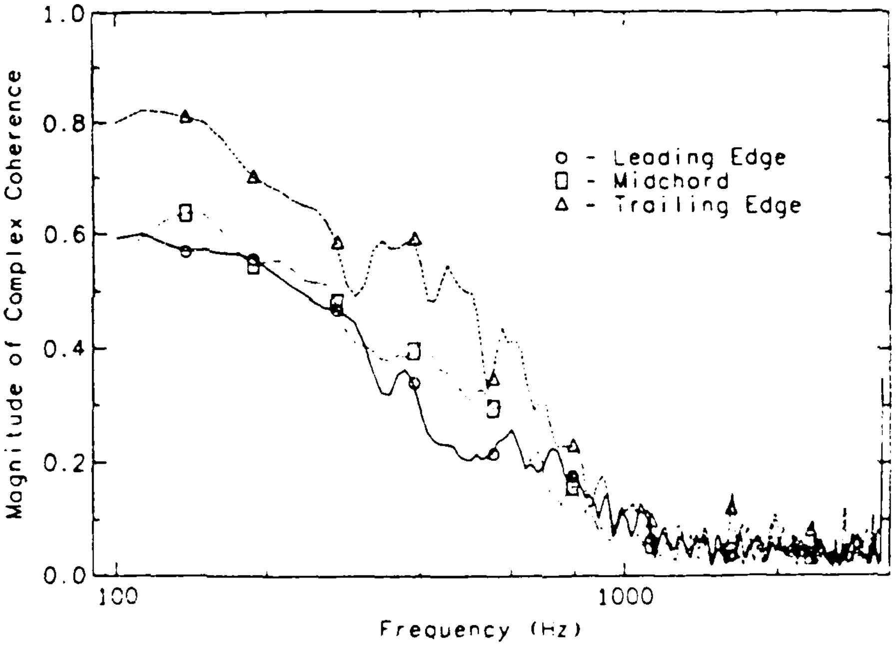

Figure 64. Complex Spanwise Coherence in Mixing Region – Suction Side.

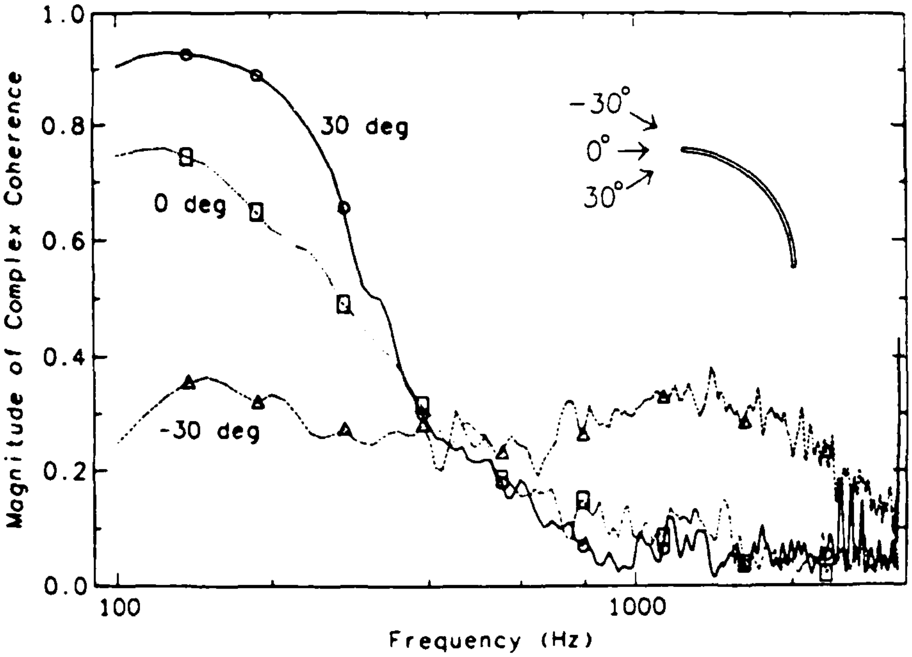

Figure 65. Effect of Incidence Angle on Complex Streamwise Coherence.

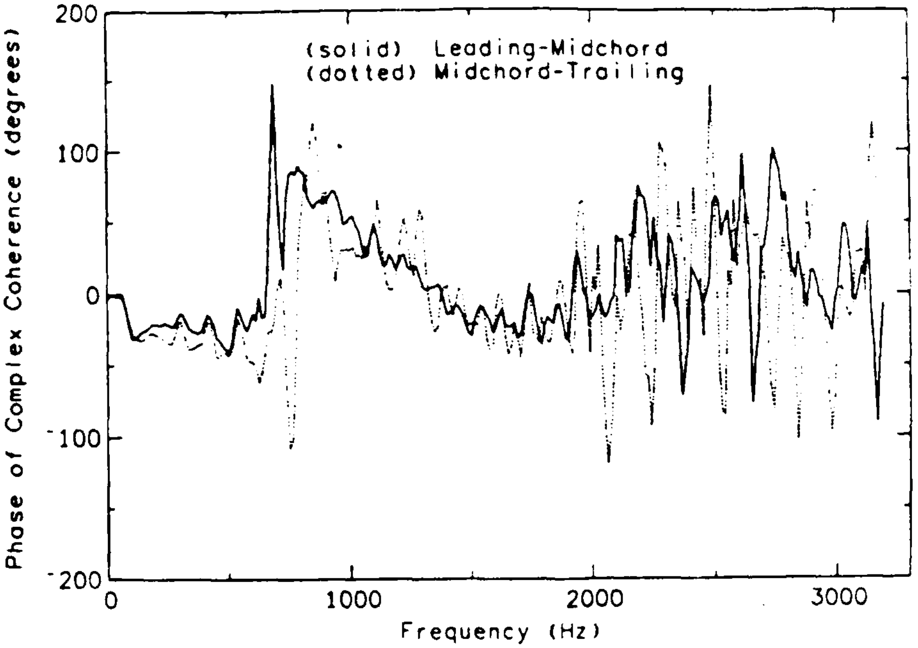

Figure 66. Phase of Complex Streamwise Coherence on Pressure Side.

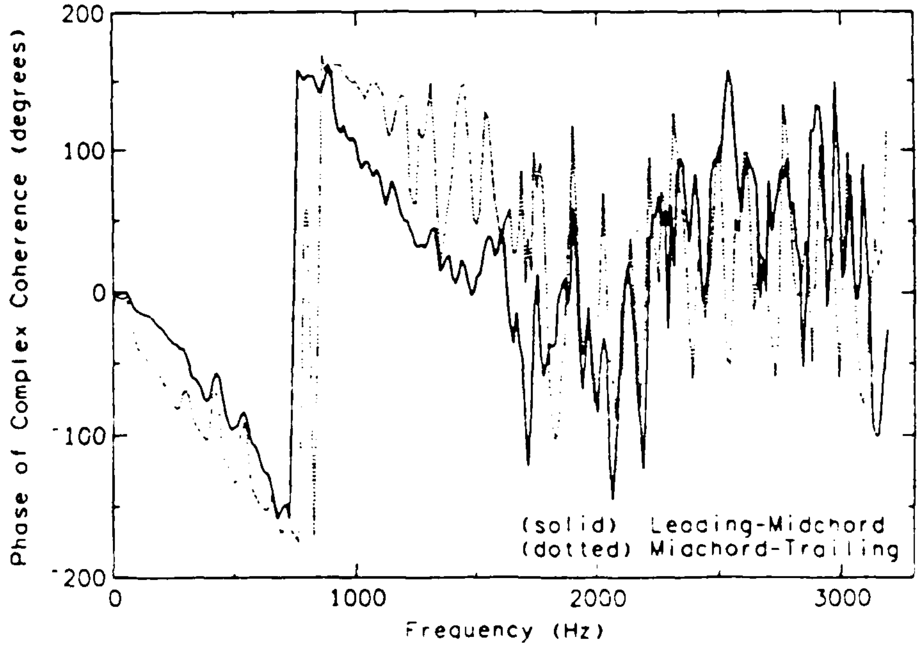

Figure 67. Phase of Complex Streamwise Coherence on Suction Side.

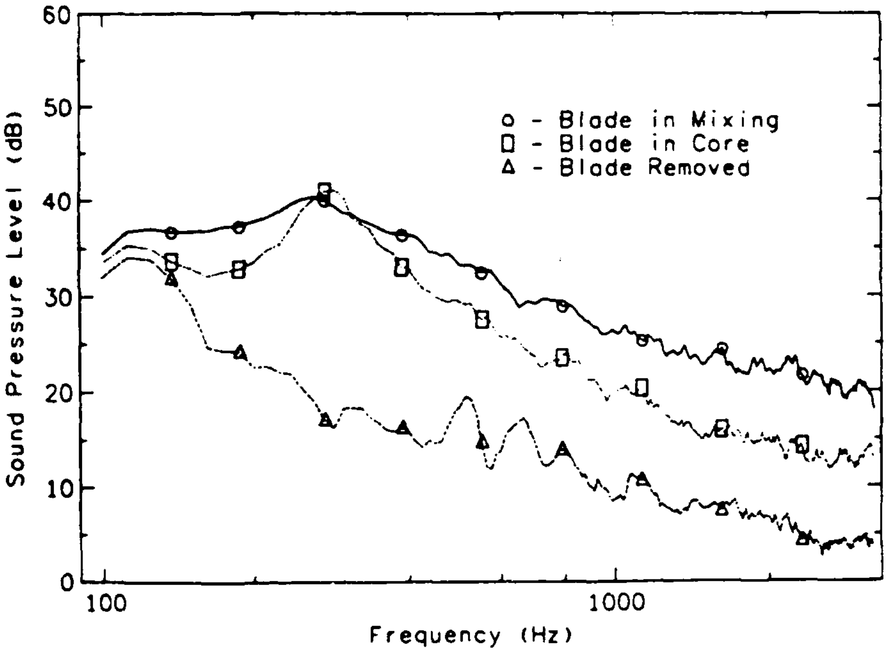

Figure 68. Sound Pressure Level at Distance of 200 mm from Blade.

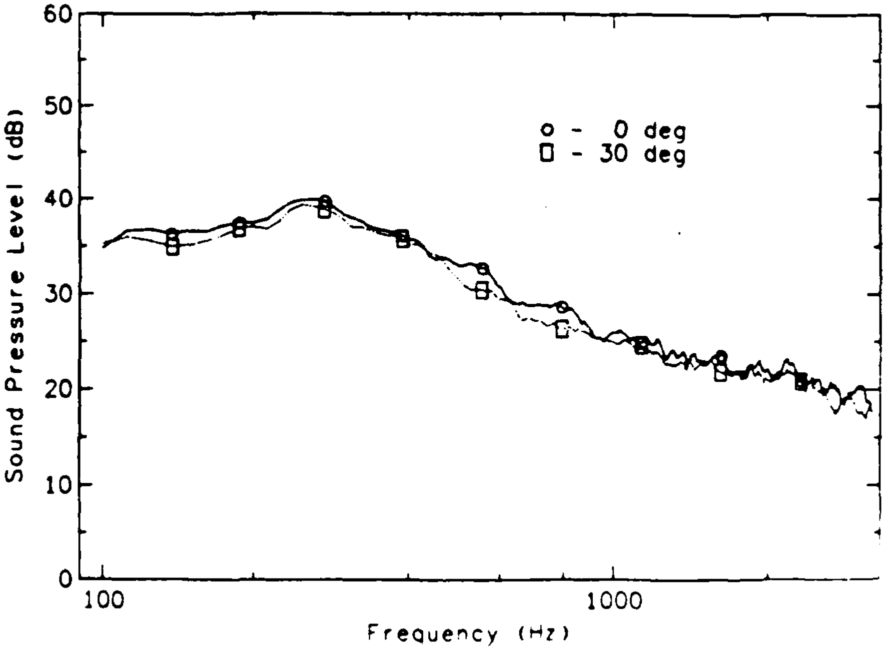

Figure 69. Sound Pressure Level Variation with Angle.

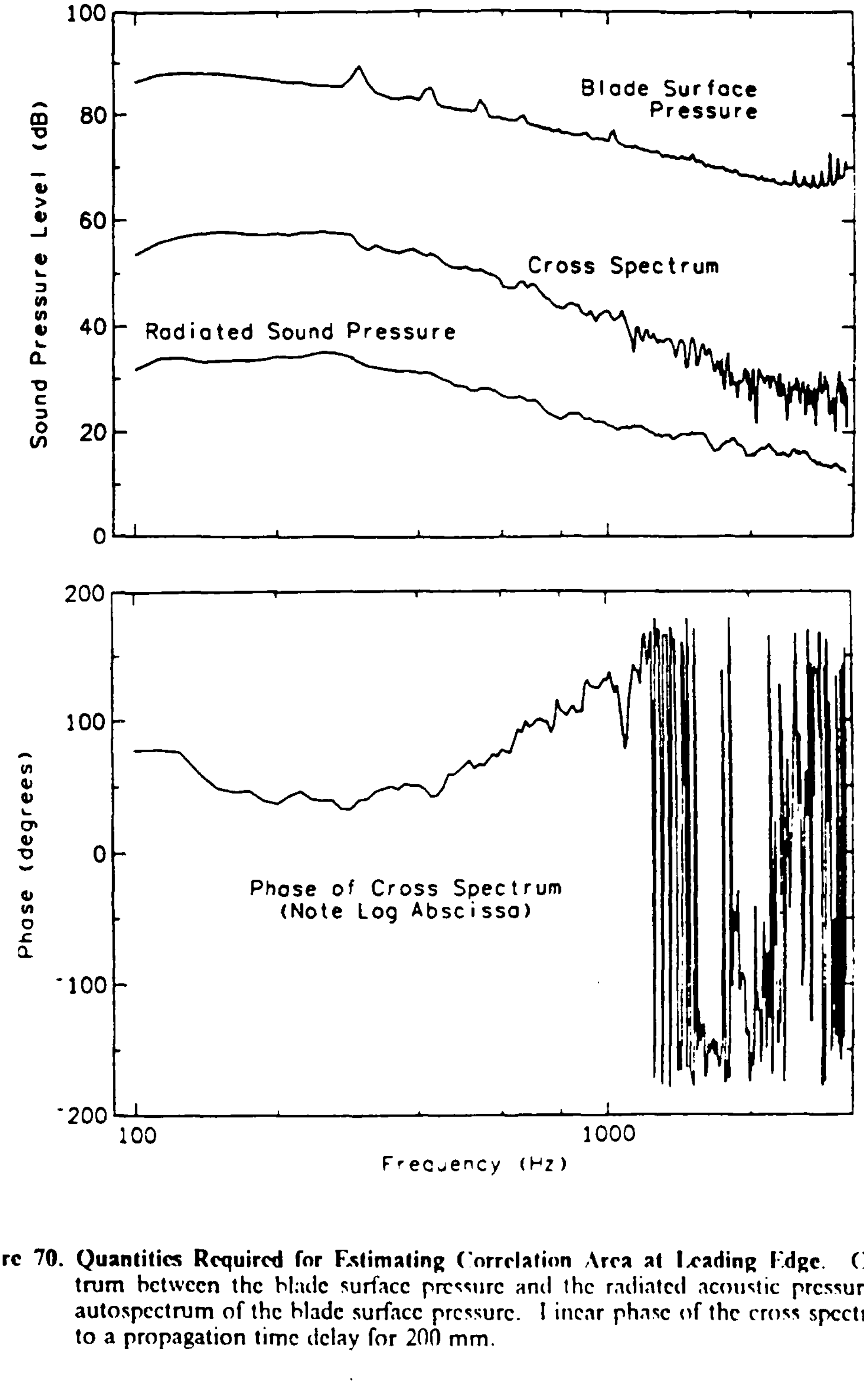

Figure 70. Quantities Required for Estimating Correlation Area at Leading Edge. Cross spectrum between the blade surface pressure and the radiated acoustic pressure, and the autospectrum of the blade surface pressure. Linear phase of the cross spectrum is due to a propagation time delay for 200 mm.

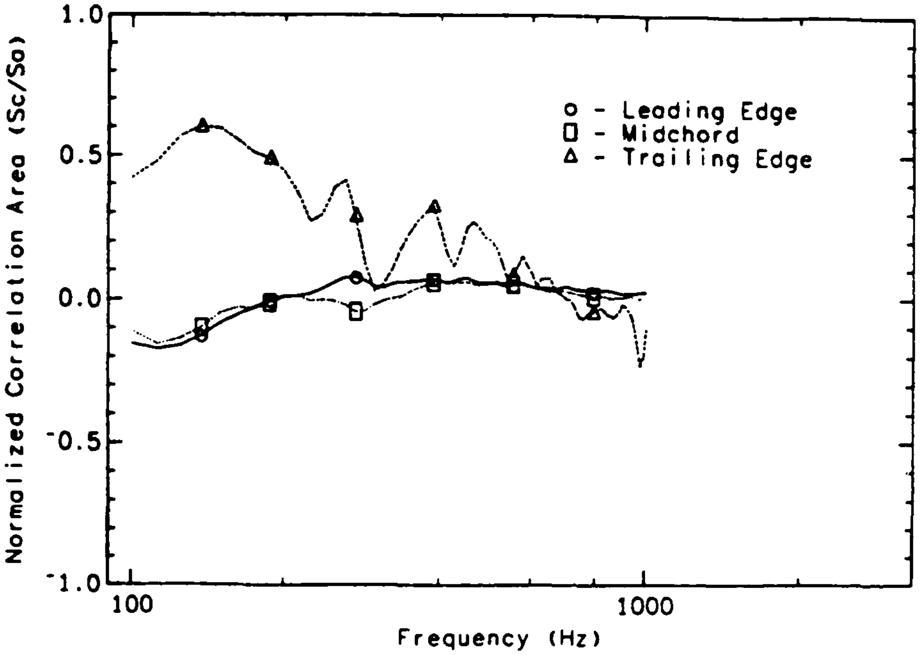

Figure 71. Suction Side Correlation Area — Mixing (Kulites).

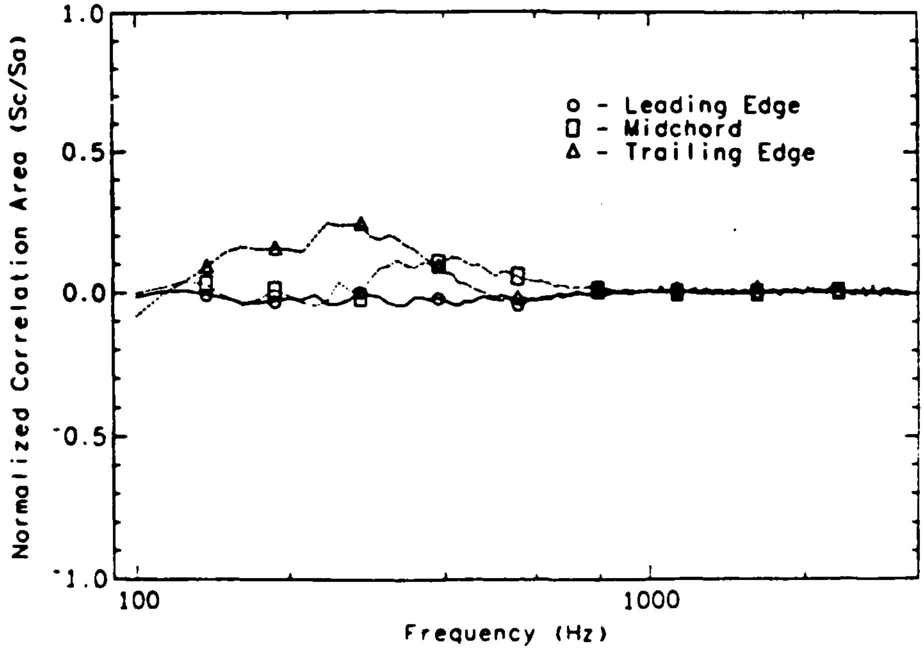

Figure 72. Suction Side Correlation Area — Arbitrary Location (Probe Tubes).

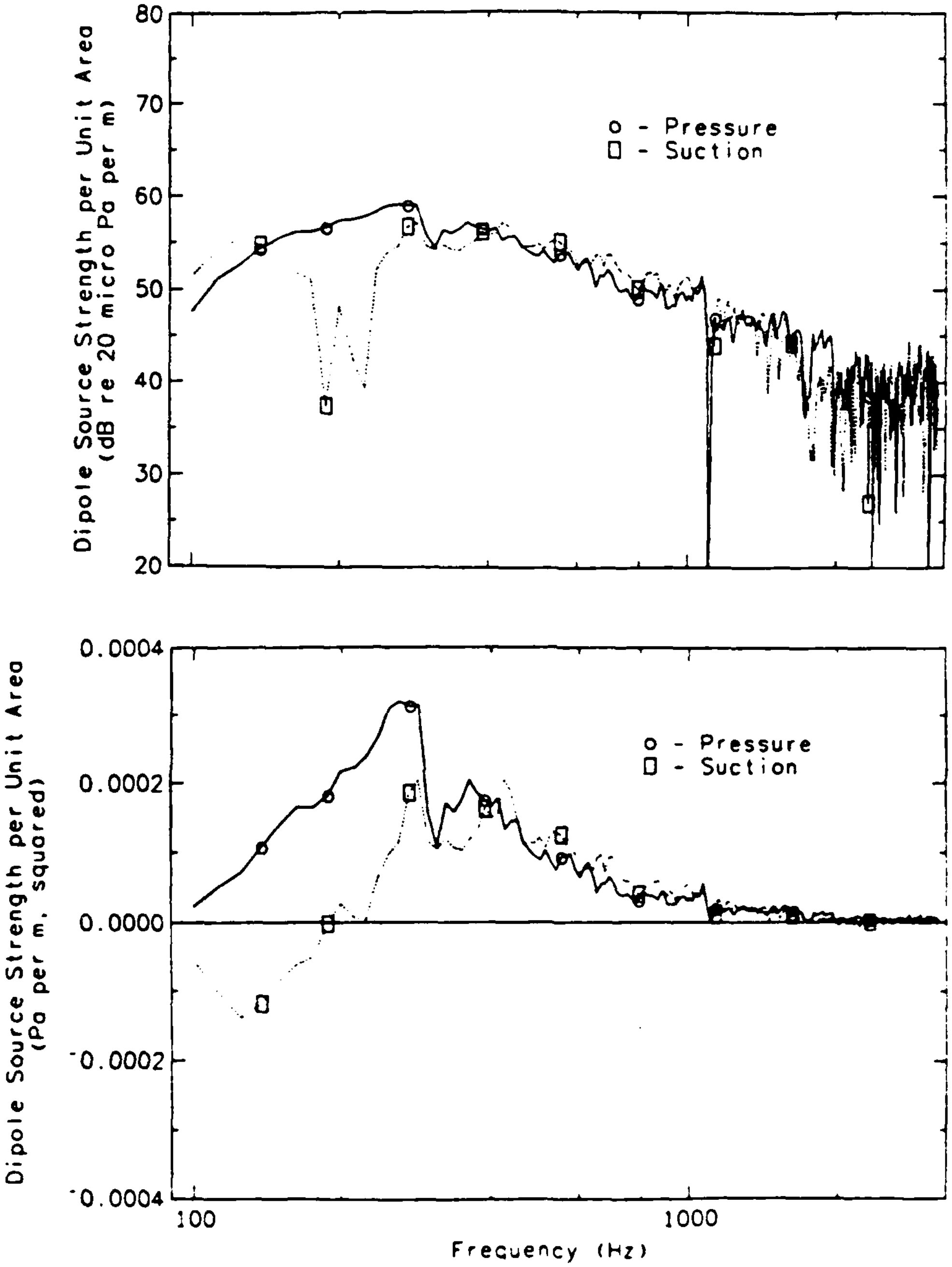

Figure 73. Dipole Source Strength at Leading Edge — Mixing. Kulite pressure transducers were used.

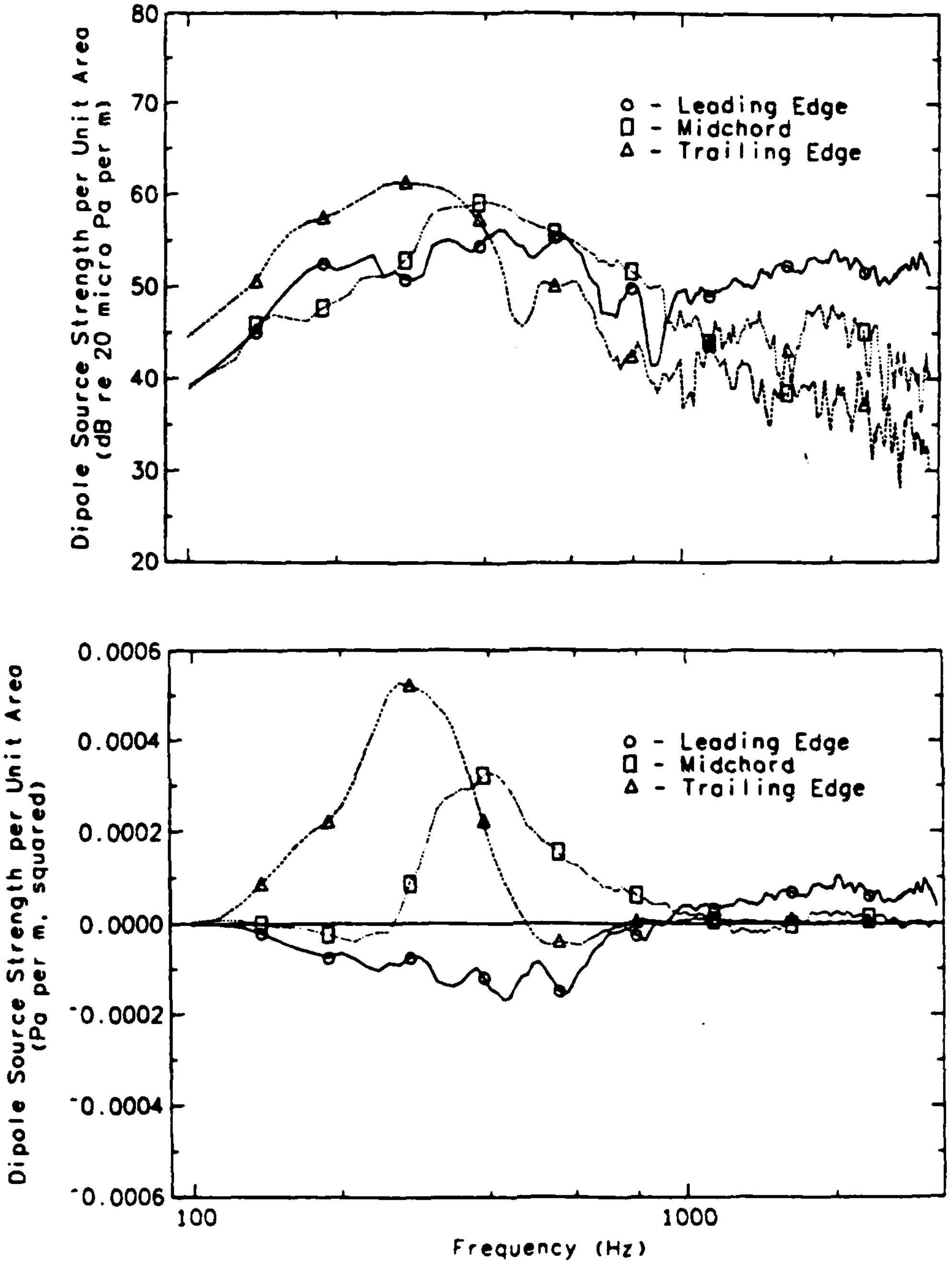

Figure 74. Dipole Source Strength for Blade at Different Location. Probe-tube microphones were used.

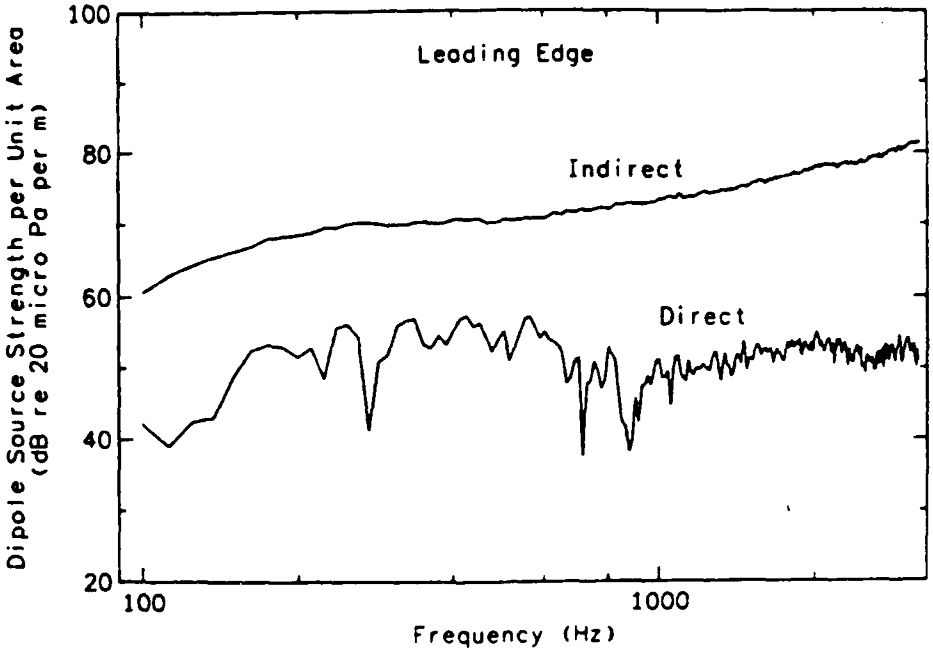

Figure 75. Comparison of Dipole Source Strength Estimators at Leading Edge.

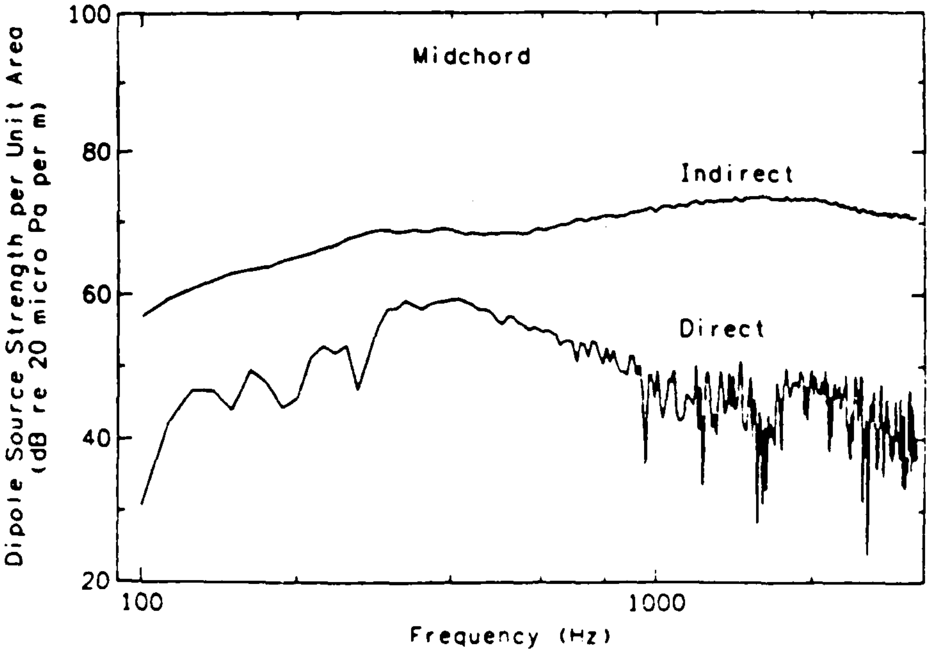

Figure 76. Comparison of Dipole Source Strength Estimators at Midchord

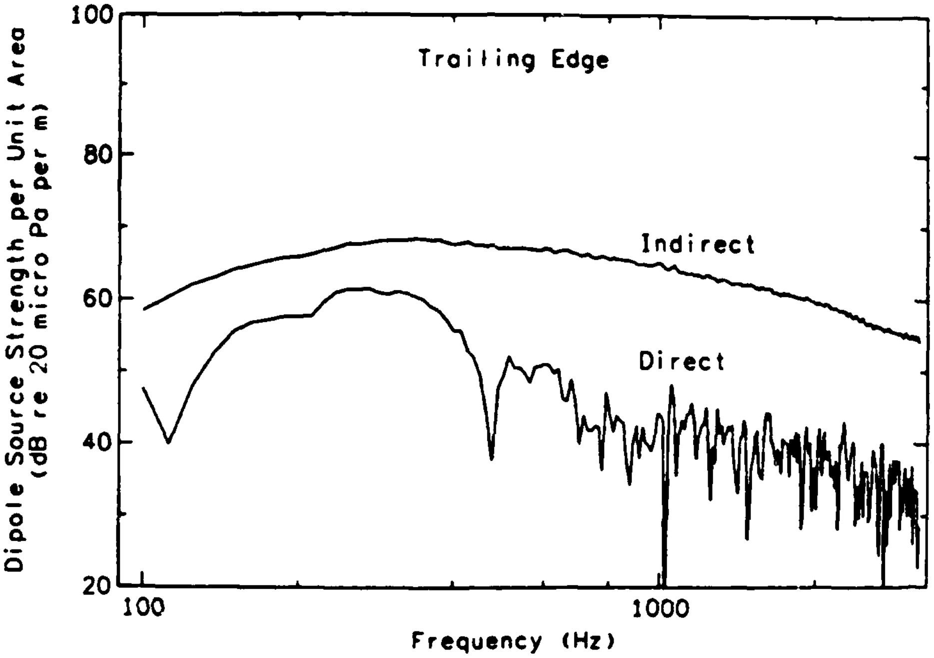

Figure 77. Comparison of Dipole Source Strength Estimators at Trailing Edge

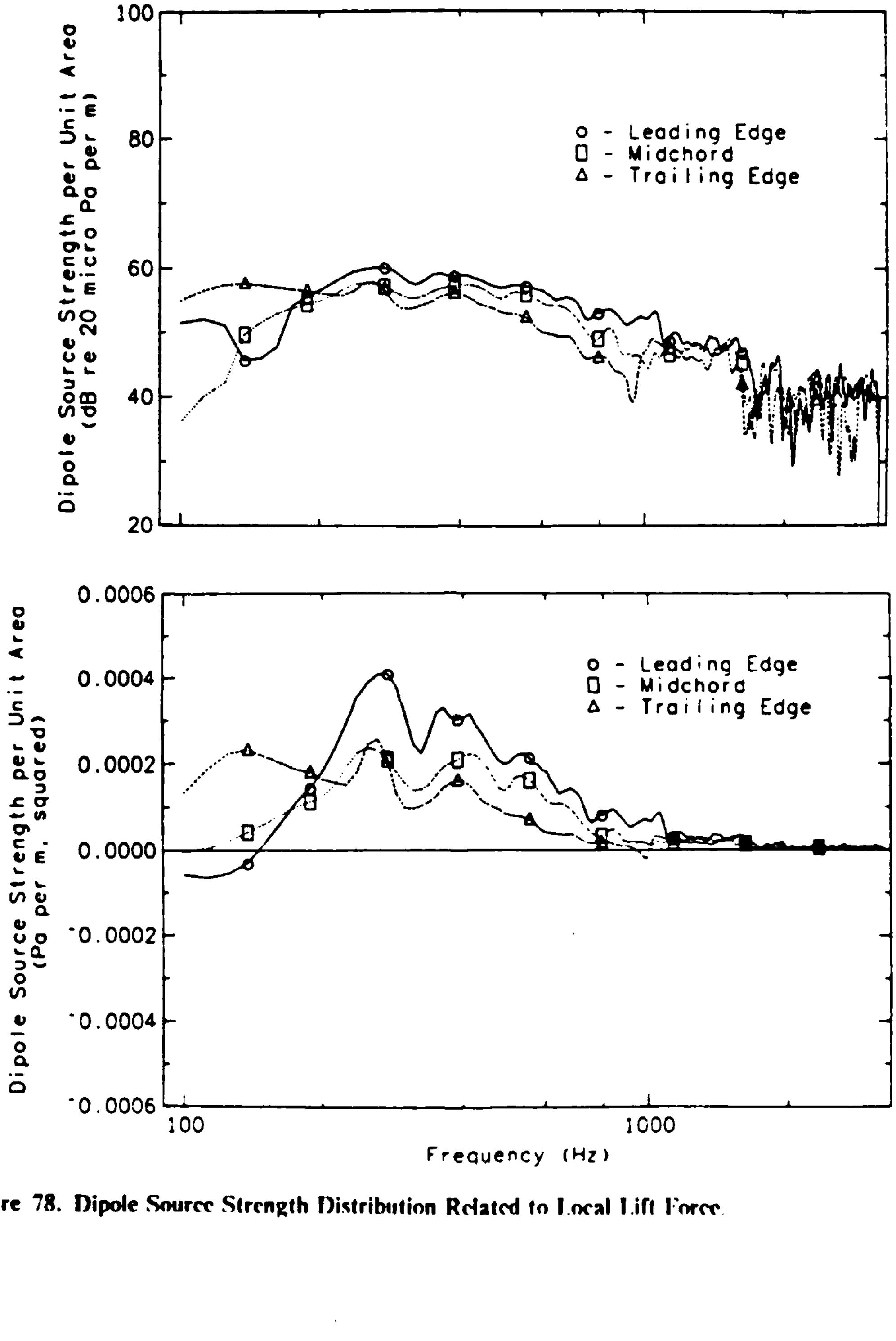

Figure 78. Dipole Source Strength Distribution Related to Local Lift Force

Chapter 7. Conclusions and Recommendations for Future Work

7.1 Conclusions and Discussions

The design goal of the model blower test vehicle was to produce a member of a homologous family of centrifugal blowers typically used for cooling electronics (especially in the computer industry). The design of the model should deviate from geometric similarity only to the extent necessary to minimize the generation of discrete-frequency noise associated with the rotor-stator interactions which occur at the cutoff of the scroll housing. This objective was met by designing a 2X scale model with increased cutoff angle to reduce the tonal noise. The resultant power spectrum was uniformly smooth over a wide range of operating points, with no evidence of narrow band noise.

Most of the experiments on the model blower were performed at the operating point of maximum static efficiency.[27] By definition, the BEP is the point of operation at which the impeller is most efficiently transferring mechanical rotational energy to the fluid. Examination of the power spectra taken over a range of operating points shows behavior typical of most air moving devices; that is, the radiated noise is a minimum at the BEP, and increases significantly at off-design operating points. The fact that noise increases for static pressures both greater than and less than the maximum-efficiency static pressure, indicates that the noise increase is due to a change in the local flow patterns in and around the impeller blade row, and not just the result of differences in the pressure rise across the blower.

---

[27] Also referred to as the best efficiency point (BEP) or design point.

The sound intensity distribution near the inlet to the model blower was measured using a custom-designed, automated scanning system built for this project. The results of the broad band intensity measurements were used to graphically construct energy flow maps of the active acoustic intensity field. In addition to the centrifugal blower, the intensity distribution near a small axial flow fan inlet was also determined and compared to the centrifugal blower data. The results were consistent with the notion that local source interactions (i.e., between different points on a distributed source) can occur if a causal relationship exists between the source regions. Local interactions between source regions can produce complicated energy flow patterns with areas of recirculation and cancellation indicated in the intensity field. For statistically independent source regions, the local interactions are negligible and the areas radiate independently producing an intensity field characteristic of outwardly propagating waves (point monopole radiation). Centrifugal and axial air moving devices are examples of independent and interacting distributed sources, respectively (provided the discrete frequency noise of the centrifugal device — rotor-stator interactions at the cutoff — is masked by the broad band components). Since a centrifugal blower can be thought of as a collection of random, independent source regions, noise cancellation methods have little chance of success for this class of air mover, since cancellation schemes rely on the causal relationships between source regions.

The aerodynamic field internal to the scroll housing was qualified through visualization techniques, and quantified using hot film anemometry. Measurement and visualization of the internal flow field near the impeller blade row lead to a good understanding of the essential qualities of the flow patterns, but detailed information was difficult to obtain. In general, the mean flow distribution through the blade channels was found to be similar to that measured by Raj [78].

Ideally, the mean flow through the impeller should be uniform in all three dimensions (circumferential, radial, and axial) to minimize the noise. For a given volumetric flow rate, and assuming that the noise generation is (indirectly) related to the mean flow velocity through the blade channels (possibly through a fifth or sixth power law), a uniform flow distribution represents the minimum noise condition, all other things being equal. The extent to which the mean flow deviates from the ideal represents some incremental increase in the overall noise generation. Additionally, the distribution of turbulence provides information on regions in flow which, when interacting with a solid boundary (blade surface), are directly responsible for noise generated by turbulence-boundary interactions. Consequently, the distribution of the mean and fluctuating flow field in the vicinity of the impeller blade row was determined and used to infer regions of high noise levels and indications of poor aerodynamic performance.

It was concluded that the mean flow through the impeller was not uniform. There was evidence of a flow deficit around the circumference of the impeller for the spanwise region covering the outer 20-40% of the blade span (i.e., nearest the inlet). Conversion from axial to radial momentum is a gradual process, with the resulting through flow deficit occurring near the inlet. In the circumferential direction the mean flow through the blades was reduced just downstream of the scroll cutoff.[28] The increased cutoff distance used for the model blower may be partially responsible for this effect, but it is more plausible to attribute this to a characteristic of the flow in the presence of the cutoff. Both the circumferential and spanwise nonuniformities were observed in the visualization studies. The possibility exists for improving the steady flow uniformity through scroll profile and/or impeller blade structure redesign.

The turbulence levels were generally low over most of the inlet to the blade channels, with the exception of the area opposite and downstream of the scroll cutoff,

---

[28] The term *downstream* is used here to denote the region on the side of the cutoff opposite from the blower discharge.

where they were significantly higher. The isolated region of increased turbulence on the inlet side near the cutoff suggests that the entire blade passage flow (as opposed to just the trailing edge region of the blade channel) is affected by the abrupt change in outlet flow impedance as the impeller passes the cutoff region. Since the turbulence is spatially periodic (once per revolution), the resultant noise generated by the periodic forces on the blades as they pass through the turbulence is narrow band. The turbulence itself being stochastic means that the phase of the sequential periodic pressures is also random. Also, since the turbulence is spatially distributed and the blades are of finite dimensions, the resulting noise is narrow band, and random. A barely detectable, relatively broad peak in the spectrum at the blade passage frequency is indicative of this phenomena.

Increased turbulence was also measured at the blade channel outlet. The velocity fluctuation intensity at the trailing edges of the blade row was uniformly high, showing almost no effect of the asymmetry of the scroll profile. The outlet turbulence, therefore, was due to local blade interactions caused by separated flow over the blade surface, turbulent boundary layer formation, and incidence and deflection fluid angle effects at the leading and trailing edges of the blades. The marked increase in turbulence from blade channel inlet to outlet is an important feature of the turbulent flow field and is an indicator of the noise generation process. It is impossible to determine from these measurements whether the turbulence is generated in the blade wake or whether it results from leading edge or midchord phenomena such as boundary layer separation. Efforts to reduce the turbulence levels from each of these regions would require different approaches. A natural extension of this analysis would be to examine the secondary flow effects in the blade channel. The intra-channel flow could be measured either in a stationary frame, using a laser doppler velocimeter and triggering system similar to the current setup, or, in a rotating frame, which has been done by several researchers [2, 27, 43, 61].

In summarizing the aerodynamic evaluation of the internal flow field, the mean flow patterns were determined and found to exhibit distinct regions of deficient flow, and other areas where the mean flow was quite high. Efforts to improve the mean flow distribution should produce a more efficient air mover with the added benefit of less noise. The relationship, however, between the mean flow velocity and the amount of noise generated is an indirect one. This is because turbulence is controlled not only by the flow speed, but by aerodynamic interactions which are dependent on the geometry of the airfoil and the fluid flow angles relative to the blade row. Therefore, the mean flow patterns are useful in understanding the basic flow phenomena and making some estimate of the effects on noise, but the real utility of these data is the role they play in estimating turbulence related effects from the steady flow field. A prime example of this point is the use of mean radial velocity measurements made at the blade inlet to compute the fluid incidence angle of the flow as it enters the blade channel. The incidence angle is a key parameter in cascade analysis because of the important stall conditions that may be predicted from knowledge of the angle of incidence. Note that stall refers to partial or complete separation over the blade suction surface, and is normally associated with a high angle of attack or incidence angle. A stalled impeller is both aerodynamically inefficient and excessively noisy.

The role of incidence angle on blower performance and acoustics was discussed briefly in the thesis. The incidence angle was estimated for the model blower, based on measurements of the mean radial velocity at the blade channel inlet, to be significantly different from ideal. The measured incidence angle was also used as input to the numerical model (developed using FLUENT) of two-dimensional flow over a single, isolated impeller blade immersed in a turbulent flow field. The flow simulations predicted suction side separation over most of the surface, even at 0° incidence, presumably due to blade curvature. The design benefits to forward blade curvature are best understood by considering exit velocity diagrams. The resultant increased rotational velocity is converted to static pressure at the exit, hence forward curved centrifugal blowers are considered high static pressure devices.

Results of experiments on a single isolated blade immersed in a controlled flow field comprise a significant portion of this thesis. A detailed discussion of the results was presented in Section Chapter 6, "Single Blade Investigations," and will be summarized here. The dipole source strength per unit area and correlation areas were estimated using frequency domain techniques developed in Chapter 2, "Theory of Aerodynamic Noise Generation." Since the blade was located in the turbulent mixing region of a free jet, high turbulence levels existed in the surrounding flow and were the primary cause for the radiated noise. There was however evidence of locally generated turbulence due to suction surface separation when the blade was oriented to produce a high angle of attack (30°). Estimates of the dipole source strength per unit area showed that more noise was radiated from the leading edge region than from the mid-chord or trailing edge, but the differences were small. The fact that no single region was dominant is consistent with the notion that the noise radiation in this particular experimental configuration was largely due to interactions of the free stream turbulence with the solid blade surface, and that noise generated as a result of local blade surface phenomena (separation or vortex shedding) was of secondary importance.

Estimates of the correlation area indicated that the correlated regions were largest at low frequencies. This is consistent with surface pressure coherence measurements which showed rapidly decreasing coherence between two fixed points on the surface with increasing frequency. The largest correlation areas peaked at about 25% of the total blade surface area (both sides combined) for frequencies around 250 Hz and decreased rapidly above that frequency. Correlation areas were very difficult to determine above 1 kHz due to the dominant effects of the correlation between the acoustic pressure and the *time derivative* of the surface pressure (i.e., $G_{rp} \propto \omega^2 \int_S G_{p_s p_s} S_c \, dS$).

Since the correlation area was determined to be a complex quantity which contains information on the extent of the local turbulence interactions and acoustic source interferences, negative values indicate destructive interference among local acoustic source regions. Some negative values of negative correlation areas were measured, however, a limited amount of destructive interference was indicated. Again, this is in general agreement with the premise of free stream turbulence being the primary noise source mechanism, since the ingested turbulence is a spatially distributed random process.

In conclusion, a wide range of experimental approaches have been utilized in an attempt to gain a better understanding of the noise generation mechanisms present in a low-speed centrifugal air moving device. The most significant results are those concerning the detailed flow investigations inside the blower housing, and the single blade experiments. While application of the experimental results of the single blade investigations to noise generation in a rotating impeller is not straightforward, the single blade experiments represent a significant initial effort at using modern signal analysis techniques for aerodynamic source identification in air moving devices.

Correlations were found to exist between the blade surface pressure and the radiated acoustic noise, and were strong enough to enable estimates of the local dipole source strength per unit area and correlation area. Significant advantages to using cross spectra over time domain functions typical of earlier work were discussed; the most obvious being the frequency-dependent information provided by the cross spectrum. In addition, comparisons were done of two methods for estimating the dipole source strength per unit area for the single blade radiation: the direct method which uses the cross spectrum, and the indirect method which is a *best guess* of the source strength based on surface pressure measurements only. It was shown that the the effects of local source interactions are significant and should not be ignored (the assumption of negligible aerodynamic source interactions is inherent in the use of the indirect method for estimating the dipole source strength per unit area).

7.2 Recommendations for Future Work

There are many areas of this research which could be extended. In a general sense, the theoretical development of Chapter 2, "Theory of Aerodynamic Noise Generation," has laid the foundation for frequency domain estimates of correlation area and the dipole source strength per unit area based on both the mean square acoustic pressure and the acoustic intensity. The latter has considerable potential in evaluating large scale structures as the directional characteristics of the intensity probe can be used to selectively examine certain regions of a radiating structure. In addition, the concept of a complex correlation area and the relationship to radiation efficiency should be explored, possibly using simplified acoustic sources, in an effort to better understand the meaning of negative and imaginary correlation areas. An error analysis should also be performed on the equations developed in Chapter 2, "Theory of Aerodynamic Noise Generation," in order to quantify the limitations of the measurement methodology. This is crucial to future applications of these expressions.

The experiments on a single blade should be extended, both in measurement technology (better sensors for improved signal-to-noise ratio) and in experimental complexity (multiple blades). By examining the radiation from two or more blades simultaneously immersed in a flow field (cascade analysis), blade-to-blade and blade-wake interactions could be evaluated.

Experimental work on an operational centrifugal blower should be continued by examining blade surface pressures (single- and two-point measurements) in a rotating reference frame. Since the correlation area can be estimated by a surface integral of the local two-point cross spectra as well as by a single cross spectrum between the radiated acoustic pressure and the local surface pressure, estimates of the correlation area could be made in a rotating frame without the noise problems associated with estimates of the acoustic field correlations using only blade surface pressure data. This work may require arrays of miniature sensors mounted in the blade surface. New pressure sensor technologies should be investigated for this purpose. Information on the correlation area in a rotating impeller would help considerably in establishing a better relationship between the isolated single blade experiments and radiation from an operational centrifugal blower. The correlation area is the link between the blade surface pressure and the conversion of the turbulent energy to acoustic noise.

Blade-to-blade surface pressure correlations (in a rotating frame) should also be quantified in order to assess the importance of blade-wake interactions. This could be done in conjunction with cascade analysis in a fixed frame for a more complete acoustical analysis than was possible with a single blade.

Regions of mean flow deficit and nonuniformity in the turbulent flow field were identified in the research. This information should be used as a basis for novel impeller and scroll configurations aimed at improving the flow uniformity and thereby reducing the noise levels. Impeller redesign should also emphasize the importance of proper selection of the mean flow incidence angle, which is a good indicator of excessive noise due to poor local blade airflow (stall). The relationship should be quantified between the incidence angle and noise. While computational fluid dynamics (CFD) computer programs are still rather limited, proper application of CFD to scroll and impeller redesign should be investigated as an effective design approach. Several of the key aerodynamic elements of a centrifugal blower could be simulated using rather simplified geometrical models.

Appendix. Principles of Centrifugal Blower Operation

In this chapter some basic terminology will be established which is used throughout the thesis. Topics covered include the velocity vectors at the inlet and outlet of the blade channels, Euler's pump equation, and the terminology associated with and important parameters involved in cascade analysis.

A.1 Velocity Diagrams

By convention, the absolute velocity vectors will be denoted by $\vec{V}$, and the velocity relative to the impeller by $\vec{W}$. Subscripts 1,2 are used to indicate inlet and outlet parameters, respectively. The velocity triangles at the leading and trailing edges of a mixed flow impeller are shown in Figure 79. The meridional velocity is the vector sum of the axial and radial components ($\vec{V}_m = \vec{V}_r + \vec{V}_x$). Since the blade has no meridional velocity (only tangential), then the total velocity component relative to the blade is given by the vector sum of the absolute meridional velocity and the relative tangential velocity:

$$\vec{W} = V_m \vec{i}_m + (V_\theta - \Omega r)\vec{i}_\theta \ . \tag{A.1}$$

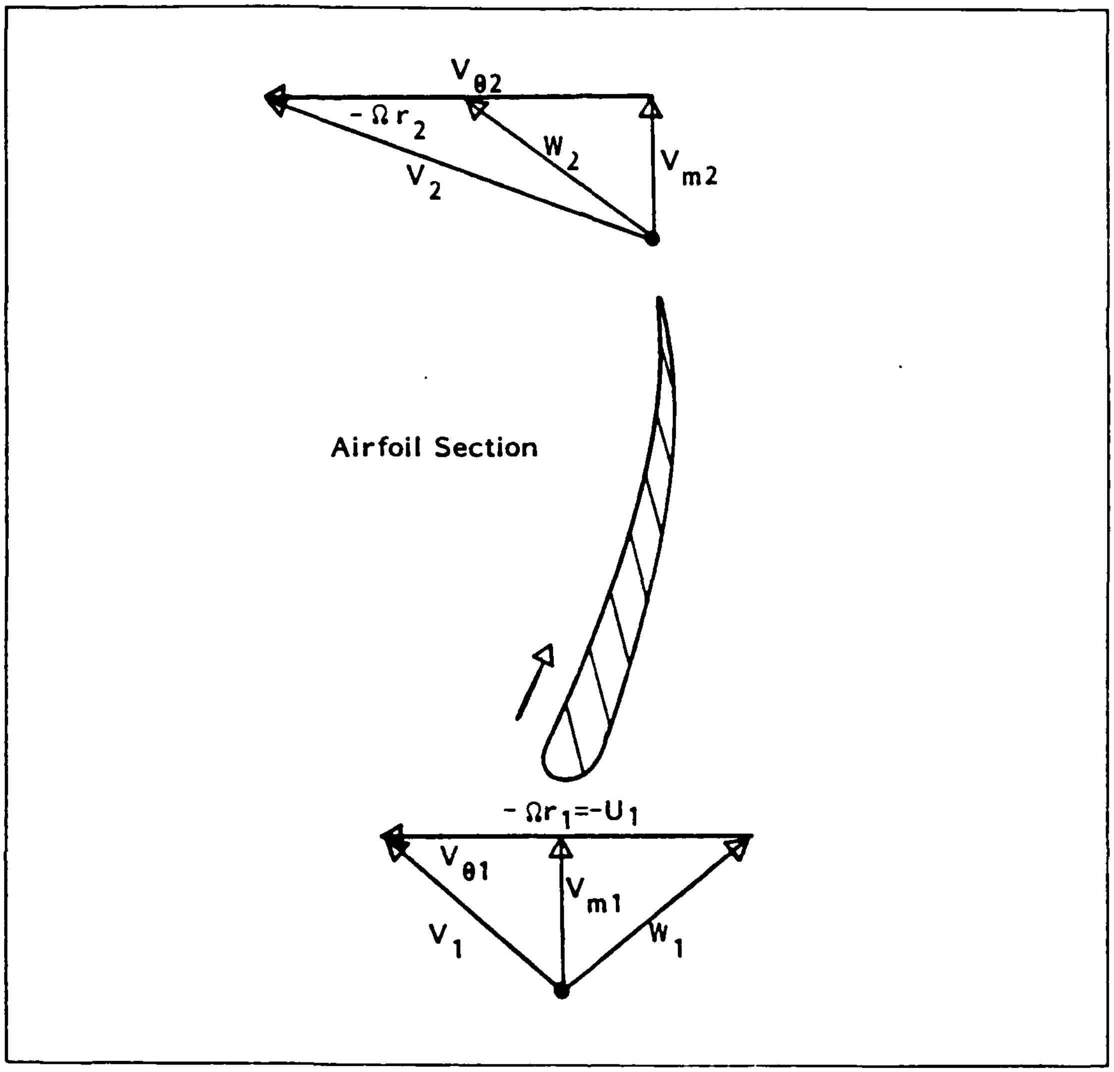

Figure 79. Two-Dimensional Velocity Diagrams for Mixed Flow Impeller. The plane of the figure is that of a stream surface intersected with an impeller blade.

A.2 Euler's Pump Equation

A fundamental relationship in turbomachinery is that between the rate at which energy is transferred to the fluid by the impeller, and the relative fluid velocity vector $\vec{c}$. The conservation of mean angular momentum may be applied to a control volume including the rotor to obtain this relationship, which is called *Euler's Pump Equation.*[29]

$$\frac{d\dot{W}}{d\dot{m}} = \frac{1}{2}\left[\left(V_2^2 - V_1^2\right) + \left(U_2^2 - U_1^2\right) - \left(W_2^2 - W_1^2\right)\right] \tag{A.2}$$

In these terms, Euler's pump equation is a decomposition of the energy transfer per unit mass into three terms which represent a change from inlet to exit of; 1) the kinetic energy relative to the casing (absolute), 2) the kinetic rotational energy (or radius, since $U = \Omega r$), and 3) the kinetic energy relative to the impeller. The following general statements made regarding the individual terms of Equation (A.2):

- For an axial device, the inlet and exit rotational velocity of the impeller is nearly constant (assuming negligible radial velocity through the blade row), hence the second term of Equation (A.2) is negligible. For a centrifugal device, however, the second term represents the transfer of rotational energy to the fluid and is a major contributor to the overall transfer of energy to the fluid. The first and last terms being equal, a centrifugal pump can produce greater energy transfer per unit mass flow than an axial device, simply due to the increase in rotational energy imparted to the fluid as it moves from the hub to

---

[29] The derivation appears in most basic fluid mechanics texts and will not be repeated here.

the tip of the impeller. This is why centrifugal devices are capable of producing greater static pressures than axial devices.

- In order to extract a contribution from the third term, $\vec{W}_2$ must be less than $\vec{W}_1$, thus the relative flow is decelerating and working against an adverse pressure gradient (i.e., $\partial p/\partial s > 0$). Flow is much more likely to separate from the impeller blade surface under these conditions. The corresponding term for a turbine is reversed, hence turbines are less susceptible to flow separation.

A.3 Cascade Analysis and Terminology

Cascade analysis is the two-dimensional representation of the intersection of a stream surface with the rotating impeller. If the stream surface is cylindrical, then the coordinate transformation $y = r\theta, \ \ x = x$ applies. This is an approximation that might be applied to an axial fan. For a centrifugal air moving device, especially where the blade chord is a small portion of the overall impeller diameter, the stream surface at the blade channel inlet can be considered to be a plane which is perpendicular to the axis of rotation This assumes a small axial velocity component at the leading edges of the blade row, which is shown in Chapter 5, "Aerodynamic Measurements in Model Blower," to be a realistic assumption for the blade span section near the hub of the impeller.

Using the simplification of negligible axial flow, a cascade model of the blade row may be obtained from the intersection between a plane perpendicular to the axis of rotation and the impeller blades, where the blade row is *unwrapped.* A schematic representation of the blade cascade for the model blower used in these experiments is shown in Figure 80.

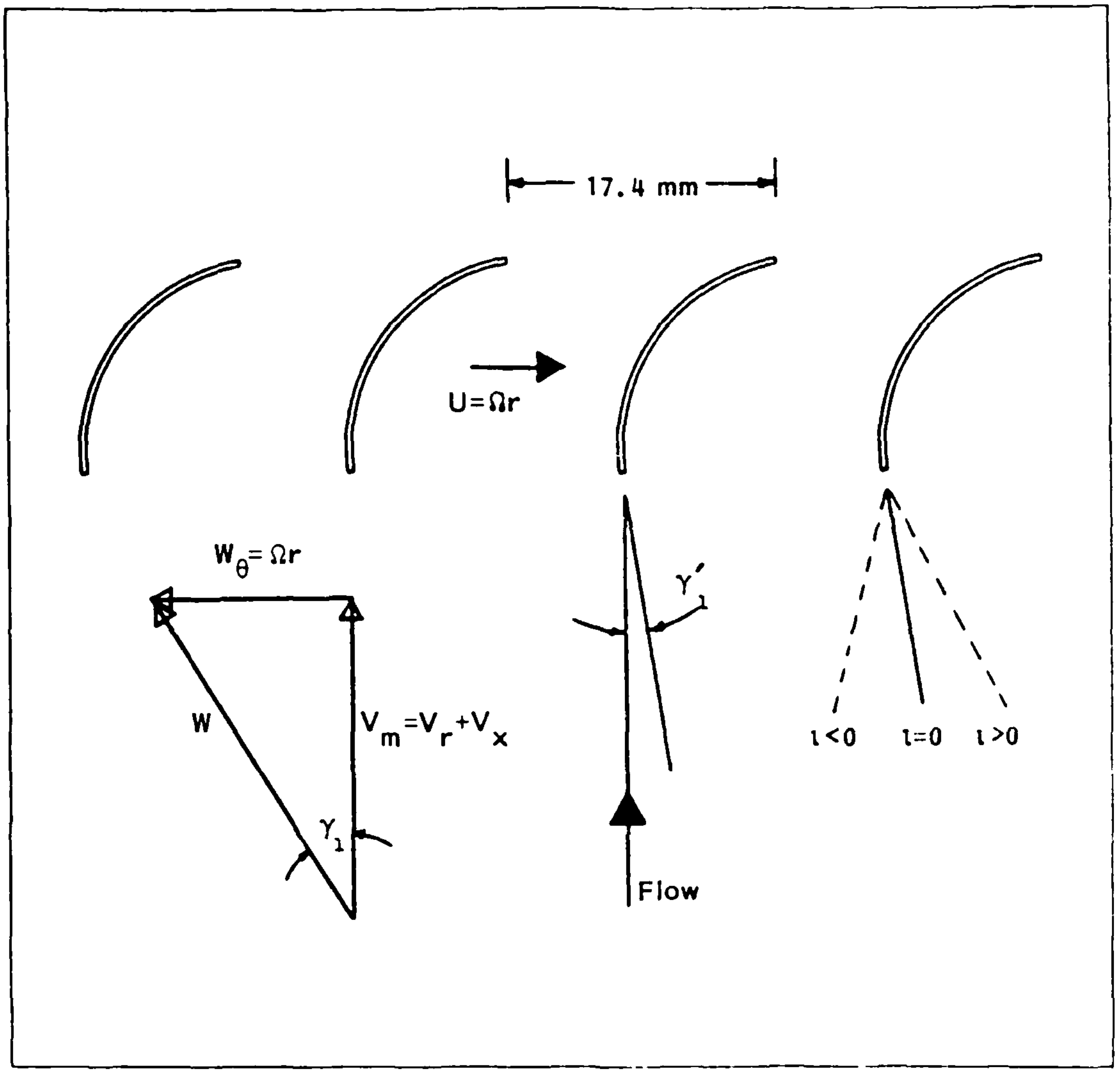

Figure 80. Cascade Schematic of Model Blower and Relevant Terminology. The axial velocity component is assumed to be negligible at the blade inlet, thus the stream surface lies in a plane perpendicular to the axis of rotation.

Terminology:

U = Blade Velocity ($U = \Omega r$)
Ω = Rotational Velocity of Blade (radians/second)
$\vec{V}_\theta$ = Tangential Fluid Velocity
$\vec{V}_m$ = Meridional Fluid Velocity ($\vec{V}_m = \vec{V}_x + \vec{V}_r$)
$\vec{V}_x$ = Axial Fluid Velocity
$\vec{V}_r$ = Radial Fluid Velocity
$\vec{V}$ = Total Fluid Velocity ($\vec{V} = \vec{V}_r + \vec{V}_x + \vec{V}_\theta$)
$\vec{W}$ = Total Fluid Velocity Relative to Impeller
γ_1 = Inlet Fluid Angle
γ'_1 = Inlet Blade Angle
ι = Incidence Angle ($\iota = \gamma_1 - \gamma'_1$)
γ_2 = Outlet Fluid Angle
γ'_2 = Outlet Blade Angle
δ = Deviation Angle ($\delta = \gamma_2 - \gamma'_2$)

The incidence angle is a critical parameter in cascade performance since there is a strong relationship between suction side separation (and consequent pressure loss) and increasingly negative values of incidence angle [24]. Beyond a certain value of negative incidence, the cascade is operating in a *stalled* region where there is a pronounced increase in total pressure loss across the blade cascade. Positive values of incidence can also lead to stalled performance. Several investigations have been performed in an effort to correlate cascade performance with fluid angles (incidence and deviation). Since the pressure losses are related to the growth and separation of the blade surface boundary layers, the incidence angle is taken as a measure of the overall cascade performance.

Bibliography

1. Abdelhamid, A.N. Acoustic response of a model ducted rotor to inflow fluctuations, AIAA paper, AIAA-74-89, January 1974.

2. Adler, D. and Levy, Y. A laser-doppler investigation of the flow inside a backswept, closed, centrifugal impeller. *J. Mechanical Engineering Science*, 21(1):1-6. 1979.

3. AMCA and ASHRAE. Laboratory methods of testing fans for rating, ASHRAE 51-75 / AMCA 210-74, 1975.

4. American National Standards Institute. Precision Methods for the Determination of Sound Power Levels of Broad-Band Noise Sources in Reverberation Rooms, ANSI S1.31, 1980.

5. American National Standards Institute. Precision Methods for the Determination of Sound Power Levels of Noise Sources in Anechoic and Hemi-Anechoic Rooms, ANSI S1.35, 1979.

6. Arndt, R.E. and Nagel, R.T. Effect of leading edge serrations on noise radiation from a model rotor, AIAA paper, AIAA-72-655, June 1972.

7. Baade, P.K. Effects of acoustic loading on axial flow fan noise generation. *Noise Control Engineering J.*, 8(1):5-15, January-February 1977.

8. Barsikow, B. and Neise, W. *The influence of non-uniform inflow conditions on centrifugal fan noise*, pages 89-93. Volume 1 in Czarnecki, S., *Inter-Noise 79*. Polish Academy of Sciences, Warszawa, Poland, 1979.

9. Bartenwerfer, M., Gikadi, T., Neise, W., and Agnon, R. Noise reduction in centrifugal fans by means of an acoustically lined casing. *Noise Control Engineering J.*, 8(3):100-107, May-June 1977.

10. Bendat, J.S. Solutions for the multiple input/output problem. *J. Sound Vib.*, 44(3):311-325, 1976.

11. Bendat, J.S. System identification from multiple input output data. *J. Sound Vib.*, 49(3):293-308, 1976.

12. Bendat, J.S. Statistical errors in measurement of coherence functions and input/output quantities. *J. Sound Vib.*, 59(3):405-421, 1978.

13. Bendat, J.S. Modern analysis procedures for multiple input output problems. *J. Acoust. Soc. Am.*, 68(2):498-503, August 1980.

14. Bendat, J.S. and Piersoll, A.G. *Random data: Analysis and measurement procedures*. Wiley-Interscience, New York, 1971.

15. Bendat, J.S. and Piersoll, A.G. *Engineering applications of correlation and spectral analysis*. Wiley-Interscience, New York, 1980.

16. Blake, W.K. A near-wake model for the aerodynamic pressures exerted on singing trailing edges. *J. Acoust. Soc. Am.*, 60(3):594-598, September 1976.

17. Brooks, T.F. and Hodgson, T.H. Trailing edge noise prediction from measured surface pressures. *J. Sound Vib.*, 78(1):69-117, 1981.

18. Buckingham, E. Model experiments and the form of empirical equations. *Trans. ASME*, 37:263-296, 1915.

19. Clark, L.T. The radiation of sound from an airfoil immersed in a laminar flow, ASME paper, 71-GT-4, March 1971.

20. Clark, P.J.F. and Ribner, H.S. Direct correlation of fluctuating lift with radiated sound for an airfoil in turbulent flow. *J. Acoust. Soc. Am.*, 46(3):802-805, 1969.

21. Corcos, G.M. The structure of the turbulent pressure field in boundary-layer flows. *J. Fluid Mech.*, 18:353-378, 1964.

22. Creare, Inc., FLUENT Manual, number TN-369, Hanover, NH, 1987.

23. Curle, N. The influence of solid boundaries upon aerodynamic sound. *Proc. R. Soc. London, Ser. A:*, 231A:505-514, 1955.

24. Dixon, S.L. *Fluid mechanics, thermodynamics of turbomachinery.* Pergamon Press, Elmsford, New York, 1978.

25. Dowling, A.P. and Ffowcs-Williams, J.E. *Sound and sources of sound.* Ellis Horwood Ltd., West Sussex, England, 1983.

26. Eck, B. *Fans: Design and operation of centrifugal, axial-flow and cross-flow fans.* Pergamon Press, New York, 1973.

27. Eckardt, D. Detailed flow investigations within a high-speed centrifugal compressor impeller. *J. Fluids Engineering (Trans. ASME)*, pages 390-402, September 1976.

28. Elko, G.W. *Frequency domain estimation of the complex acoustic intensity and acoustic energy density*, PhD thesis, Pennsylvania State University, 1984.

29. Embleton, T.F.W. Experimental study of noise reduction in centrifugal blowers. *J. Acoust. Soc. Am.*, 35(5):700-705, 1963.

30. Institute of Noise Control Engineering. Measurement of noise emitted by air-moving devices for cooling computer and business equipment, Recommended Practice 1-85, 1985.

31. Ffowcs Williams, J.E. and Hall, L.H. Aerodynamic sound generation by turbulent flow in the vicinity of a scattering half plane. *J. Fluid Mech.*, 40(4):657-670, 1970.

32. Franke, G.F. and Henderson, R.E. Unsteady stator response to upstream rotor wakes. *J. of Aircraft*, 17(7):500-507, July 1980.

33. Gearhart, W.S., Henderson, R.E., McMahon, J.F., and Horlock, J.H. The quasi-steady design of a compressor or pump stage for minimum fluctuating lift. *Trans. ASME, J. Eng. Power*, 68-WA/FE-12:1-6, 1968.

34. Goldstein, R.J. *Fluid Mechanics Measurements*. Hemisphere Publishing, New York, 1983.

35. Goulas, A. The production of vorticity and its effects on the flow in centrifugal compressor impellers, ASME paper, 79-GT-113, 1979.

36. Goulas, A. and Mealing, B. Flow at the tip of a forward curved centrifugal fan. ASME paper, 84-GT-222, 1984.

37. Henderson, R.E. and Horlock, J.H. An approximate analysis of the unsteady lift on airfoils in cascade. *J. of Engineering for Power (Trans. ASME)*, pages 233-240, October 1972.

38. Henderson, R.E. and Shen, I.C. The influence of unsteady rotor response on a distorted flow field. *J. of Engineering for Power (Trans. ASME)*, 104:683-691, July 1982.

39. Horlock, J.H., Greitzer, E.M., and Henderson, R.E. The response of turbomachine blades to low frequency inlet distortions. *J. of Engineering for Power (Trans. ASME)*, 99(2):195-203, April 1977.

40. Howe, M.S. A review of the theory of trailing edge noise. *J. Sound Vib.*, 61(3):437-465, 1978.

41. Huebner, G.H. Noise of centrifugal fans and rotating cylinders. *ASHRAE J.*, 5:87-94, November 1963.

42. Johnson, M.W. and Moore, J. The influence of flow rate on the wake in a centrifugal impeller. *J. of Engineering for Power (Trans. ASME)*, 105:33-39, January 1983.

43. Johnson, M.W. and Moore, J. Secondary flow mixing losses in a centrifugal impeller. *J. of Engineering for Power (Trans. ASME)*, 105:24-32, January 1983.

44. Jorgensen, R. *Fan engineering*. Buffalo Forge Company, Buffalo, New York, 1983.

45. Koopmann, G.H. and Neise, W. *An application of resonators in reducing centrifugal fan noise*, pages 219-222. Volume 1 in G.C. Maling, Jr., *Inter-Noise 80*. Noise Control Foundation, New York, USA, 1980.

46. Koopmann, G.H. and Neise,W. The use of resonators to silence centrifugal blowers. *J. Sound Vib.*, 82(1):17-27, 1982.

47. Krishnappa, G. Some experimental studies on centrifugal blower noise. *Noise Control Engineering J.*, 12(2):82-90, March-April 1979.

48. Krishnappa, G. *Effect of modulated blade spacing on centrifugal fan noise*, pages 215-218. Volume 1 in G.C. Maling, Jr., *Inter-Noise 80*. Noise Control Foundation New York, USA, 1980.

49. Launder, B.E. and Spaulding, D.B. *Mathematical models of turbulence.* Academic Press, New York, 1972.

50. Lee, H.K. Correlation of noise and flow of a jet, Univ. of Toronto Institute for Aerosp. Studies, UTIAS-168, Toronto, Canada. August 1971.

51. Lee, H.K. and Ribner, H.S. Direct correlation of noise and flow of a jet. *J. Acoust. Soc. Am.*, 52(5):1280-1290, 1972.

52. Leggat, L.J. and Siddon, T.E. Experimental study of the aeroacoustic mechanism of rotor-vortex interactions. *J. Acoust. Soc. Am.*, 64(4):1070-1077, October 1978.

53. Lighthill, M.J. On sound generated aerodynamically. I-General theory. *Proc. R. Soc. London, Ser. A:*, 211A:564-587, 1952.

54. Lighthill, M.J. On sound generated aerodynamically: II. Turbulence as a source of sound. *Proc. R. Soc. London, Ser. A:*, 222A:1-32, February 1954.

55. Lyons, L.A. and Platter, S. Effect of cutoff configuration on pure tones generated by small centrifugal blowers. *J. Acoust. Soc. Am.*, 35:1455-1456, 1963.

56. Madison, R.D. *Fan engineering.* Buffalo Forge Company, Buffalo, New York, 1949.

57. Maling, G.C., Jr. Dimensional analysis of blower noise. *J. Acoust. Soc. Am.*, 35(10):1556-1564, October 1963.

58. Maling, G.C., Jr. Measurements of noise generated by centrifugal blowers. *J. Acoust. Soc. Am.*, 35(11):1913, November 1963.

59. Maling, G.C., Jr. *Noise generated by small air moving devices*, pages 275-282. in Ken'iti Kido, *Inter-Noise 75.* Inter-Noise 75, Sendai, Japan, 1975.

60. Miller, W.R., Meecham, W.C., and Ahtye, W.F. Large scale model measurements of airframe noise using cross-correlation techniques. *J. Acoust. Soc. Am.*, 71(3):591-599, March 1982.

61. Mizuki, S., Ichiro, A., and Watanabe, I. A study on the flow mechanism within centrifugal impeller channels. ASME paper, 75-GT-14, 1975.

62. Moreland, J.B. Housing effects on centrifugal blower noise. *J. Sound Vib.*, 36(2):191-205, 1974.

63. Morfey, C.L. Rotating blades and aerodynamic sound. *J. Sound Vib.*, 28(3):587-617, 1973.

64. Mugridge, B.D. Turbulent boundary layers and surface pressure fluctuations on two-dimensional aerofoils. *J. Sound Vib.*, 18(4):475-486, 1971.

65. Mugridge, B.D. Noise characteristics of axial and centrifugal fans as used in industry. *Shock and Vibration Digest*, 7(9):93-107, 1975.

66. Naumann, H. and Yeh, H. Lift and pressure fluctuations of a cambered airfoil under periodic gusts and applications in turbomachinery. *J. of Engineering for Power (Trans. ASME)*, 95:1-10, 1973.

67. Neise, W. Application of similarity laws to the blade passage sound of centrifugal fans. *J. Sound Vib.*, 43(1):61-75, 1975.

68. Neise, W. Noise reduction in centrifugal fans: A literature survey. *J. Sound Vib.*, 45(3):375-403, 1976.

69. Neise, W. Review of noise reduction methods for centrifugal fans. *American Society of Mechanical Engineers*, 81-WA/NCA-2, 1981.

70. Neise, W. Noise and noise abatement in fans and blowers - a state of the art review, DFVLR, FB-80-16 (NTIS PB82-129784), Gottingen, Germany. 1981.

71. Neise, W. and Barsikow, B. Acoustic similarity laws for fans, ASME, 1981.

72. Neise, W. and Koopmann, G.H. Reduction of centrifugal fan noise by use of resonators. *J. Sound Vib.*, 73(2):297-308, 1980.

73. Patankar, S.V. *Numerical heat transfer and fluid flow.* Hemisphere Publishing, New York, 1980.

74. Patel, B.R., Dvinsky, A.S., and Hutchings, B.J. Application of computational fluid dynamics in engineering, Creare, Inc., TN-402, Hanover, NH. 1986.

75. Petrov, Y.I. and Khoroshev, G.A. Improving the noise-level of centrifugal fans. *Russian Engineering J.*, 51(11):42-44, 1971.

76. Ploner, B. and Herz, F. New design measures to reduce siren tones caused by centrifugal fans in rotating machines. *Brown Boveri Revu*, 56:280-287, 1969.

77. Raffy, P., Lewy, S., Lambourion, J., and Chatanier, M. Investigation of fan noise sources by blade pressure measurements. *AIAA J.*, 16(8):777-778, 1978.

78. Raj, D. *Identification of noise sources in FC centrifugal fan rotors*, PhD thesis, Tennessee Technological University, August 1978.

79. Raj, D. and Swim, W.B. *Measurements of the mean flow velocity fluctuations at the exit of an FC centrifugal fan rotor*, pages 43-49. in *Symposium on Measurement Methods in Rotating Components of Turbomachinery.* ASME, New York, 1980.

80. Richarz, W.G. Direct correlation of noise and flow of a jet using laser doppler, Univ. of Toronto Institute for Aerosp. Studies, UTIAS-230, Toronto, Canada. June 1978.

81. Robbins, B. and Lakshminarayana, B. Effect of inlet turbulence on compressor noise. *J. of Aircraft*, 11(5):273-281, May 1974.

82. Schlichting, H. *Boundary-layer theory.* McGraw-Hill, New York, 1979.

83. Schmidt, D.P. and Okiishi, T.H. Multistage axial-flow turbomachine wake production, transport, and interaction. *AIAA J.*, 15, 1977.

84. Sentek, J. Influence of geometrical parameters upon the sound power level of centrifugal fans. *J. Sound Vib.*, 61(3):383-389, 1978.

85. Seybert, A.F. and Hamilton, J.F. Time delay bias errors in estimating frequency response and coherence functions. *J. Sound Vib.*, 60(1):1-9, 1978.

86. Sharland, I.J. Sources of noise in axial flow fans. *J. Sound Vib.*, 1(3):302-322, 1964.

87. Siddon, T.E. *New correlation method for study of flow noise*, pages 533-536. Volume 2 in *7th ICA*. Akademiai Kiado, Budapest, 1971.

88. Siddon, T.E. Surface dipole strength by cross-correlation method. *J. Acoust. Soc. Am.*, 53(2):619-633, 1973.

89. Smith, W.A., O'Malley, J.K., and Phelps, A.H. *Reducing blade passage noise in centrifugal fans*, pages 45-52. Volume 80 in *ASHRAE Transactions, Part II*. ASHRAE, 1959.

90. Tam, C.K.W. Intensity, spectrum, and directivity of turbulent boundary layer noise. *J. Acoust. Soc. Am.*, 57(1):25-34, January 1975.

91. Tennekes, H. and Lumley, J.L. *A first course in turbulence*. MIT Press, Cambridge, Mass., 1972.

92. Wang, M.E. and Crocker, M.J. On the application of coherence techniques for source identification in a multiple noise source environment. *J. Acoust. Soc. Am.*, 74(3):861-872, September 1983.

93. Wieland, H. Edge serrations for low noise centrifugal blower, U.K. Patent GB 2-105-791A, September 1982.

94. Wise, R.E., Maling, G.C., Jr., and Masuda, K. Qualification of a 230 cubic metre reverberation room. *Noise Control Engineering J.*, 7(2):98-104, September-October 1976.

95. Wright, T. Centrifugal fan performance with inlet clearance. *American Society of Mechanical Engineers*, (84-GT-186), 1984.

96. Yeager, D.M. *Centrifugal blower noise reduction using a flow resistive scroll*, pages 231-238. in R. Lotz, *Noise-Con 83*. Noise Control Foundation, NewYork, USA, 1983.

97. Yeager, D.M. *Measurement of air moving device sound intensity distribution*, pages 133-138. in Singh, R., *Noise-Con 85*. Noise Control Foundation, Poughkeepsie, NY, 1985.

98. Yocum, A.M. and Henderson, R.E. The effects of some design parameters of an isolated rotor on inlet flow distortions. *J. of Engineering for Power (Trans. ASME)*, 102(1):178-186, January 1980.

99. Zhichi, Z., Yongxi, L., and Shouxue, F. *Experimental investigation in reduction of centrifugal fan noise by use of resonator and theoretic analysis of resonance frequency*, pages 199-204. Volume 1 in R. Lotz, *Inter-Noise 86*. Noise Control Foundation, New York, USA, 1986.